

**JULIANA MARINI MARSON**

**Meltwater impacts on the ocean  
circulation since the Last Glacial  
Maximum**

Thesis submitted to the Instituto Oceanográfico  
- Universidade de São Paulo in partial fulfillment  
of the requirements for the degree of  
Doctor of Philosophy in Sciences, Oceanography  
Program, Physical Oceanography area.

Advisor: Dr. Ilana E. K. C. Wainer  
Co-Advisor: Dr. Mauricio M. Mata  
Supervisor at McGill University: Dr. Lawrence A. Mysak

**São Paulo  
2015**

Universidade de São Paulo  
Instituto Oceanográfico

# Meltwater impacts on the ocean circulation since the Last Glacial Maximum

JULIANA MARINI MARSON

Thesis submitted to the Instituto Oceanográfico  
- Universidade de São Paulo in partial fulfill-  
ment of the requirements for the degree of  
Doctor of Philosophy in Sciences, Oceanogra-  
phy Program, Physical Oceanography area.

Judged in       /       /       by

---

Prof. Dr.

---

Grade

---

# Contents

---

<b>List of Figures</b>	<b>iv</b>
<b>List of Tables</b>	<b>v</b>
<b>List of Acronyms</b>	<b>vi</b>
<b>Acknowledgments</b>	<b>viii</b>
<b>Resumo</b>	<b>xi</b>
<b>Abstract</b>	<b>xiii</b>
<b>1 Introduction</b>	<b>1</b>
<b>2 Climate evolution since the Last Glacial Maximum</b>	<b>4</b>
2.1 Climate state at 21,000 years ago . . . . .	5
2.2 The last deglaciation . . . . .	6
2.3 The Holocene . . . . .	10
<b>3 The transient simulation TraCE-21K</b>	<b>12</b>
3.1 NCAR-CCSM3 numeric model . . . . .	12
3.2 TraCE-21K settings . . . . .	13
3.3 Simulation performance . . . . .	19
<b>4 The Atlantic Ocean's deglacial evolution: Introduction</b>	<b>21</b>
4.1 Present-day structure of the deep ocean circulation . . . . .	21
4.2 Deep ocean circulation changes in the last 21,000 years . . . . .	25
<b>5 The Atlantic Ocean's deglacial evolution: Meridional transports</b>	<b>28</b>
5.1 The AMOC . . . . .	28
5.2 Meridional heat and salt transport . . . . .	31

---

<b>6</b>	<b>The Atlantic Ocean's deglacial evolution: Thermohaline characteristics</b>	<b>35</b>
<b>7</b>	<b>The Atlantic Ocean's deglacial evolution: Water masses distribution</b>	<b>42</b>
7.1	The mixing triangle technique . . . . .	42
7.2	Issues and their solutions within the mixing triangle technique . . . . .	45
7.3	Results . . . . .	49
7.3.1	Evolution of the water types' properties . . . . .	49
7.3.2	Spatial contribution of analyzed water masses in the Atlantic Ocean . . . . .	53
7.4	Discussion . . . . .	57
<b>8</b>	<b>The Southern Ocean and the Meltwater Pulse 1A</b>	<b>64</b>
8.1	Regional evolution of thermohaline properties: Weddell and Ross Seas	65
8.2	The impact of the MWP-1A on the Southern Ocean dynamics . . . . .	70
<b>9</b>	<b>The Indian Ocean's response to meltwater fluxes</b>	<b>73</b>
9.1	The Indian Ocean's characteristics . . . . .	74
9.2	Impacts of meltwater pulses on the Indian Ocean . . . . .	76
<b>10</b>	<b>General Conclusions and Final Considerations</b>	<b>82</b>
	<b>Academic production</b>	<b>86</b>
	<b>Bibliography</b>	<b>87</b>

---

## List of Figures

---

2.1	Ice sheet reconstruction at 21 ka . . . . .	5
2.2	Insolation, temperature and GHG since 21 ka . . . . .	7
3.1	TraCE-21K construction . . . . .	14
3.2	Meltwater flux rates and locations . . . . .	16
4.1	Atlantic's wind driven circulation . . . . .	22
4.2	Modern AMOC scheme . . . . .	23
4.3	Salinity at 25°W from WOCE . . . . .	24
4.4	Glacial AMOC scheme . . . . .	26
5.1	AMOC from TraCE-21K . . . . .	30
5.2	Heat and salt transports . . . . .	32
5.3	Scatter diagram of heat and salt transports . . . . .	34
6.1	Atlantic's salinity across 25°W . . . . .	37
6.2	Atlantic's salinity differences between climatic periods across 25°W . . . . .	37
6.3	Atlantic's temperature across 25°W . . . . .	38
6.4	Atlantic's temperature differences between climatic periods across 25°W . . . . .	39
6.5	$\theta - S$ for the South Atlantic . . . . .	41
7.1	Mixing between two hypothetical water masses A and B. . . . .	43
7.2	Mixing between three hypothetical water masses A, B, and C. . . . .	44
7.3	Atlantic's $\theta - S$ diagram at different periods and its water types . . . . .	47
7.4	Temperature and salinity evolution of CW . . . . .	50
7.5	Temperature and salinity evolution of AAIW . . . . .	50
7.6	Temperature and salinity evolution of AABW . . . . .	52
7.7	Temperature, salinity, and core depth evolution of GNAIW and NADW . . . . .	52
7.8	Vertical distribution of CW . . . . .	54
7.9	Horizontal distribution of CW . . . . .	54
7.10	Vertical distribution of AAIW . . . . .	55
7.11	Horizontal distribution of AAIW . . . . .	55

---

7.12	Horizontal distribution of AAIW during H1 . . . . .	55
7.13	Vertical distribution of AABW . . . . .	56
7.14	Horizontal distribution of AABW . . . . .	56
7.15	Vertical distribution of GNAIW and NADW . . . . .	58
7.16	Horizontal distribution of GNAIW and NADW . . . . .	58
7.17	Alternative distribution of GNAIW . . . . .	59
7.18	SST, precipitation-evaporation, and meltwater fluxes . . . . .	60
8.1	Transects in the Southern Ocean . . . . .	65
8.2	Temperature in the Weddell Sea . . . . .	66
8.3	Temperature in the Ross Sea . . . . .	67
8.4	Salinity in the Weddell Sea . . . . .	68
8.5	Salinity in the Ross Sea . . . . .	69
8.6	Current speed, salinity, and wind stress at 55 and 65°S . . . . .	71
8.7	Flow generated by the salinity gradient between the Antarctic coast and 50°S . . . . .	72
9.1	Climatological winds over the Indian Ocean . . . . .	74
9.2	Indian Ocean surface circulation . . . . .	75
9.3	Western Indian Ocean vertical salinity from WOCE . . . . .	75
9.4	Western Indian Ocean vertical salinity from TraCE-21K . . . . .	77
9.5	Southwest Indian Ocean mean salinity and temperature at different layers . . . . .	78
9.6	$\theta - S$ diagram for the southwestern Indian Ocean . . . . .	80
9.7	Wind stress time series at the equator, 53°E. . . . .	80
9.8	EUC core speed and depth at 53°E. . . . .	81

---

## List of Tables

---

3.1 Detailed meltwater flux rates and locations prescribed on TraCE-21K . . .	18
---	----

---

## List of Acronyms

---

<b>AABW</b>	Antarctic Bottom Water
<b>AAIW</b>	Antarctic Intermediate Water
<b>ACC</b>	Antarctic Circumpolar Current
<b>ACoC</b>	Antarctic Coastal Current
<b>AMOC</b>	Atlantic Meridional Overturning Circulation
<b>BA</b>	Bølling-Allerød
<b>CDW</b>	Circumpolar Deep Water
<b>CW</b>	Central Waters
<b>D-O</b>	Dansgaard-Oeschger
<b>EICC</b>	East Indian Coastal Current
<b>EUC</b>	Equatorial Undercurrent
<b>GHG</b>	Greenhouse gas
<b>GNAIW</b>	Glacial North Atlantic Intermediate Water
<b>H1</b>	Heinrich Stadial 1
<b>ka</b>	Thousands of years ago
<b>LGM</b>	Last Glacial Maximum
<b>MWP-1A</b>	Meltwater pulse 1A
<b>NACW</b>	North Atlantic Central Water
<b>NADW</b>	North Atlantic Deep Water
<b>NH</b>	Northern Hemisphere
<b>NOHT</b>	Northward ocean heat transport
<b>NOST</b>	Northward ocean salt transport
<b>RSW</b>	Red Sea Water
<b>SAMW</b>	Subantarctic Mode Water
<b>SH</b>	Southern Hemisphere
<b>SACW</b>	South Atlantic Central Water
<b>SAT</b>	Surface air temperature
<b>WDW</b>	Warm Deep Water
<b>WICC</b>	West Indian Coastal Current
<b>YD</b>	Younger Dryas

To Prof. João Marson, my father, who taught me the physics, the values and the everlasting wish to learn.

Ao Prof. João Marson, meu pai, quem me ensinou a física, os valores e o eterno desejo de aprender.

---

## Acknowledgments

---

I have always looked up to teachers. They turn empty heads into a paradise of ideas, knowledge and conscious opinions. They transform human beings into citizens. And, yet, they get almost nothing back (especially nowadays, especially in Brazil). They are not even respected by most of the students — or their parents, as a matter of fact. Teachers have nothing but this unmeasurable passion for giving all they have in their minds in the hope that a few of the listeners is going to grow to be a good person. Today, I hope I am one of them. That is why I begin here by thanking all my teachers, from my childhood to my adolescence. They made me understand that, in my own words at that time, I wanted nothing but to be an eternal student.

My special thanks go to two teachers that made me want to be a scientist. First, my father João, my Physics teacher, in whom I mirror myself to be as much organized, determined and passionate about something as he is. I am very proud to be a lot like him in this sense. Dad, I want you to know that everything your dad expected you to be, you became: a scientist, a master, a bright mind, and on the top of all that, an amazing parent. Second, my first Science teacher, Lucilia, who presented me to this amazing world and always encouraged me to pursue Ocean Sciences.

I also thank all my professors at the University, especially the ones who showed me what kind of professor I want to be some years ahead from now. To my advisors — Rodrigo, Mauricio, and Ilana —, I give my sincere acknowledgements for giving me the opportunity to learn from them in all kinds of situation. To McGill University and my supervisor, Dr. Lawrence Mysak, my eternal appreciation for welcoming me at his research group for one year. Prof. Mysak showed me what is to be an honest and respected scientist, an exceptional professor and advisor, and a remarkable human being.

I am extremely grateful to my mother. Even with a broken heart from seeing a child leave for so long and so far, she always supported me in my decisions and comforted me when those were the wrong ones. My mom is always there, no matter what. She is brave and loving, as every mother in the world should be. I thank my sister for her love and her husband for our nerd talks. To my aunts, uncles, cousins, and grandparents (the four of them), I thank to be part of this family. I still believe, as a kid does, that our family is perfect.

To my husband-to-be, I thank for his endless love, patience, support, and encouragement. I could not have done it without him. He never let me give up or desperate when things got ugly. He is not only my sweetheart. He is my partner, he is my team, he is my best friend. That is how I know we will be always together. To my parents-in-law, I also thank for their love and support at every single moment of the last three years.

I thank my friends, the scientist ones and the mentally-healthy ones too. Marc and Ana Paula, in particular, thank you for sharing academic crises, deep conversations about life and science, and, of course, hilarious comics and cat videos.

Finally, I thank the FAPESP agency for allowing me to continue my academic formation through the grants 2011/02047-9 and 2013/20977-9.

Each piece of this work exists because of you all.

"My goal is simple. It is a complete understanding of the universe, why it is as it is and why it exists at all."

—*Stephen Hawking*

---

## Resumo

---

**D**URANTE os últimos 21.000 anos, o planeta sofreu grandes mudanças. A concentração de CO<sub>2</sub> atmosférico aumentou cerca de 50% (Monnin et al., 2001) e a temperatura média global aumentou  $4,0 \pm 0,8^{\circ}\text{C}$  até a época pré-industrial (Annan and Hargreaves, 2013). Como consequência deste aquecimento, os grandes mantos de gelo que cobriam a América do Norte, o norte da Europa e parte da Eurásia derreteram e os oceanos polar e subpolar receberam grandes quantidades de água doce destes mantos em retração. A entrada de água doce altera gradientes de pressão na superfície do mar e também a densidade de massas de água. Como a circulação oceânica é parcialmente forçada por diferenças de densidade, a água de degelo tem o potencial de afetar esta circulação. Nesta tese de Doutorado, os impactos da entrada de água de degelo no oceano desde o Último Máximo Glacial em altas latitudes, especialmente do Oceano Atlântico, são estudados usando os resultados de uma simulação transiente dos últimos 22 mil anos com o modelo NCAR-CCSM3. Os principais resultados mostram que: (1) a circulação de revolvimento meridional do Atlântico enfraqueceu durante eventos de descarga de água doce próxima a regiões de formação de água densa; (2) a Água Profunda do Atlântico

Norte (APAN) estava ausente no começo da deglaciação, enquanto sua versão intermediária — Água Glacial Intermediária do Atlântico Norte (AGIAN) — era formada; (3) AGIAN era uma massa d'água doce e fria, semelhante à Água Intermediária Antártica (AIA) no domínio termohalino atual; (4) as camadas profundas e de fundo da bacia do Atlântico eram dominadas pela Água de Fundo Antártica (AFA) na primeira metade da simulação; (5) a transição de AGIAN para APAN ocorreu após o Heinrich Stadial 1; (6) quando a APAN apareceu, cerca de 12 mil anos atrás (ka), a AFA retraiu e ficou limitada às camadas de fundo; (7) a presença de uma camada de baixa salinidade na superfície do Oceano Austral há ~14 mil anos impedia a liberação de calor das águas profundas para a atmosfera, aquecendo a AFA; (8) a Corrente Costeira Antártica foi intensificada pela descarga de água de degelo proveniente do manto de gelo Antártico. Usando o Oceano Índico como comparação, foi observado que o Atlântico Norte afetou o Índico oeste tropical através de processos atmosféricos, enquanto variações climáticas associadas ao Hemisfério Sul foram transmitidas via oceano — especialmente através das camadas intermediárias. Embora as condições iniciais dos oceanos glacial e moderno sejam diferentes, este estudo pode ser usado para prever as possíveis respostas do oceano ao presente derretimento acelerado de geleiras e mantos de gelo associado a mudanças climáticas abruptas.

---

## Abstract

---

**D**URING the last 21,000 years, the planet underwent major changes. The atmospheric CO<sub>2</sub> concentration increased ~50% (Monnin et al., 2001) and the mean global temperature increased  $4.0 \pm 0.8^\circ\text{C}$  until pre-industrial times (Annan and Hargreaves, 2013). As a consequence of this warming, the huge ice sheets that covered North America, Northern Europe and part of Eurasia melted and the polar and subpolar ocean surface received a large amount of freshwater from these retracting ice sheets. The input of freshwater alters pressure gradients on the sea surface and also the density of water masses. Since the ocean circulation is partially driven by density differences, the deglacial meltwater has the potential to affect the ocean circulation. In this PhD thesis, the impacts of meltwater input since the Last Glacial Maximum into the high latitudes, especially of the Atlantic Ocean, are studied using the results of a transient simulation of the last 22 thousand years with NCAR-CCSM3. The main results show that: (1) the Atlantic Meridional Overturning Circulation (AMOC) slowed down during freshwater discharge events near dense water formation regions; (2) North Atlantic Deep Water (NADW) was absent in the beginning of the deglaciation, while its intermediate version — Glacial North Atlantic

Intermediate Water (GNAIW) — was being formed; (3) GNAIW was a fresh and cold water mass, very similar to the Antarctic Intermediate Water (AAIW) in the thermohaline domain; (4) the deep and abyssal Atlantic basin was dominated by AABW in the first half of the simulation; (5) the transition from GNAIW to NADW occurred after the Heinrich Stadial 1; (6) when the NADW appeared, around 12 thousand years ago (ka), AABW retracted and was constrained to lie near the bottom; (7) the presence of a low-salinity layer in the Southern Ocean surface around 14,000 years ago prevented the release of heat from deep waters to the atmosphere, warming the AABW; (8) the Antarctic Coastal Current (ACoC) was reinforced by the meltwater discharge from the Antarctic ice sheet. Using the Indian Ocean as a comparison, it was observed that the North Atlantic affected the western tropical Indian through atmosphere, while climatic variations associated with the Southern Hemisphere were transmitted via ocean — especially through intermediate waters. Although the initial conditions in the glacial and modern ocean are different, this study may be used to foresee the possible responses of the ocean to the accelerated melting of glaciers and ice sheets, which are associated with dramatic climate changes.

# CHAPTER 1

---

## Introduction

---

**T**HE impact of human activities on the climate has never been so evident. According to IPCC 5<sup>th</sup> Assessment Report (2013), more than a half of the observed increase in the global mean surface temperature from 1951 to 2010 was caused by anthropogenic increase in greenhouse gas (GHG) concentrations and other anthropogenic forcings together. The climate system is responding to this warming: over the last twenty years, the Greenland and Antarctic ice sheets have been losing mass and glaciers have continued to shrink almost worldwide. Between 1992 and 2011, the melting of ice sheets has contributed to a sea level rise rate of  $0.59 \pm 0.20$  mm/yr (Shepherd et al., 2012). Moreover, the projections for future climate point out that current glacier extents are out of balance with the present climatic conditions, indicating that glaciers will continue to shrink even without further temperature increase. Meanwhile, the oceans are receiving all this melted ice and the scientific community is concerned about the changes in ocean circulation that this meltwater input may trigger (e.g., Swingedouw et al., 2006; Driesschaert et al., 2007;

Hu et al., 2011; Blaschek et al., 2014).

The oceans are fundamental to the climate system as they are the major sink of atmospheric energy and carbon (e.g., Ellis et al., 1978; Hall and Bryden, 1982; Gruber et al., 2002; Sabine et al., 2004). The large-scale ocean circulation distributes heat from the tropical regions to higher latitudes. As an example of the ocean role in the heat distribution, consider the warm equatorial waters that are carried by the Gulf Stream. They travel northward along the USA coast and turn toward Europe as the North Atlantic Current. From there, the warm waters are picked up by the Norwegian Current, which bathes the Norway coast. This is why the northwestern Europe enjoys a milder climate than Canada at the same latitude (e.g., Hartmann, 1994). The deep ocean circulation is, on average, meridional, and it is mainly driven by density differences among water masses formed in the North Atlantic and Southern Ocean. Since the density of sea water is mainly controlled by temperature and salinity, changes in those fields lead to changes in circulation. For example, when warm tropical waters are transported to the northern North Atlantic they release heat to the atmosphere and become cold — therefore, denser than their surroundings — which leads these waters to sink to the deep ocean. Although the temperature is usually more important in determining density, changes in salinity also affect the vertical position of a water parcel in the water column, especially near the poles, where temperatures do not change much. Thus, the input of freshwater coming from the melting of ice sheets and glaciers at high latitudes can affect ocean circulation (e.g., Blaschek et al., 2014).

The introduction of large amounts of meltwater has happened before in Earth's history. Around 20,000 years ago, continental ice sheets covered North America, the northern portion of Europe and part of Eurasia (Peltier, 1994). From that time until the middle Holocene (around 6,000 years ago), these ice sheets melted, contributing to a sea level rise of  $\sim 120$  m during the last 21 thousand years (Fairbanks, 1989). Studying the climate of the past, therefore, can help us understand what responses should be expect under extreme climate changes. In order to do that, scientists use numerical models that might explain how the observed variations in the several cli-

mate system components happened and interacted to each other. One of the many interesting aspects of studying the Earth's past climate through numerical models is that they give us a better understanding of the mechanisms and ranges of the climate system's natural variability. This comprehension allows us to improve models and access their sensibility before trying to simulate future climate changes.

The present thesis has the main objective of evaluating the ocean responses to meltwater influxes. The specific objectives are:

1. To analyze changes in the Meridional Overturning Circulation and its associated transports of heat and salt under the influence of meltwater discharges;
2. To diagnose variations in the temperature and salinity fields of the Atlantic Ocean, where most of the meltwater is introduced;
3. To determine the distribution of the main Atlantic water masses before, during, and after meltwater discharge episodes;
4. To evaluate the local impacts of a meltwater discharge in a key region to water mass formation;
5. To verify the potential teleconnections of Atlantic meltwater fluxes to other oceans.

It is hypothesized that the accelerated melting of glaciers and ice sheets affects the ocean circulation and, consequently, the climate equilibrium. In order to reach the presented goals, the results of a transient simulation of the past 22,000 years are analyzed. Each chapter of this thesis addresses one of the specific objectives. In Chapter 2, the evolution of climate for the last 21,000 years is presented. Chapter 3 describes the model and simulation which generated the data analyzed. Chapters 4 to 7 assess the changes in the Atlantic Ocean's circulation, thermohaline characteristics, and water masses distribution. Chapter 8 presents some local impacts of the meltwater presence in the Southern Ocean. Chapter 9 investigates how an ocean that is isolated from the North Atlantic — the Indian Ocean — responds to the freshwater inputs in the Atlantic Ocean. Finally, Chapter 10 points out the main conclusions and final considerations of this thesis.

## CHAPTER 2

---

# Climate evolution since the Last Glacial Maximum

---

**I**N 1941, Milankovitch proposed that the size of ice sheets was controlled by orbital variations, which are expressed in terms of summer insolation changes at high latitudes. Thirty-five years later, Hays et al. (1976) showed that, during the Quaternary (the last  $\sim 2.6$  million years), the Earth experienced ice age cycles at similar intervals to the main periods of orbital variations. The Last Glacial Maximum (LGM) ended at approximately 19 ka (ka: thousands of years ago), when the summer insolation at the Northern Hemisphere increased enough to make the ablation rates exceed the snow accumulation rates, thus triggering the melting of the large ice sheets (e.g., Milankovitch, 1941; Berger, 1978; Clark et al., 2009). The climate evolution after this trigger, however, does not seem to have been controlled by orbital variations only, but also by a set of internal responses of the climate system (Ruddiman, 2008). The last deglaciation, from 19 ka to 10 ka, was the most recent natural climate change,

when CO<sub>2</sub> increased by ~ 70-80 ppmv. This rise is comparable to the one generated by emissions since the Industrial Revolution (Karl and Trenberth, 2003). Therefore, studying this period of the Earth's history allows us to observe how the climate system acts and reacts to changes in its multiple components.

## 2.1 Climate state at 21,000 years ago

The last ice age registered in proxy data<sup>1</sup> began around 100,000 years ago (Kukla et al., 2002). Its peak — when the ice sheets reached their maximum extent — was around 21 ka, period which is referred to as the Last Glacial Maximum (LGM, Mix et al., 2001). The LGM ended when the increasing summer insolation in the Northern Hemisphere (NH) triggered the most recent deglaciation.

Twenty-one thousand years ago, the Earth had mean temperatures of  $4.0 \pm 0.8^\circ\text{C}$  (Annan and Hargreaves, 2013), the sea level was ~130 m below the present one (Clark et al., 2009), and all this missing water was stored in ice sheets that covered most of North America (i.e., the Laurentide Ice Sheet), Northern Europe, and Eurasia. Figure 2.1 shows the extent and thickness of these ice sheets at the LGM, which are provided by the ICE-5G data set (Peltier, 2004).

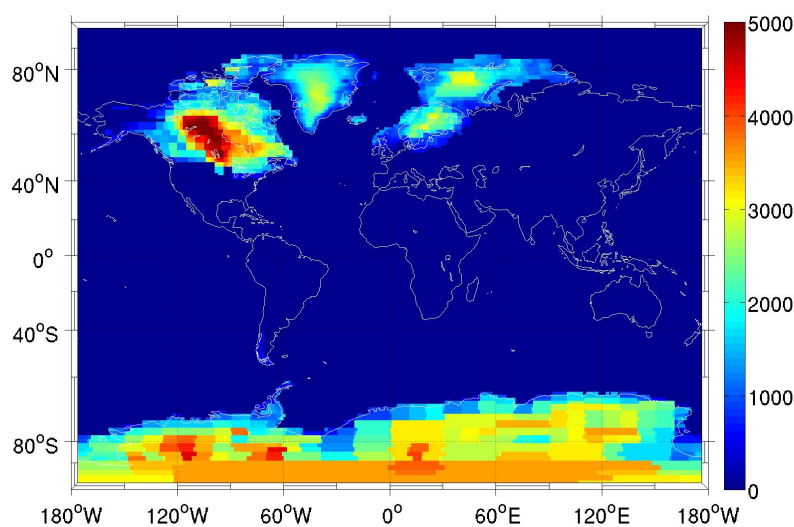


**Figure 2.1:** Ice sheet thickness (m) given by ICE-5G (Peltier, 2004) at 21,000 years ago.

<sup>1</sup>Climatic parameters, such as temperature, inferred from biotic, geological, or geochemical records.

Then, what would cause the Earth's climate 21 ka to be so different from the present state? First, the presence of the ice sheets itself contributed to keep the low temperatures, since the high albedo of the ice reflects more than absorbs the solar radiation. Second, the atmospheric GHG concentrations of these two periods are very different. The CO<sub>2</sub> and CH<sub>4</sub> concentrations were ~190 ppmv and 350 ppbv at the LGM (Monnin et al., 2001), about 68% and 40% of present levels, respectively. Moreover, Alley and Clark (1999) showed that the stronger glacial winds may have contributed to the low temperatures through the increased mixing and upwelling in the tropics.

## 2.2 The last deglaciation

The last deglaciation started (around 19 ka) as soon as the summer insolation at northern high latitudes began to increase. The insolation increased gradually up to ~12 ka, when it reached a maximum and started decreasing toward present levels (Figure 2.2(a)). This solar radiation increase is, however, small compared with the climate changes observed during the deglaciation. This implies the existence of positive feedbacks that amplify the climate system responses. In fact, variations on sea level, albedo and GHG concentrations seem to have assumed this role (Alley and Clark, 1999).

The last deglaciation was a highly variable climatic period, consisting of oscillations with periods that go from 1,500 to 100,000 years and overlap each other, alternating warm and cold phases. The slowest oscillations are related to Milankovitch cycles — fluctuations of the orbital parameters which determine the amount of solar radiation received at the Earth's surface. The shorter oscillations are probably related to ice sheet and deep ocean circulation changes (Alley and Clark, 1999). The ~1,500-year oscillations are called the Dansgaard-Oeschger (D-O) cycles (Bond and Lotti, 1995; Bond et al., 1997), which manifest themselves through abrupt changes in temperature. After several successively colder D-O cycles, a Heinrich event may

occur (Heinrich, 1988; Bond et al., 1993). The Heinrich events were first described by Hartmut Heinrich (1988) and are characterized by massive iceberg discharges into the North Atlantic. These events are identified in the geological records as sediment layers of fast deposition. As the icebergs drift and melt, they leave behind freshwater and debris of variable sizes, the so-called Ice Rafted Debris (IRD) (e.g. Keigwin and Lehman, 1994). The debris sink to the bottom of the ocean and are buried afterwards, forming a distinct layer at sediment cores. The cause of the Heinrich Events is not well established, but explanations go from internal instabilities of ice sheets (MacAyeal, 1993) to increase in sea surface temperature (Marcott et al., 2011). The Heinrich events are commonly followed by abrupt warmings.

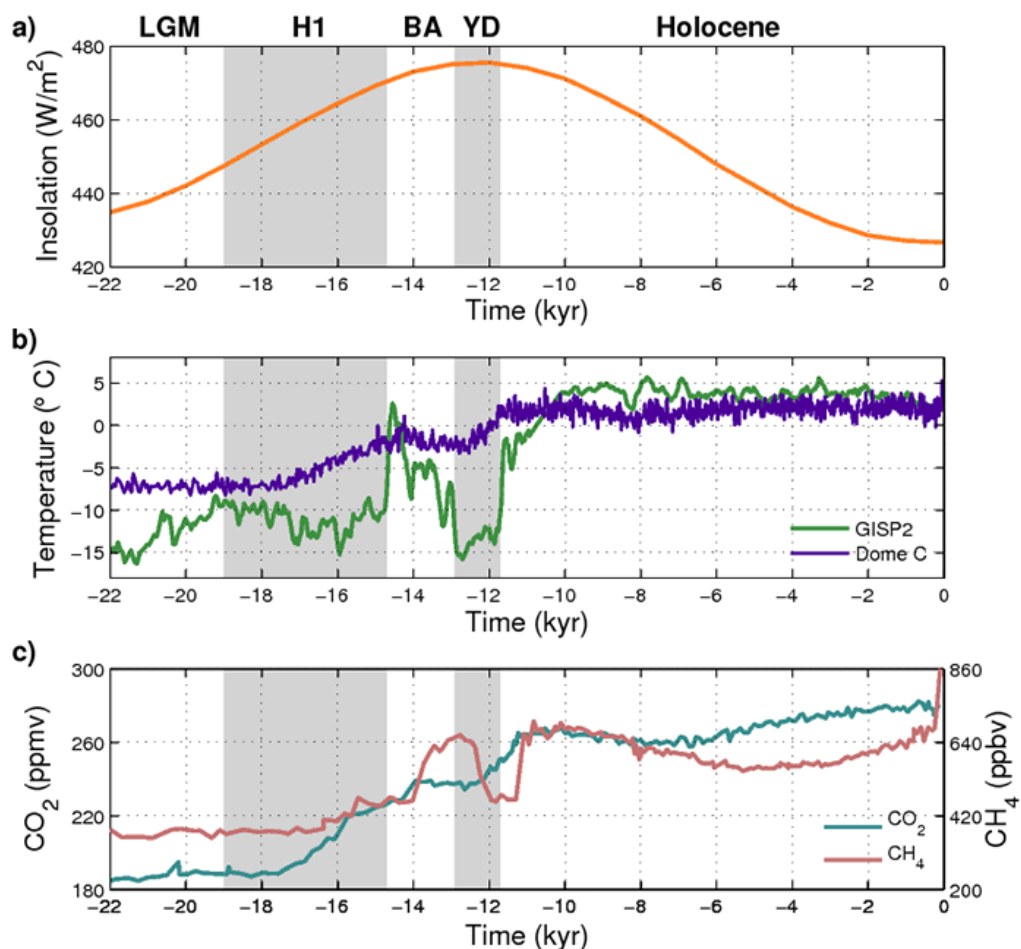


**Figure 2.2:** (a) Insolation<sup>2</sup>, (b) Antarctic (Dome C, purple line, Jouzel et al., 2007) and Greenland (GISP2, green line, Alley, 2000a) temperatures, and (c)  $\text{CO}_2$  (Lüthi et al., 2008) and  $\text{CH}_4$  (Loulergue et al., 2008) concentrations in the atmosphere since 21 ka.

<sup>2</sup>Data obtained at <ftp://ftp.ncdc.noaa.gov/pub/data/paleo/insolation/>

Considering the millennial oscillations cited above, the last deglaciation consisted of a sequence of five climatic periods that can be observed in the Greenland surface air temperature (SAT) evolution, reconstructed from ice cores collected during the Greenland Ice Sheet Project 2 (Alley, 2000a, Figure 2.2(b), green line): the Oldest Dryas (cold, from 19 to 14.7 ka), the Bølling (warm, from 14.7 to 14 ka), the Older Dryas (cold, from 14 to 13.7), the Allerød (warm, from 13.7 to 12.9 ka), and the Younger Dryas (cold, from 12.9 to 11.7 ka)<sup>3</sup>. The Heinrich event 1 (H1) occurred during the Oldest Dryas. Commonly, the H1 is dated from 17.5 to 16 ka based on the layer of IRD in NH sediment cores. Stanford et al. (2011), conversely, define the Heinrich Stadial 1 in a broader sense, placing it between 19 ka and 14.6 ka. The authors divide the H1 in three main phases: the onset of meltwater release at ~19 ka; the 'conventional' H1 IRD deposition phase starting at about 17.5 ka; and the final phase between 16.5 and ~15 ka, marked by pooling of freshwater in the Nordic Seas. Based on this broader definition, the H1 is placed in a period as long as the Oldest Dryas itself. Because of that, the period between 19 ka and 14.7 will be referred to, hereafter, as H1. Moreover, since the Older Dryas was quite fast and sometimes cannot be identified in low resolution records, this period is often omitted and the interval from 14.7 to 12.9 ka is merged as the Bølling-Allerød.

Having the above discussion in mind, here we simplify and divide the deglaciation in three climatic episodes that mark dramatic transitions of temperature, greenhouse gases concentration, sea level, and massive iceberg discharges. They are:

- **Heinrich Stadial 1 (H1):** from 19 to 14.7 ka;
- **Bølling-Allerød (BA):** from 14.7 to 12.9 ka;
- **Younger Dryas (YD):** from 12.9 to 11.7 ka.

The H1 marked the end of LGM with the first meltwater discharges, causing the sea level to rapidly rise ~10-15 m at around 19 ka (Yokoyama et al., 2000). During the H1, the temperature decreased about 4°C followed by an increase of 2~3°C

---

<sup>3</sup>The dates are estimates because there is still controversy about the periods' boundaries chronology.

before the beginning of the BA (Figure 2.2, top). At around 14.7 ka, the BA terminated the H1 with a sharp air temperature increase in the Northern Hemisphere —  $\sim 13^{\circ}\text{C}$  in less than 150 years (Cuffey and Clow, 1997). During the BA, a meltwater discharge responsible for a rapid sea level rise of  $\sim 20$  m in less than 150 years took place and was named **meltwater pulse 1A** (MWP-1A Fairbanks, 1989). The Younger Dryas followed the Allerød with a temperature decrease of  $\sim 9^{\circ}\text{C}$  in about 200 years, which made this period almost as cold as the glacial interval. During the YD, a new iceberg discharge took place at the NH (the Heinrich event 0, Andrews et al., 1995) accompanied by increased freshwater fluxes in the North Atlantic. The YD ended at 11.7 ka with a 5 to  $10^{\circ}\text{C}$  increase in Greenland SAT (Alley, 2000b). After that, the components of the climate system stabilized, marking the beginning of the Holocene. In total, Greenland temperatures increased by  $15^{\circ}\text{C}$  between the LGM and the late Holocene (e.g., Cuffey and Clow, 1997).

These events were observed in climate records all around the planet, almost synchronic with the NH. However, looking at the Antarctic temperature evolution registered in the Dome C ice core (Jouzel et al., 2007) it can be seen that the southern high latitudes behave quite differently than their northern counterpart (Figure 2.2(b), purple line). Blunier and Brook (2001) showed that, in the last 90,000 years, significant increases in Greenland temperature were preceded by Antarctica by 1,500-3,000 years — interval that coincides with the period of the D-O oscillations. Because of that, it is possible to observe a phase opposition between Greenland and Antarctica temperature time series, which means that warm periods in one place coincide with cold periods in the other one. This behaviour is known as **bipolar seesaw** (Broecker et al., 1998), but it is not exactly symmetric around the equator. While the "northern behaviour" is observed broadly around the world, the "southern behaviour" is only observed in the South Atlantic, Central Indian and Deep Pacific Ocean (Alley and Clark, 1999). It is believed that the "southern behaviour" is transmitted through the ocean along hundreds of years, while the "northern behaviour" is transmitted via atmosphere, allowing the observed global synchronicity (Alley and Clark, 1999).

Figure 2.2(c) shows the temporal evolution of two important greenhouse gases: CO<sub>2</sub> and CH<sub>4</sub>. The CO<sub>2</sub> concentrations rise in a two-step fashion: from the early H1 (~17 ka) to the beginning of the BA (14.7 ka) and from the end of the BA (12.9 ka) to the end of YD (11.7 ka), when it reaches interglacial levels. CH<sub>4</sub> concentrations also start to rise around 17 ka and jump abruptly from ~450 to 640 ppbv during the BA, followed by a sharp decrease back to ~450 ppbv at the YD (12.9 ka). At the end of the YD, CH<sub>4</sub> concentrations jump to 650 ppbv again. An interesting feature pointed by Alley and Clark (1999) can be observed in these time series: CO<sub>2</sub> variations follow Heinrich events because these events affect especially ocean processes which, in turn, control atmospheric CO<sub>2</sub> concentrations. On the other hand, CH<sub>4</sub> oscillates with D-O events, because one of the main sources of CH<sub>4</sub> — the wetlands — are closely related to the monsoonal regime, which is affected by the temperature swings that characterize D-O events.

## 2.3 The Holocene

During the deglaciation, the large amplitude of climate variability is attributed to the presence of huge ice sheets, which amplify climatic responses (e.g., Mayewski et al., 2004). In the Holocene, however, most of the ice sheets had melted and the main forcing of climate variations became the seasonal contrast of incoming solar radiation (Bond et al., 2001). This contrast was reflected on changes in the hydrological cycle and monsoonal systems (Otto-Bliesner et al., 2006; Mayewski et al., 2004) which, in turn, were expressed in surface changes in vegetation, lake levels in Asia and northern Africa, and expansion of the boreal forest at the expense of tundra at mid- to high latitudes of the NH (Prentice and Jolly, 2000). Although the climatic variability during the Holocene is fairly stable when compared to the one during the deglaciation, there are some characteristics and episodes that are worth mentioning.

Bond et al. (1997) recognized eight cold events during the Holocene: at 11.1 ka, 10.3 ka, 9.4 ka, 8.2 ka, 5.9 ka, 4.2 ka, 2.8 ka and 1.4 ka. The authors discuss

that the probable cause for these events was an ocean surface cooling brought by changes in North Atlantic's surface circulation. The most notable event is the 8.2 ka one, when climatic deviations were about half as large as those of the YD (Alley et al., 1997). Around this time, the temperatures cooled by 3°-6°C over Greenland and the snow accumulation decreased 20% (Alley et al., 1997). Another cold event, which happened around 400 years ago, was called the Little Ice Age and followed the Medieval warm period. Several of those Holocene cold events led to the collapse and reconstruction of human civilizations (Mayewski et al., 2004). The last major meltwater discharges occurred with the melting of the remaining Eurasian Ice Sheet (around 8 ka) and Laurentide Ice Shees (around 7 ka, Carlson et al., 2008).

## CHAPTER 3

---

# The transient simulation TraCE-21K

---

**N**UMERICAL models provide "full-picture" scenarios when observations cover only punctual locations and times. In the past decades, several numerical studies determined the paleocean state for specific time slices. Here, with the aid of advanced computational resources, we use the results of the first transient simulation of the last 22,000 years (called TraCE-21K), based on the NCAR-CCSM3 model. With prescribed greenhouse gas concentrations in atmosphere, insolation levels, meltwater fluxes that resemble sea level rise records, and changes in ice sheets and coast lines configuration, the simulation successfully reproduced the main climatic periods since the Last Glacial Maximum.

### 3.1 NCAR-CCSM3 numeric model

The Climate Community System Model (CCSM) is a global coupled model developed at the National Center for Atmospheric Research (NCAR). It is composed of four com-

ponents: atmosphere, ocean, land surface and sea ice (Boville and Gent, 1998). The atmospheric component of this model is the Community Atmospheric Model (CAM) version 3 with a  $\sim 3.75^\circ$  in horizontal resolution and 26 hybrid coordinate levels in the vertical (Collins et al., 2006). The land model uses the same resolution as the atmospheric model, and allows the user to specify glaciers, lakes, wetlands, urban areas, and vegetated regions.

The ocean component of this model is the Parallel Ocean Program (POP), a three-dimensional primitive equation model in vertical z-coordinate (Gent et al., 2006). The ocean grid has a dislocated north pole over Greenland, and 25 levels extending to 5.5 km depth. Its horizontal resolution is approximately  $3.6^\circ$  in longitude and is variable along latitudes, with greater resolution in the tropics and North Atlantic. The sea ice model uses the same horizontal grid and land mask as the ocean model, and has a dynamic–thermodynamic formulation, which includes a sub-grid-scale ice thickness distribution and elastic–viscous–plastic rheology (Briegleb et al., 2004).

## 3.2 TraCE-21K settings

The simulation analyzed is referred to as TraCE-21K, and it is the final result of several sensitive experiments generated by He (2011) in his effort to constrain meltwater flux rates and locations that best reproduced Greenland SAT records, the Atlantic Meridional Overturning Circulation (AMOC) strength reconstructions, and other proxy data. The final run spans from 22 ka to 0 ka, which includes the LGM, all the main climatic events of the last deglaciation, and the Holocene. The present day (0 ka) in the simulation represents year 1950. He (2011) explains that at each millennial event, several sensitive experiments were performed with the same initial condition, but different meltwater schemes in terms of rates and location of meltwater discharge. After taking into consideration the sea level records, indicators of the meridional ocean circulation strength, and Greenland temperature records, he chose the experiment that best matched the proxy data to continue the transient run (see Figure 3.1). TraCE-21K

is an extended version of the DGL-A experiment discussed in Liu et al. (2009).

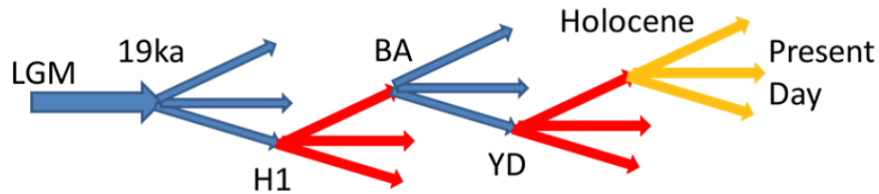


**Figure 3.1:** Schematic of the strategy for TraCE-21K. At the beginning of each important climatic event, several sensitive experiments were performed with different meltwater schemes. The most successful experiment reproducing proxy data was chosen to continue the transient run. Figure adapted from He (2011).

The TraCE-21K run was initialized using the results of the LGM CCSM3 simulation described by Otto-Bliesner et al. (2006). The LGM CCSM3 has prescribed concentrations of atmospheric greenhouse gases based on ice core measurements (Flückiger et al., 1999; Dällenbach et al., 2000; Indermühle et al., 2000) and are given in Otto-Bliesner et al. (2006, their Table 1) as are the atmospheric aerosols. The concentrations of atmospheric carbon dioxide ( $\text{CO}_2$ ), methane ( $\text{CH}_4$ ) and nitrous oxide ( $\text{N}_2\text{O}$ ) are reduced compared to the pre-industrial values, resulting in a total decrease in radiative forcing of the troposphere of  $2.76 \text{ Wm}^2$ . The majority of this change ( $2.22 \text{ Wm}^2$ ) results from a decrease in the amount of  $\text{CO}_2$ . Continental ice sheet extent and topography in the LGM CCSM3 simulation come from the ICE-5G reconstruction (Peltier, 2004). The coastline is also taken from the ICE-5G reconstruction and corresponds to a sea level  $\sim 120 \text{ m}$  below the present one. The orbital parameters at 21 ka (Berger, 1978) are used to determine the total solar flux. The LGM CCSM3 ocean was initialized by applying anomalies of the ocean three-dimensional potential temperature and salinity fields derived from a LGM run with the Climate System Model version 1.4 (CSM1.4, Shin, 2003). Starting the simulation with a previous LGM run that reached quasi-equilibrium allows a shorter spin-up phase. The LGM CCSM3 equilibrium was run coupled to a vegetation module (CLM-DGVM, Levis et al., 2004) for 1800 years before initializing the TraCE-21K simulation.

The initial fields present a colder and saltier deep ocean compared to the present-day thermohaline structure, which is in agreement with previous studies (Ad-

kins et al., 2002). The North Atlantic, in particular, presents a very dense vertical profile in the subsurface and deep ocean, which gives the LGM ocean its highly stratified characteristic. For the prescribed forcing fields, TraCE-21K adopted transient orbital parameters and transient greenhouse gases concentrations ( $\text{CO}_2$ ,  $\text{CH}_4$  and  $\text{N}_2\text{O}$ ) from Joos and Spahni (2008). The ice sheets volume changed every 500 years according to ICE-5G reconstruction (Peltier, 2004). The coastlines were also taken from ICE-5G and were modified at 13.1 ka (removal of the Fennoscandian Ice Sheet from the Barents Sea), 12.9 ka (opening of the Bering Strait), 7.6 ka (opening of Hudson Bay), and 6.2 ka (opening of the Indonesian throughflow). The changes in the coastlines also reflects the sea level variability.

The meltwater scheme (summarized in Figure 3.2(a)) and their locations (shown in Figure 3.2(b)) for this simulation are detailed in the Table 3.1. The meltwater flux rates were chosen based on sea level records presented in Clark and Mix (2002) and Peltier (2004), and on geological indicators of ice sheet retreat and meltwater discharge from Licciardi et al. (1999), Clark et al. (2001, 2002a), Clark et al. (2004), and Carlson (2009). As the sea level records do not constrain the locations where the meltwater fluxes come from, these locations were chosen according to the AMOC sensitivity to freshwater input in that particular region. There is a trend of lower sensitivity of the AMOC to the meltwater forcing in more southerly latitudes. Therefore, the Beaufort Sea/Mackenzie River discharge, Nordic Sea and  $50^\circ$ - $70^\circ\text{N}$  of North Atlantic are the three regions with larger sensitivity, while the sensitivity of the Southern Ocean is very small (He, 2011).

The meltwater discharges were added to the ocean model as a freshwater flux to the ocean surface (He, 2011). This allows the low salinity signal to spread freely in the global ocean. The freshwater flux rate applied on each grid cell of the chosen region was obtained by dividing the corresponding sea level rise by the total area where the freshwater was inserted. The unit for the meltwater discharge is given in m/kyr (meters of equivalent sea level volume per thousand years). Since the area of the ocean is about  $3.61 \times 10^{14} \text{ m}^2$ , 1 m/kyr means  $3.61 \times 10^{14} \text{ m}^3$  volume of meltwater

in  $10^3$  years, which is  $0.011 \text{ m}^3/\text{s}$ , or  $0.011 \text{ Sv}$ .

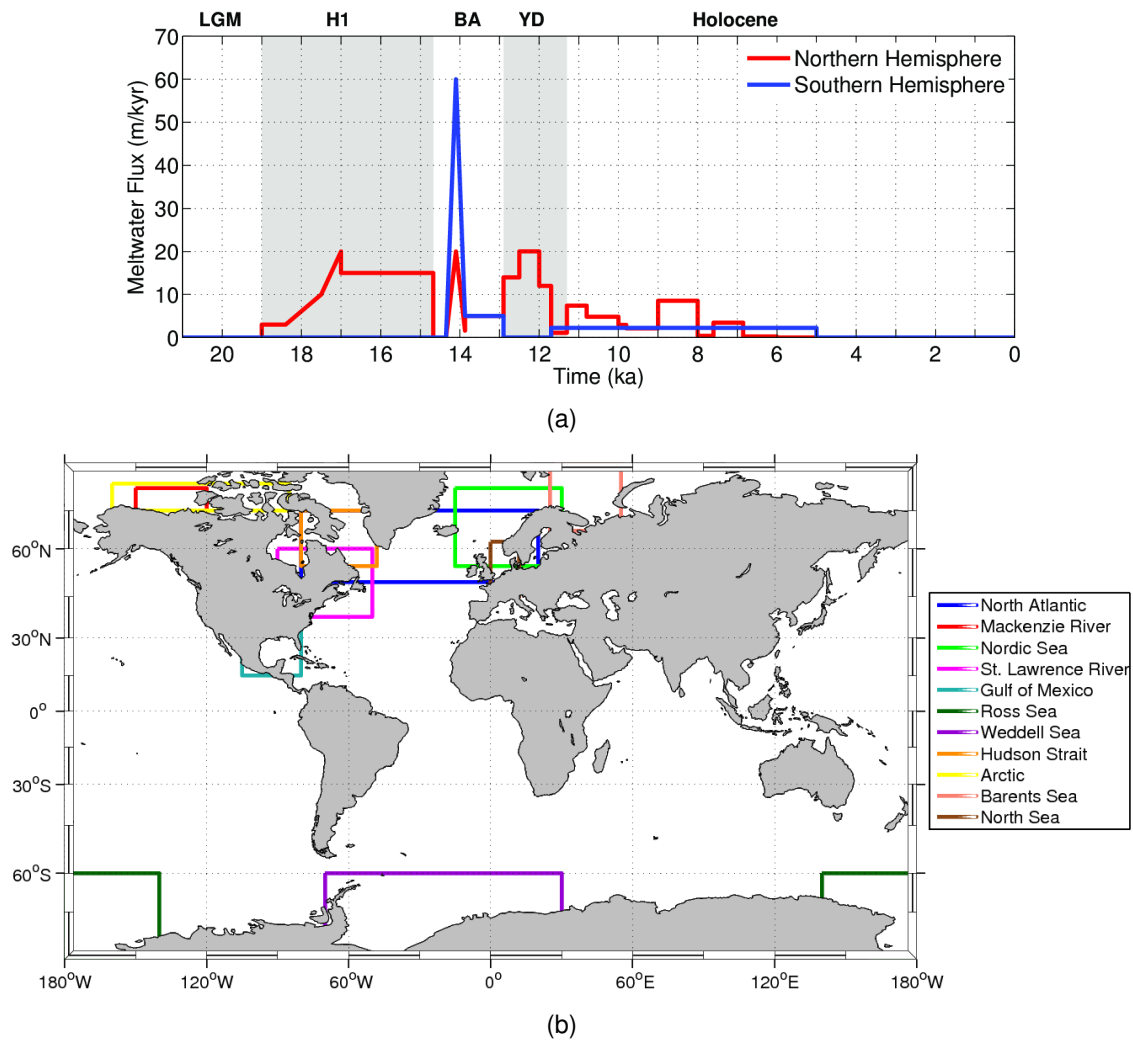


**Figure 3.2:** (a) Sum of meltwater flux rates prescribed in each hemisphere in TraCE-21K ( $1 \text{ m/kyr}=0.011 \text{ Sv}$ ) and (b) regions where the meltwater fluxes were prescribed (He, 2011).

In TraCE-21K, the end of the Bølling warming is attributed to the meltwater pulse 1A (MWP-1A), which triggered the Older Dryas cooling (He, 2011; Liu et al., 2009). The idea of the causal link between MWP-1A and Older Dryas cooling has been also proposed based on proxy records (Stanford et al., 2006). Although the origins of the MWP-1A are still under debate, He (2011) followed the estimates of sea level records that point out to a 5 m contribution from the NH and 15 m from Antarctica (Clark et al., 2002b; Bassett et al., 2005), totalling the approximate 20 m sea level rise registered for this event (Fairbanks, 1989). Any larger contribution from the Northern Hemisphere would result in a complete shutdown of the meridional overturning

circulation, which is inconsistent with proxy records (McManus et al., 2004).

Year (ka)	NHMW (m/kyr)	NHMW location	SHMW (m/kyr)	SHMW location
22.00 to 19.00	-	-	-	-
19.00 to 18.40	3	North Atlantic	-	-
18.40 to 17.50	Ramping 3 to 5	North Atlantic	-	-
	Ramping 0 to 5	Gulf of Mexico	-	-
17.50 to 17.00	Ramping 5 to 15	North Atlantic	-	-
	5	Gulf of Mexico	-	-
17.00 to 14.67	15	North Atlantic	-	-
14.67 to 14.35	-	-	-	-
14.35 to 14.10	Ramping 0 to 10	Mackenzie River	Ramping 0 to 30	Ross Sea
	Ramping 0 to 10	Gulf of Mexico	Ramping 0 to 30	Weddell Sea
14.10 to 13.85	Ramping 10 to 0	Mackenzie River	Ramping 30 to 0	Ross Sea
	Ramping 10 to 0	Gulf of Mexico	Ramping 30 to 0	Weddell Sea
13.87 to 12.90	1	Nordic Sea	5	Ross Sea
13.87 to 13.40	4	Gulf of Mexico	-	-
13.40 to 12.90	2.4	Gulf of Mexico	-	-
	1.6	St. Lawrence River	-	-
12.90 to 12.50	14	St. Lawrence River	-	-
12.50 to 12.20	20	St. Lawrence River	-	-
12.20 to 12.00	6	St. Lawrence River	-	-
	14	Mackenzie River	-	-
12.00 to 11.70	12	St. Lawrence River	-	-
11.70 to 11.30	0.15	St. Lawrence River	1.12	Weddell Sea
	0.29	Hudson Strait	1.12	Ross Sea
	0.15	Arctic	-	-
	0.38	North Sea	-	-
	0.13	Barents Sea	-	-
11.30 to 10.80	0.55	Arctic	1.12	Weddell Sea
	0.55	St. Lawrence River	1.12	Ross Sea
	1.03	Hudson Strait	-	-
	1.32	Barents Sea	-	-
	3.96	North Sea	-	-

10.80 to 10.00	0.55	Arctic	1.12	Weddell Sea
	0.55	St. Lawrence River	1.12	Ross Sea
	1.03	Hudson Strait	-	-
	0.68	Barents Sea	-	-
	2.03	North Sea	-	-
10.00 to 09.80	0.55	Arctic	1.12	Weddell Sea
	0.55	St. Lawrence River	1.12	Ross Sea
10.00 to 09.80	1.03	Hudson Strait	-	-
	0.20	Barents Sea	-	-
	0.60	North Sea	-	-
09.80 to 09.00	0.55	Arctic	1.12	Weddell Sea
	0.55	St. Lawrence River	1.12	Ross Sea
	1.03	Hudson Strait	-	-
09.00 to 08.00	0.42	Arctic	1.12	Weddell Sea
	0.42	St. Lawrence River	1.12	Ross Sea
	7.47	Hudson Strait	-	-
	438 <sup>1</sup>	Hudson Strait	-	-
08.00 to 07.60	0.02	Arctic	1.12	Weddell Sea
	0.02	St. Lawrence River	1.12	Ross Sea
	0.33	Hudson Strait	-	-
07.60 to 06.85	0.17	Arctic	1.12	Weddell Sea
	0.17	St. Lawrence River	1.12	Ross Sea
	3.13	Hudson Strait	-	-
06.85 to 06.00	0.01	Arctic	1.12	Weddell Sea
	0.01	St. Lawrence River	1.12	Ross Sea
	0.21	Hudson Strait	-	-
06.00 to 05.00	-	-	1.12	Weddell Sea
	-	-	1.12	Ross Sea
05.00 to 00.00	-	-	-	-

**Table 3.1:** Meltwater flux rates and locations prescribed on TraCE-21K (1 m/kyr=0.011 Sv).  
NHMW: Northern Hemisphere Meltwater; SHMW: Southern Hemisphere Meltwater.

<sup>1</sup>At 8.47 ka for half a year

### 3.3 Simulation performance

He (2011) points out that between H1 and the onset of BA the sea level stabilized, which suggests a minimal meltwater discharge during this period. Yet, even with no meltwater input, the AMOC remained at a near-collapse state during this period, which could be explained invoking AMOC hysteresis (e.g., Hofmann and Rahmstorf, 2009; Hawkins et al., 2011). Because CCSM3 has a weak AMOC hysteresis (Liu et al., 2009), it was necessary to induce substantial sea level rise in order to maintain a near-collapsed AMOC between H1 and BA.

At the onset of BA, the Greenland SAT increases by about 13°C in the simulation, which is in good agreement with SAT georeconstructions in terms of amplitude. However, the rate of the simulated Greenland warming is ~40% slower than that from reconstructions: the simulation takes about 350 years to increase Greenland's temperature by 13°C, while the reconstructions suggest that this abrupt warming took only ~200 years to happen (He, 2011).

Proxy data indicate that the AMOC did not collapse during the YD, which implies that the AMOC reduction during YD is smaller than during H1. In the simulation, the maximum meltwater discharge rate that allowed AMOC to weaken but not shut-down was 10 m/kyr. This meltwater flux led to a cooling of merely 2°C, compared to the 8~10°C cooling on Greenland SAT reconstructions. Even with a larger meltwater discharge and a collapsed AMOC, the temperature decreases only by 3-5°C. He (2011) explains that, besides AMOC strength, the only other change observed during this period that could be involved in YD cooling was in the coastline configuration: the Bering Strait was opened at 12.9 ka. Although the opening of the Bering Strait indeed showed a contribution for a weaker AMOC, its effect on temperature reduction was minimal. Therefore, TraCE-21K could not reproduce all the cooling of Younger Dryas. Besides, with the opening of the Bering Strait at 12.9 ka, the termination of meltwater flux at the end of the YD fails to produce the abrupt warming during the YD-early Holocene transition (He, 2011).

Even though AMOC and Greenland SAT reconstructions show a complete

transition to Holocene by 10 ka, He (2011) opted to keep meltwater discharges in the NH between 10 and 7 ka in order to respect sea level records and geological indicators of ice sheet retreat. As a result, the simulated Greenland SAT is significantly cooler than reconstructions between 10 and 7 ka. Once the meltwater was shutdown, the temperatures reached Holocene levels, which agrees with reconstructions and modern observations.

Despite the above considerations, the simulation reproduced most of the major climatic events of the last deglaciation, suggesting a good agreement in climate sensitivity between the model and observations (Liu et al., 2009). He (2011) highlights that, since TraCE-21K started from the LGM and integrated forward with prescribed GHG concentrations and orbital forcing, the successful simulation of the Holocene temperatures shows that CCSM3 responds adequately to the radiative forcing.

## CHAPTER 4

---

# The Atlantic Ocean's deglacial evolution: Introduction

---

### **4.1 Present-day structure of the deep ocean circulation**

Oceanic motion is driven primarily by two types of forcing: wind stress and buoyancy. In the upper  $\sim 100$  m of the water column, the winds drive horizontal gyres. The Atlantic Ocean has two subtropical gyres (one in each hemisphere), one subpolar gyre in the North Atlantic, and an equatorial system (Figure 4.1). In the Atlantic sector of the Southern Ocean, the Antarctic Circumpolar Current flows eastward. Due to the conservation of potential vorticity, the western boundary currents (WBC) of the gyres are intense and narrow, while the eastern ones are weak (Talley et al., 2011).

Between 1000 and 1500 m, the intermediate depth circulation is forced by Ekman pumping (upwelling and downwelling) generated by wind friction on the surface

layers (Talley et al., 2011).

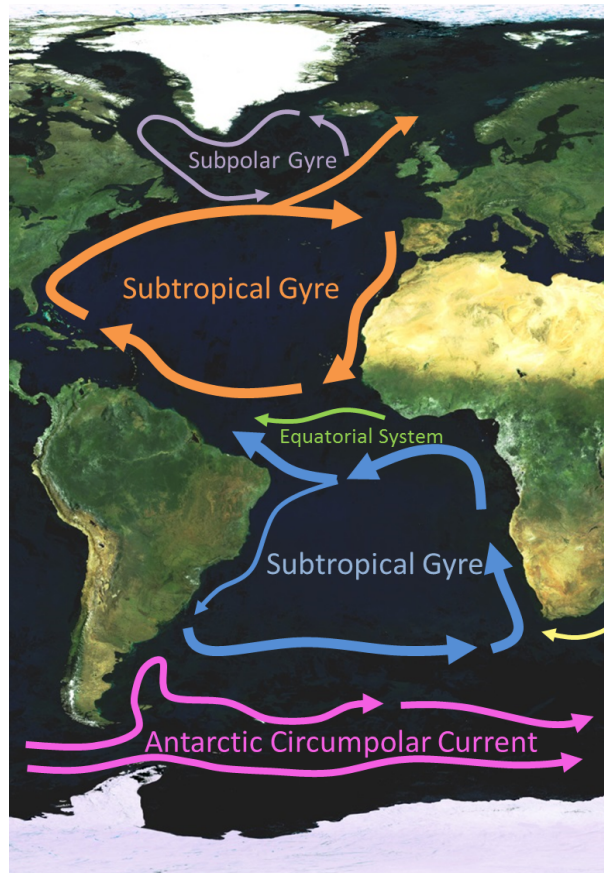


**Figure 4.1:** Simplified scheme of Atlantic Ocean circulation near the surface driven by winds.

At greater depths, the circulation is mostly forced by buoyancy. The flow in the ocean interior is generally weak and easily masked by the eddy field and the deep WBCs (DWBCs) which extend to the bottom - although with reduced strength. The DWBCs in the Atlantic Ocean are the main carriers of newly formed deep waters (Stommel, 1958). The northern DWBC carries North Atlantic Deep Water (NADW) southward at the 2500 m level, while the southern DWBC carries Antarctic Bottom Water (AABW) northward, offshore of and deeper than the NADW's DWBC (Hogg and Owens, 1999). Since DWBCs are the most energetic part of the deep circulation (Talley et al., 2011), the deep flows are essentially meridional when averaged over a long time. A schematic representation of this circulation is shown in Figure 4.2.

The present-day configuration of the Atlantic Meridional Overturning Circulation (AMOC) comprises two cells. The upper cell consists of surface warm waters that flow northward, lose heat to the atmosphere in the northern North Atlantic, and

sink as North Atlantic Deep Water (NADW), which travels southward around 3000 m of depth until  $\sim 40^{\circ}\text{S}$ . The lower cell, in turn, is composed by the NADW flowing southward, mixing with other water masses, upwelling near  $50^{\circ}\text{S}$  and sinking off the Antarctic shelf as Antarctic Bottom Water (AABW), which spreads northward up to the equator (Johnson, 2008). The AMOC carries heat and freshwater across the Atlantic, which is why it is intimately associated with the climate variability.

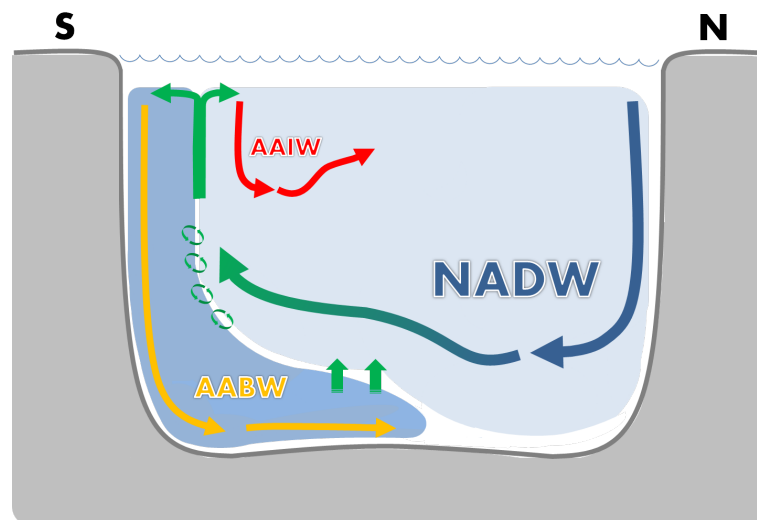


**Figure 4.2:** Simplified scheme of the modern Atlantic Meridional Overturning Circulation (zonally averaged). The North Atlantic Deep Water (NADW) sinks in the northern North Atlantic, travels southward, and upwells in the subtropical front, when it mixes with the newly formed Antarctic Bottom Water (AABW). From there, NADW can go northward, towards the Antarctic Intermediate Water (AAIW) formation region, or southward, becoming a part of the AABW formation. AABW travels northward near the ocean bottom and eventually mixes with NADW in its lower part.

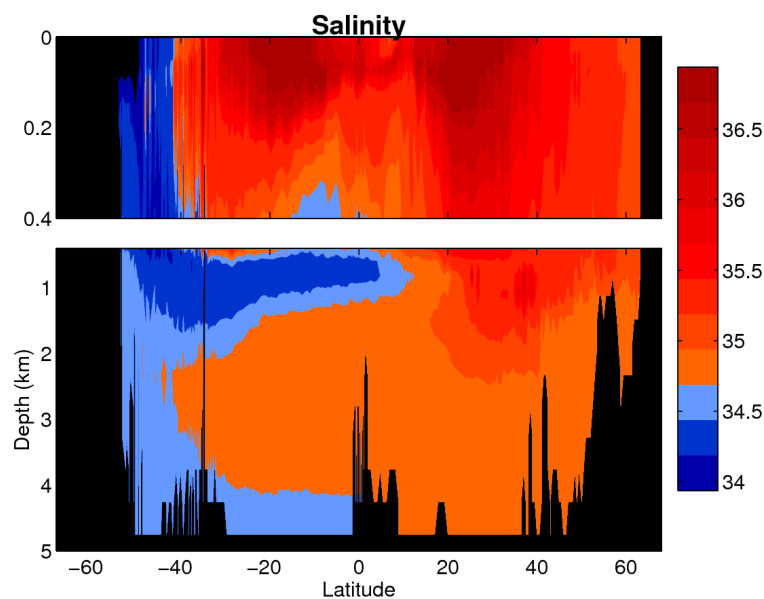
The observation of this meridional circulation, however, is not easily done because of the difficulties in measuring the slow velocities in the ocean interior. Much of what is known about the deep ocean circulation today has been inferred from the distribution of sea water properties, especially temperature and salinity. This indirect analysis is possible based on the concept that the properties of a certain parcel of water are originally acquired at the ocean surface in its formation region. Since temperature and salinity are considered to be fairly conservative properties (i.e., only change at the surface), they function as a signature that allow us to trace the origin (where the parcel intercepts the ocean surface) and dispersion of this water parcel.

Figure 4.3 shows the vertical salinity profile for the Atlantic obtained with data

from the World Ocean Circulation Experiment (WOCE, <http://www.nodc.noaa.gov/woce/>). One can compare this profile with the schematic circulation provided in Figure 4.2 and see that, indeed, salinity is a good tracer for water masses distribution.

Here we define water type and water mass following Tomczak and Large (1989):

- **Water type:** a point in hydrographic parameter space (i.e., each hydrographic property has a single value); it represents the original properties of the water mass, acquired in its formation region (before mixing with other water masses);
- **Water mass:** collection of water parcels that have a common formation history; they are defined by their mean hydrographic properties plus a standard deviation.



**Figure 4.3:** Vertical section at 25°W for the Atlantic Ocean salinity field using data from WOCE (<http://www.nodc.noaa.gov/woce/>).

Any water mass can be represented by a finite number of water types. In other words, each water mass is characterized by small fluctuations around a property extreme. The AABW, for example, has a temperature minimum signature, while the NADW's signature is a salinity maximum at depth. The Antarctic Intermediate Water (AAIW) is characterized by a salinity minimum signature. NADW's high salinity

derives from Gulf of Mexico waters and from eddies that form from the Mediterranean Sea overflow (both with high salinity as a result of the excess of evaporation over precipitation). The temperature minimum characteristic of AABW is due to the freezing waters involved in the formation process of this water mass on the Antarctic continental shelf. AAIW has different formation theories, but its low salt content is either associated with the fresher Pacific waters that enter the South Atlantic via the Drake Passage or with the excess of precipitation over evaporation around 50°S.

## **4.2 Deep ocean circulation changes in the last 21,000 years**

With a significant fraction of water stored in the form of ice, the oceans' mean salinity at the LGM was higher than today. Adkins et al. (2002) showed that, at this time, the waters coming from the Southern Ocean filled the deep Atlantic basin and were characterized by salinities of  $\sim 35.8$  compared to the current  $\sim 34.7$ . The increased salinity is commonly attributed to the enhanced sea ice formation and extension 21,000 years ago (Liu, 2005; Shin, 2003). Adkins (2013) points out another factor that could have contributed to the elevated salinity: the warm deep water of northern origin was colder at the LGM, which could have led to a reduced basal melting of ice shelves and, consequently, a lack of freshwater input in the Southern Ocean waters. The increased salinity of deep waters and the low temperatures of the ocean determined a distinct dynamic behaviour compared to the present day one. At the LGM, the vertical ocean movements were determined by differences in salinity rather than temperature (Adkins et al., 2002), which happens today only in high latitudes or regions under the influence of river runoff. The presence of salty waters near the bottom added to the reduced vertical mixing rates (e.g. Adkins, 2013; Ferrari et al., 2014) resulted in a highly stratified and stable ocean, which reduced the communication between the two cells that compose the AMOC (Ferrari et al., 2014).

Due to the expansion of AABW at the LGM, the boundary between the south-

ern and the northern water masses was around  $\sim 2000$  m (Figure 4.4), compared to the average  $\sim 4000$  m at present (Oppo and Lehman, 1993; Curry and Oppo, 2005; Ferrari et al., 2014). Back in the 1980s, some studies had already pointed to a shoaling of the glacial version of NADW (Boyle and Keigwin, 1987; Duplessy et al., 1988). Today, it is widely accepted that this shoaling indeed happened (e.g., Oppo and Lehman, 1993; Marchitto et al., 1998; Sarinthein et al., 2001; Curry and Oppo, 2005; Lynch-Stieglitz et al., 2007; Otto-Bliesner et al., 2007; Praetorius et al., 2008; Lippold et al., 2012), which led the scientific community to rename the early NADW as Glacial North Atlantic Intermediate Water (GNAIW). Based on proxy data, Boyle and Keigwin (1987) further suggested that GNAIW would have been colder and fresher than NADW.

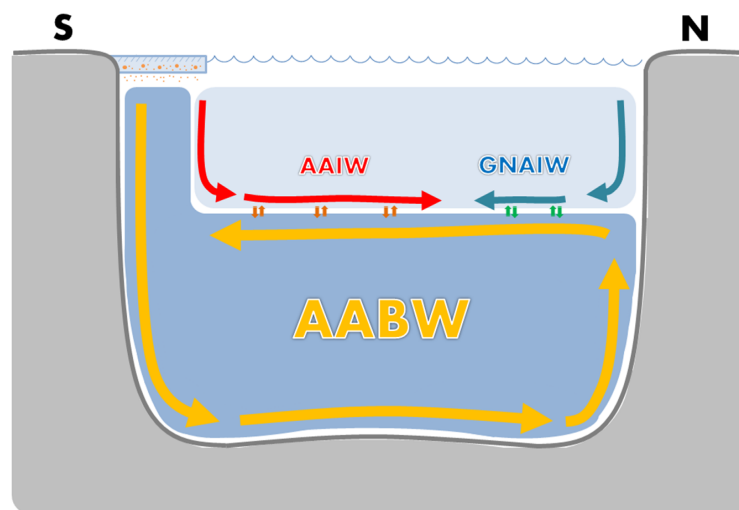


**Figure 4.4:** Simplified scheme of the glacial Atlantic Meridional Overturning Circulation, following the descriptions in Curry and Oppo (2005); Ferrari et al. (2014). The studies suggest that the Antarctic Bottom Water (AABW) occupied most of the Atlantic basin during the last glacial period, forming an almost closed lower cell — since the stratification was stronger and the vertical mixing was reduced. In the intermediate layers, besides the Antarctic Intermediate Water (AAIW), there was an intermediate water mass formed in the northern North Atlantic called Glacial Intermediate North Atlantic Water (GNAIW), that flowed southward.

It is believed that the climate swings that followed the LGM were frequently accompanied by changes in the ocean circulation (e.g., Broecker, 1994; McManus et al., 2004; Praetorius et al., 2008). Proxy records show that during cold periods there were reductions in the AMOC while the warm periods were marked by the AMOC's

recovery (McManus et al., 2004; Came et al., 2008; Ritz et al., 2013, see more details in section 5.1).

Concerning the AAIW, there is still some controversy about how much this water mass penetrated into the North Atlantic during the last deglaciation. Some studies suggest that AAIW could have reached as far north as 60°N (Rickaby and Elderfield, 2005), while others believe this water mass did not reach the subtropical North Atlantic (Xie et al., 2012). Also, the  $\delta^{13}\text{C}$  signature of AAIW in Makou et al. (2010) points to a reduced contact with the atmosphere during glacial AAIW formation, likely due to the presence of sea ice in the region.

The next three chapters present the results obtained from the analysis of TraCE-21K data concerning the deep Atlantic Ocean circulation. Chapter 5 shows the variability of the AMOC since the LGM and its associated heat and salt transports. Chapter 6 describes how the temperature and salinity fields changed during the deglaciation. Chapter 7 presents the water masses distribution across the Atlantic in different important periods. This chapter begins by describing the methodology used to obtain the distribution of water masses — the mixing triangle technique, described by Mamayev (1975).

## CHAPTER 5

---

# The Atlantic Ocean's deglacial evolution: Meridional transports

---

### 5.1 The AMOC

Either (or both) proxy and model data have been widely used in the effort to reconstruct the geometry and strength of the AMOC at the LGM and on (e.g., Duplessy et al., 1988; Yu et al., 1996; Shin et al., 2003; Paul and Schafer-Neth, 2003; Weaver et al., 2003; McManus et al., 2004; Curry and Oppo, 2005; Otto-Bliesner et al., 2006; Stouffer et al., 2006; Clauzet et al., 2007; Lynch-Stieglitz et al., 2007; Otto-Bliesner et al., 2007; Came et al., 2008; Liu et al., 2009; Brady and Otto-Bliesner, 2010; Lippold et al., 2012; Wainer et al., 2012; Ritz et al., 2013). The results of the numerous studies are, however, far from unanimous. Some studies that used proxy records to estimate the intensity of the AMOC point to a vigorous circulation (at least, as strong as today) at the LGM (e.g. Yu et al., 1996; Roberts et al., 2010; Lippold et al., 2012).

Others — sometimes using the same proxies as the studies just cited — interpret the data as a sign of a slower AMOC (e.g. McManus et al., 2004; Negre et al., 2010). In a comprehensive review of several proxy data, Lynch-Stieglitz et al. (2007) believe that the middle path is the best bet: the AMOC was neither stronger nor much slower than today. The authors point out that in several sediment cores no significant difference was found between tracers deposited during the LGM and today, which is consistent with a range of past circulation states (from a slight increase in the AMOC to a decrease of up to 30%). Either way, there seems to be a general agreement about the relationship between AMOC intensity and D-O cycles: AMOC experienced a weakening during Heinrich Stadials (more intense during the H1 than during the YD), followed by rapid increases concurrent with regional warming events during the last deglaciation (McManus et al., 2004; Stanford et al., 2006; Gherardi et al., 2009; Bohm et al., 2014).

Here, TraCE-21K data point to an intensified AMOC at the LGM (Figure 5.1(a)). The upper cell of the overturning is homogeneously strong in both hemispheres while the lower cell shows a vigorous Southern Hemisphere circulation, associated with the intensified AABW formation, occupying most of the deep Atlantic basin. During the H1 (Figure 5.1(b)), the intensified lower cell is still present with the maximum transport of 8–10 Sv confined south of 25°S. The upper cell changes significantly, becoming consistently weaker in both hemispheres. The maximum transport (~10 Sv) at about 1000 m at the LGM is significantly reduced in H1 (max ~4 Sv). During the BA (Figure 5.1(c)) and MPW-1A (Figure 5.1(d)), the deeper circulation of the lower cell weakens while the upper cell intensifies. In the BA, there is an intensification of about 4–6 Sv centered at 1000 m between 20–40°N that is not seen in Figure 5.1(d). The Antarctic Bottom Water picks up again during YD, which is responsible for the re-intensification of the lower cell of the meridional overturning (Figure 5.1(e)), while the upper cell is weakened — except in the upper few hundred meters centered at 20°N. The configuration of the meridional overturning for the Holocene is shown in Figure 5.1(f).

Liu et al. (2009), analyzing the TraCE-21K AMOC variability from the LGM to the BA, found that the BA warming is a response to the sudden interruption of meltwater flux in the North Atlantic at 14.67 ka. This interruption stimulated AMOC to recover and get back to its glacial state ( $\sim 12.5$  Sv, increasing Greenland SAT by  $\sim 5^\circ\text{C}$ ) and overshoot (to 19 Sv, contributing to rise the temperature by other  $10^\circ\text{C}$ ; Liu et al., 2009). The authors explain that the overshoot could be caused by convective instability in the Nordic Sea added to a deep-ocean warming scenario. He (2011) points out that the rate and final amplitude of the AMOC resumption is dependent on the history of meltwater forcing, with faster recovery and larger AMOC overshoot in cases where the meltwater discharge took longer to cease. Moreover, Liu et al. (2009) note that there is almost a linear dependence of Greenland SAT variations on AMOC strength, supporting that AMOC is essential for the temperature control during the deglaciation.

The results suggest that, in CCSM3, the AMOC has multiple equilibria and goes from one state to the other through meltwater discharges onto the ocean surface.

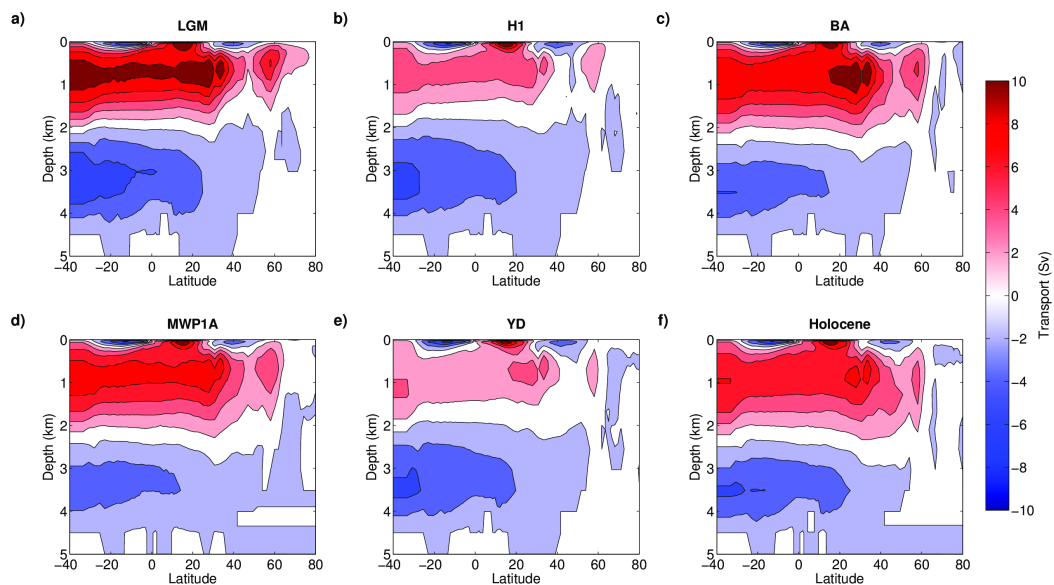


**Figure 5.1:** Atlantic Meridional Overturning Circulation streamfunction and associated transports at six different periods: (a) LGM, (b) H1, (c) BA, (d) MWP-1A, (e) YD, and (f) Holocene. Figure from Marson et al. (2014).

## 5.2 Meridional heat and salt transport

In contrast to the Pacific Ocean, where the heat is transported from the equator to the poles, the meridional heat transport in the South Atlantic is directed northward. This happens because the upper branch of the AMOC carries warm surface layer waters northward to compensate for the outflow of cold waters from the deep North Atlantic (Seidov and Maslin, 2001). Therefore, studying the South Atlantic circulation is instrumental to fully understand the Earth's climate system.

The meridional heat transport was calculated as in Bryan (1962) through a section of the Atlantic basin, using the equation 5.1.

$$Q_t = \int_{5000\text{m}}^0 \int_{70\text{W}}^{20\text{W}} c_p \rho \theta v \, dx dz \quad (5.1)$$

where  $Q_t$  is the meridional heat transport,  $c_p$  is the sensible heat of seawater,  $\rho$  is seawater density,  $v$  is the meridional velocity and  $\theta$  is the potential temperature. The meridional salt transport was calculated in the same way, simply substituting  $c_p\theta$  by  $S$ , where  $S$  is the salinity of seawater.

The northern ocean heat transport (NOHT) for the South Atlantic (0–30°S) is shown in Figure 5.2(a) (purple curve). Apart from the cold LGM period, positive values – which indicate northward transport – coincide with warm periods in the Northern Hemisphere. A sharp increase of the NOHT at  $\sim 14.7$  ka (which coincides with the Bølling–Allerød (BA) warming in the north) is evident. The heat transport is higher at LGM than at modern times, which is consistent with the hypothesis that the AMOC was stronger at 21 ka as discussed by Shin (2003) and Clauzet et al. (2007). Near-zero and negative meridional heat transport are associated with the Northern Hemisphere cooling relative to the H1 and Younger Dryas (YD) events, while the temperature increases in the Southern Hemisphere. After 11 ka, the heat transport values show a steady, small rise to about 0.25–0.3 PW until about 6 ka after which it remains practically constant at that level, indicating a stable equilibrium at the same time that the meltwater pulses are shutdown in the simulation.

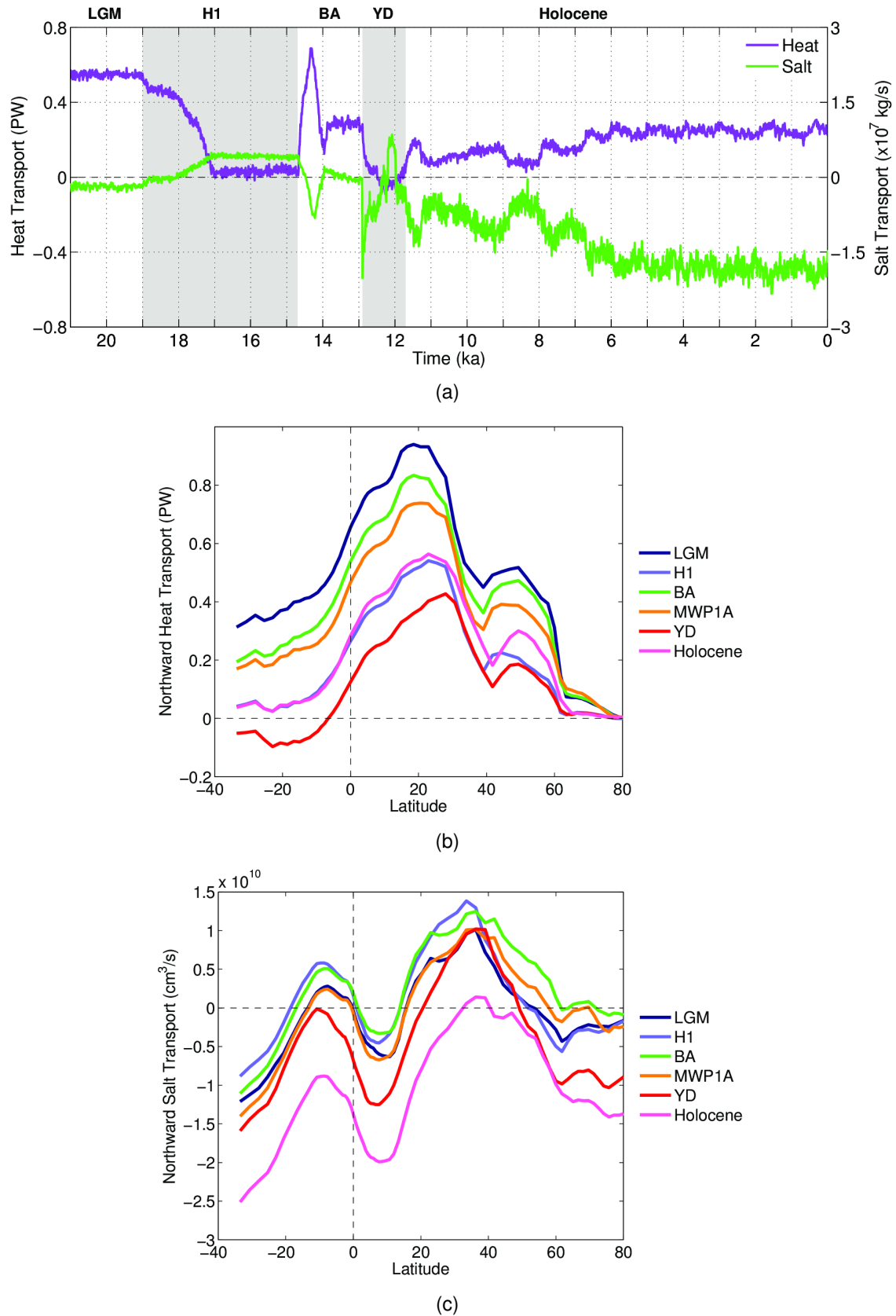


**Figure 5.2:** TraCE-21K meridional heat (purple) and salt (green) transport between  $30^\circ\text{S}$  and  $0^\circ$  (a). Positive values denote northward transport. The main climatic events in the last deglaciation are also marked: Last Glacial Maximum (LGM), Heinrich event 1 (H1), Bølling–Allerød (BA), Younger Dryas (YD) and Holocene. Northward transport of heat (PW) (b) and northward transport of salt ( $\text{cm}^3/\text{s}$ ) (c), averaged for each millennial event of the last 21,000 years. Figure from Marson et al. (2014).

The NOHT as a function of latitude averaged for each of the key millennial events in the simulation is shown in Figure 5.2(b). NOHT has a maximum in the North Atlantic in the tropics, centered at 20°N for the LGM and BA. This maximum shifts a few degrees north for the MWP-1A period. For the YD and Holocene, the maximum northward transport is at about 25°S and 30°S, respectively. The changes in magnitude of the NOHT between the periods are related to air–sea interaction in the tropics as discussed by Cheng et al. (2007). They discuss the AMOC slowdown, the related NOHT and the mechanisms for the high-latitude tropical coupling through freshwater perturbation experiments. In the South Atlantic, with exception of the YD, the transport is northward, largest at LGM, decreasing nonlinearly at BA and MWP-1A and very small for H1 and the Holocene.

The northward ocean salt transport (NOST) as a function of latitude is shown in Figure 5.2(c). The NOST between the key millennial events shows its maximum values between 30–40°N with a secondary maximum at 10°S. In the North Atlantic, the ocean salt transport is southward for all periods (except the Holocene) from the Equator to about 20°N, after which it becomes poleward until 60°N, when it reverts to southward. The strongest NOST is during H1, followed by BA, LGM and YD. During the Holocene with the exception of a small, albeit positive, NOST at about 38°N, all the salt transport is southward. In the South Atlantic, there is northward salt transport at H1, BA and LGM, which is reversed southward at YD and Holocene.

The relationship between the TraCE-21K meridional heat transport and the meridional salt transport (Figure 5.2(a), green curve) shows an out-of-phase behavior between the two time series. This is best illustrated by the scatter diagram in Figure 5.3. It shows that the negative correlations between heat and salt transport are high before and after the BA warming period (circles with a correlation coefficient ( $r$ ) of -0.99, and triangles with  $r = -0.93$ , respectively). During the transition from approximately 14.7 ka to 12.9 ka, the correlation diminishes (but is still significant; Fig. 5.3, crosses with  $r = -0.79$ ) due to the reorganization of the deep ocean structure. The different slopes of the circle and triangle clusters in Fig. 5.3 indicate that, overall, the

transport exhibits two regimes: a large heat and small salt transport before BA and a small heat and large salt transport especially after YD (greenish to reddish tones).

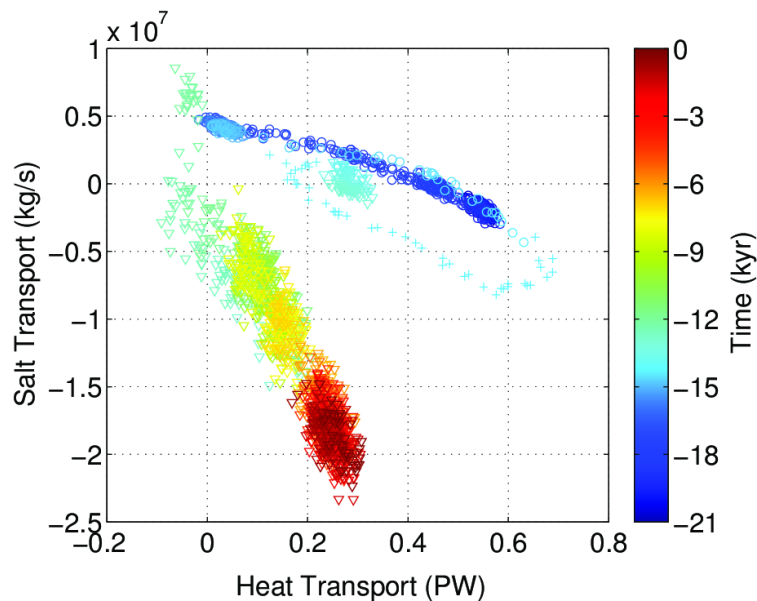


**Figure 5.3:** Scatter diagram showing negative correlation between heat and salt transport in South Atlantic (30–0°S). The circles represent the data for the period that precede the Bølling–Allerød event; the crosses stand for the BA period; and the triangles show data from Younger Dryas on. The colors stand for time evolution, according to the color bar on the right. Figure from Marson et al. (2014).

If we consider the salt transport via water masses, the AABW fills the Atlantic basin from LGM to BA due to the limited extension of GNAIW. After that, the developing NADW starts transporting salt southward, and at the same time there is more heat being transported to the north (as in Seidov and Maslin, 2001). The same is true for AABW at the beginning of the simulation (more glacial AABW means export of salt northward and more heat southward). The increase or decrease in NOHT and NOST is related to the location of the prescribed freshwater fluxes. For example, the MWP-1A that discharged the equivalent of 15 m/kyr of freshwater into the Southern Ocean, where the AABW is formed, would cause its North Atlantic counterpart to transport salt southward more intensely. According to Seidov and Maslin (2001), for example, a stronger NADW is associated with increased northward heat transport, and more salt transported to the south, leading to an inverse correlation.

## CHAPTER 6

---

# The Atlantic Ocean's deglacial evolution: Thermohaline characteristics

---

**T**HE analysis of the Atlantic's salinity and temperature fields reveals changes in its water masses that occurred in the transient simulation. As we will see, several of those changes agree with proxy reconstructions discussed in section 4.2. We begin presenting the salinity vertical sections, since salinity is a good tracer of the vertical distribution of water masses in the Atlantic Ocean (as mentioned in section 4.1).

The Atlantic Ocean at LGM (Figure 6.1(a)) was much more stratified than today (e.g. Adkins et al., 2002; Zhang et al., 2014) with the dense (and salty) AABW occupying much of the deep basin, as discussed before. During the H1 (Figure 6.1(b)), the slow and continuous freshwater inflow into the North Atlantic reduces the GNAIW formation with a significant freshening of the upper 1000 m accompanied by a drop in the total ocean heat transport (e.g., Figure 5.2(a)). In Stanford et al. (2011), they

infer, from proxy data, a slowdown of northern sourced water formation from 19 to 17.5 ka. The H1 meltwater discharge is interrupted at 14.67 ka when the North Atlantic circulation recovers (Figure 6.1(c)). The deep ocean (below 500m) is fresher. The H1 changes in ocean circulation have been associated with atmospheric CO<sub>2</sub> changes (Menviel et al., 2014). It is suggested that an enhanced AABW could have been responsible for 30% of the atmospheric CO<sub>2</sub> increase. Between 14.35 and 13.85 ka (Figure 6.1(d)), the freshwater source in the Southern Ocean is activated (and re-activated in the Northern Hemisphere) in the model. A freshening of most of the upper 1000 m in both the North and South Atlantic can be observed. Even though this event is of much shorter duration in the model, its magnitude is about 4 times greater in the Southern Ocean (maximum of 60 m/kyr) than the meltwater flux in the North Atlantic at H1 (maximum of 15 m/kyr). The AABW is suppressed and only recovers at the YD (Figure 6.1(e)), when the North Atlantic receives a new iceberg discharge that slows down the AMOC. The opening of the Bering Strait at 12.9 ka in TraCE-21K contributes to a further weakening of the AMOC through meltwater transport from the Pacific to the Nordic seas (He, 2011). As soon as the freshwater flux from the North Atlantic is interrupted around 11.7 ka, the heat transport towards the north is re-established. The salinity barrier, which was responsible for the high stratification in the simulation initial condition, was continuously eroded and the dense water that was confined to the surface and intermediate layers (GNAIW) can finally sink and become NADW. During the Holocene (Figure 6.1(f)), the features of the modern NADW are in place and the model results compare well (albeit with very different spatial resolution) with observed data from the WOCE (Figure 4.3).

Examining the differences in the vertical salinity profile between H1 and LGM, BA and H1, MPW-1A and BA, YD and MWP-1A and Holocene and YD (Figure 6.2) helps in understanding the changes in the ocean structure between the different periods. The Atlantic basin is considerably fresher at H1 when compared to the LGM (Figure 6.2(a)). The largest differences are in the North Atlantic in the upper 1000 m with maximum values in the upper 200 m. The subtropical South Atlantic in the upper

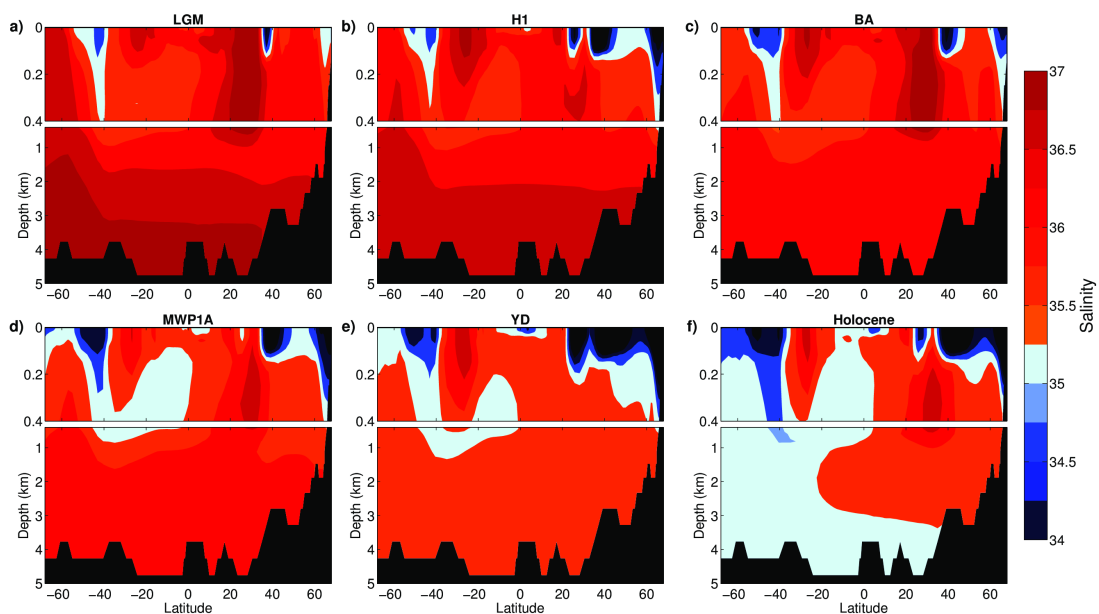


**Figure 6.1:** TraCE-21K salinity meridional sections across the Atlantic Ocean (25°W) at (a) LGM (22 ka–19 ka); (b) H1 (19 ka–14.67 ka); (c) BA (14.67 ka–14.35 ka); (d) MWP-1A (14.35 ka–13.85 ka); (e) YD (12.9 ka–11.3 ka); (f) Holocene (11.3 ka–0 ka). Figure from Marson et al. (2014).

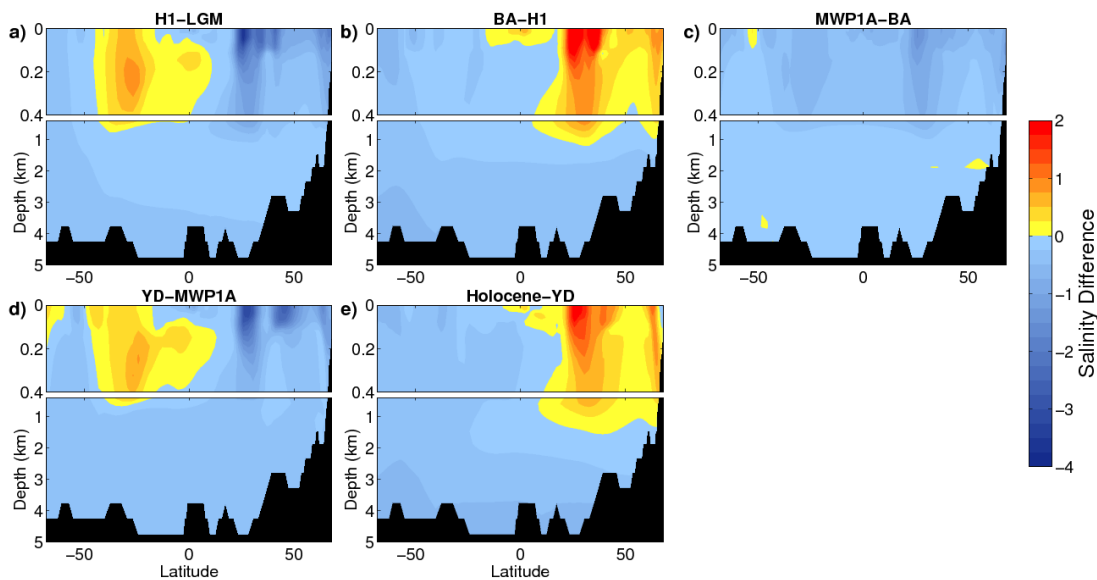


**Figure 6.2:** TraCE-21K salinity differences between (a) H1 (19 ka–14.67 ka) and LGM (22 ka–19 ka); (b) BA (14.67 ka–14.35 ka) and H1 (19 ka–14.67 ka); (c) MWP-1A (14.35 ka–13.85 ka) and BA (14.67 ka–14.35 ka); (d) YD (12.9 ka–11.3 ka) and MWP-1A (14.35 ka–13.85 ka); (e) Holocene (11.3 ka–0 ka) and YD (12.9 ka–11.3 ka). Figure from Marson et al. (2014).

800–900 m is saltier in H1 compared to LGM. This is because the prolonged freshening was entirely in the North Atlantic with the residual LGM saltiness remaining in the southern subtropics' upper ~800–900 m. Figure 6.2(b) shows the salinity differences between H1 and BA when the GNAIW recovers, which is seen by the positive salinity difference in most of the North Atlantic in the upper 1000 m, reaching the equator in the surface layers. The impact of MWP-1A with respect to BA is observed in Figure 6.2(c) with a basin-wide freshening. Comparing the salinity differences between the YD event with MWP-1A (Figure 6.2(d)) shows a similar distribution to Figure 6.2(a), except that the deeper ocean is significantly fresher. The upper 500 m displays a saltier South Atlantic and a fresh North Atlantic, indicating a weaker North Atlantic dense water formation. This structure finally evolves into the opposite structure, with the newly formed NADW that is able to spread into the Southern Hemisphere as seen today.

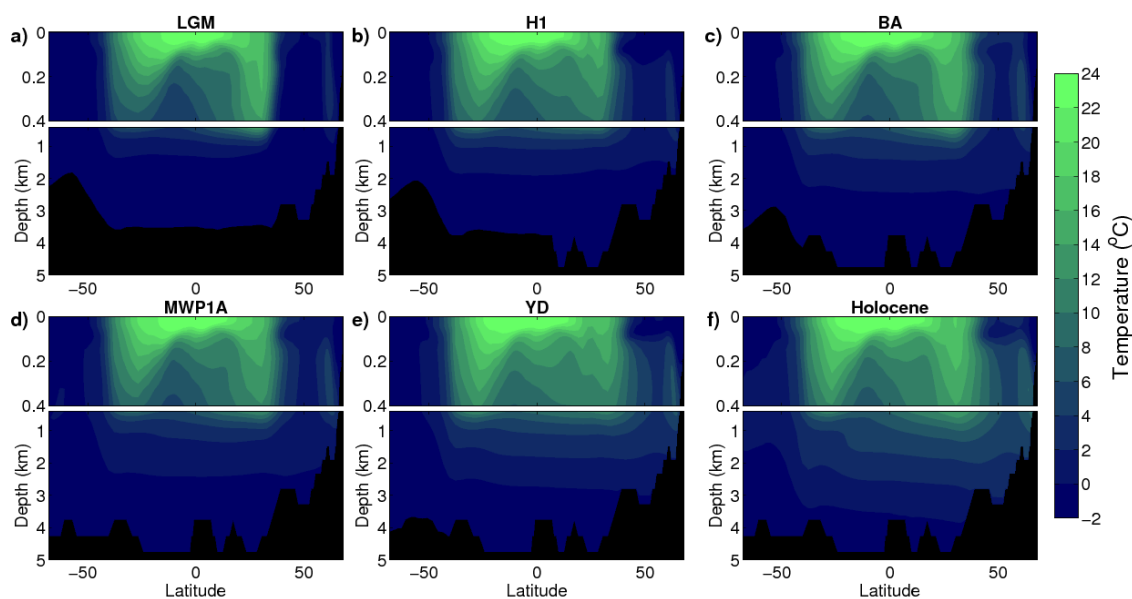


**Figure 6.3:** TraCE-21K temperature meridional sections across the Atlantic Ocean ( $25^{\circ}\text{W}$ ) at (a) LGM (22 ka–19 ka); (b) H1 (19 ka–14.67 ka); (c) BA (14.67 ka–14.35 ka); (d) MWP-1A (14.35 ka–13.85 ka); (e) YD (12.9 ka–11.3 ka); (f) Holocene (11.3 ka–0 ka)

The changes in temperature across the Atlantic are not so visible as the salinity changes when we look at Figure 6.3. What we can see is that the temperatures became higher — especially between 500 and 3000 m — as time evolved. When we observe the temperature differences between the main climatic periods (Figure

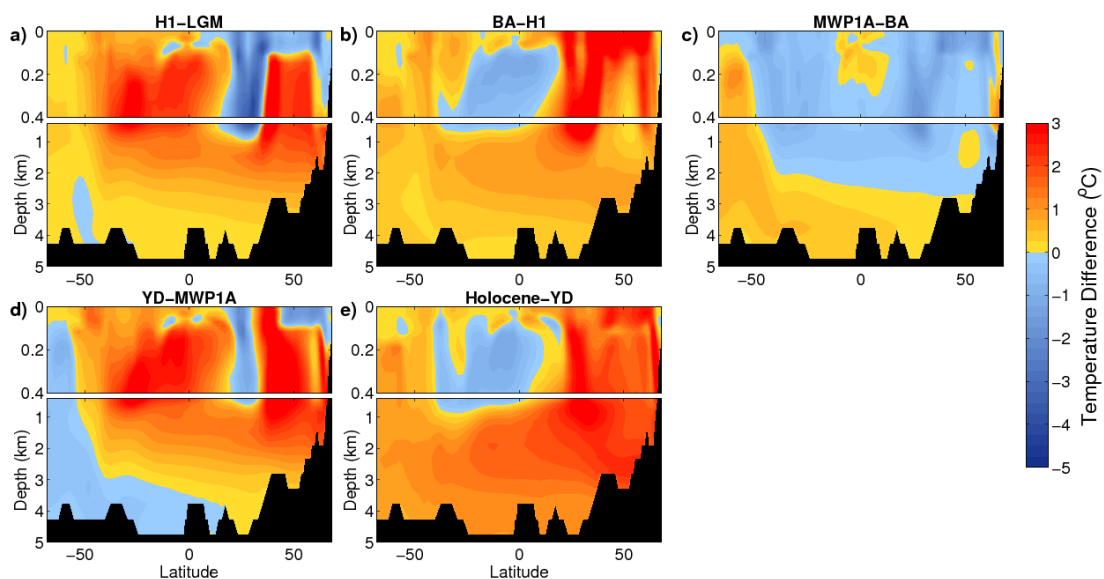


**Figure 6.4:** TraCE-21K temperature differences between (a) H1 (19 ka–14.67 ka) and LGM (22 ka–19 ka); (b) BA (14.67 ka–14.35 ka) and H1 (19 ka–14.67 ka); (c) MWP-1A (14.35 ka–13.85 ka) and BA (14.67 ka–14.35 ka); (d) YD (12.9 ka–11.3 ka) and MWP-1A (14.35 ka–13.85 ka); (e) Holocene (11.3 ka–0 ka) and YD (12.9 ka–11.3 ka).

6.4), however, the changes are clearer. During the H1 (Figure 6.4(a)), the first hundred meters cool down in the NH due to the discharge of cold meltwater. Below that, the temperature increase since the freshwater layer isolates the ocean from the atmosphere, trapping the heat in the ocean. The South Atlantic also warms up, reflecting the continuous warming in the SH during this period. From the H1 to the BA (Figure 6.4(b)), there is a general temperature rise trend, except for the tropics' first five hundred meters. The warming is more accentuated in the upper layers of NH, possibly in response to the abrupt BA warming observed in the North Atlantic. It is possible to distinguish this warmer water flowing southward around 1500 m, indicating GNAIW/NADW warming. The temperature response to the MWP-1A is quite different (Figure 6.4(c)). The large meltwater pulse in both hemispheres cause the intermediate layers to cool down. Additionally, the AABW's temperature rise because the heat that was supposed to scape to atmosphere in southern high latitudes is trapped by the stable freshwater layer around Antarctica. When this freshwater layer dissipates, the AABW cools down again and the intermediate layers' temperature increases (Figure 6.4(d)). Also, due to new meltwater discharges during the YD, some cooling is observed in the North Atlantic in Figure 6.4(d). The changes in temperature after YD

(Figure 6.4(e)) are very similar to the ones observed after the H1 (Figure 6.4(b)). This resemblance shows the ocean consistent response to D-O cycles since both H1 and YD were cold periods followed by rapid warming events. Nevertheless, the warming in NADW's tongue is stronger during the Holocene.

In order to see salinity and temperature changes together, these fields are plotted in a  $\theta - S$  diagram shown in Figure 6.5. The points are an average between  $30^{\circ}\text{S}$  and  $0^{\circ}$  from the LGM (blue points) to 0 ka (red points). The choice of this particular latitude range ( $30^{\circ}\text{S} - 0^{\circ}$ ) is based on the fact that the NADW only assumes an unified thermohaline characteristic in the South Atlantic, while in the North Atlantic this water mass is still divided in its precursors. It can be observed that there is a shift of the curve towards lower salinities throughout the entire water column, which is expected given all the freshwater entering the Atlantic Ocean in the last 21 000 yr. The changes in the shape of the  $\theta - S$  curve for the different periods are significant: the  $\theta - S$  curve at 21 ka has only two deep water types, while the modern curve (0 ka) presents the three main Atlantic Ocean deep water masses (AAIW, NADW and AABW, as in Figure 6.5(a)). The water type that specifies the NADW characteristics (salinity maximum at  $\sim 2500$  m) does not appear until the early Holocene. The  $\theta - S$  plots considering the same latitudinal interval for the South Atlantic, averaged for 21 ka, 15 ka, 14.1 ka, 13 ka and 0 ka, are shown in Figure 6.5(b). It is, again, clear that the deep salinity maximum characteristic of the NADW within the South Atlantic starts to develop only after 14.1 ka (Figure 6.5(b), pink curve).

The absence of the NADW during the glacial period is consistent with proxy records (Adkins et al., 2002). Also, the weaker dense water production in the NH during YD is discussed by several studies based on proxy data (Boyle and Keigwin, 1987; Hughen et al., 1998; Praetorius et al., 2008; Roberts et al., 2010). Through  $^{231}\text{Pa}/^{230}\text{Th}$  ratio analysis, Negre et al. (2010) – as well as the modeling study of Wainer et al. (2012) – argue that the modern Atlantic circulation was only fully established during the Holocene, which is also consistent with the evolution of the salinity-based water mass structure presented in Figure 6.1. The establishment of the NADW

as the main southward component of the AMOC induced the change in the overturning circulation geometry. The AMOC became deeper, meridional heat transport became more stable and the NADW became the main salt exporter across the Atlantic Ocean. Hence, the steep triangle cluster on Figure 5.3 (page 34) is explained: a smaller variability of the heat transport northwards and larger salt transport southwards in the Holocene.

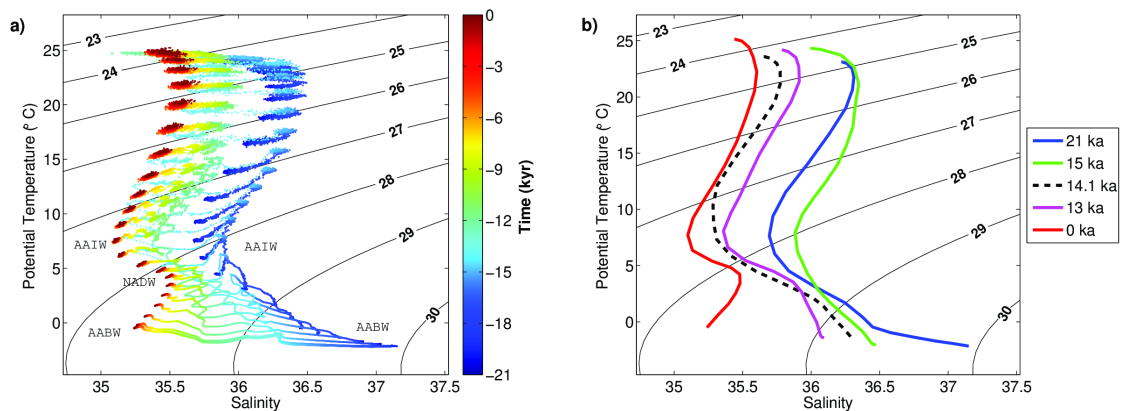


**Figure 6.5:** TraCE-21K  $\theta - S$  diagram averaged between  $30^{\circ}\text{S}$  to  $0^{\circ}$ , at  $25^{\circ}\text{W}$ . Time evolution is represented by the color range (a). The acronyms indicate the main water masses: AAIW – Antarctic Intermediate Water; AABW – Antarctic Bottom Water; NADW – North Atlantic Deep Water. The  $\theta - S$  diagram for the key climatic periods considered in this study: LGM (21 ka), before (15 ka), during (14.1 ka), after (13 ka) MWP-1A and 0 ka (b).  
Figure from Marson et al. (2014).

## CHAPTER 7

---

# The Atlantic Ocean's deglacial evolution: Water masses distribution

---

### 7.1 The mixing triangle technique

Mamayev (1975) explains how one can retrieve information about ocean water masses from a temperature-salinity analysis. The first step is to plot potential temperature (y-axis) against salinity (x-axis) - the  $\theta - S$  diagram. Let us start with a simplified example illustrated in Figure 7.1. Consider two water types A and B, with potential temperatures  $\theta_A$  and  $\theta_B$  and salinities  $S_A$  and  $S_B$ , respectively, represented by the blue circles in Figure 7.1. The dashed line between the two points represents the linear mixing between A and B, i.e., any parcel of water with thermohaline properties that falls within the line is the result of a mixing between A and B. The closer the water parcel is to A, the more A contributes to the formation of the water parcel - and similarly for water type B. As an example, the red cross in Figure 7.1 stands for a water parcel formed

by the mixing of 20% of A and 80% of B.

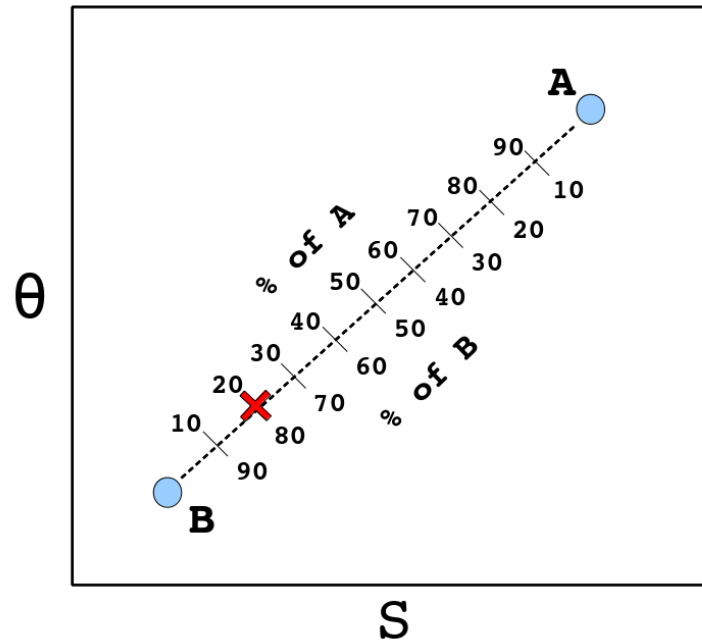


**Figure 7.1:** Mixing between two hypothetical water masses A and B.

Mathematically, we can find how much of each water type contributes to the properties of the water parcel through the equation set (7.1).

$$\begin{cases} \theta = m_A \theta_A + m_B \theta_B \\ S = m_A S_A + m_B S_B \\ 1 = m_A + m_B \end{cases} \quad (7.1)$$

where

$\theta$  = potential temperature of the water parcel

$S$  = salinity of the water parcel

$m_A$  = fraction of the water type A contributing to the mixing

$m_B$  = fraction of the water type B contributing to the mixing

$0 < (m_A, m_B) < 1$

Now, if we include one more water type (C, with potential temperature  $\theta_C$  and salinity  $S_C$ ) in our  $\theta - S$  diagram, we will have a mixing *triangle* instead of a mixing

line. In the illustrated example (Figure 7.2), the water parcel whose thermohaline properties are indicated by the red cross is formed by 10% of A, 60% of B, and 30% of C. In order to find each water type percentage, follow the lines parallel to triangle's side that opposes the desired vertex.

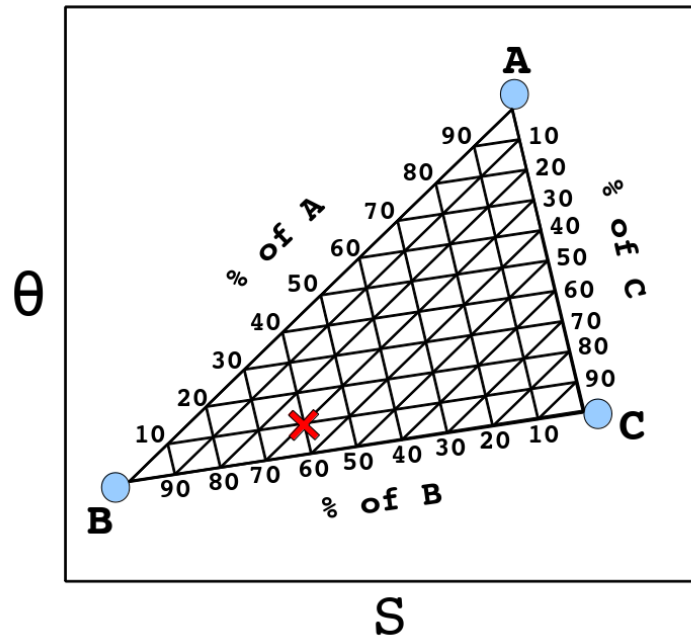


**Figure 7.2:** Mixing between three hypothetical water masses A, B, and C.

The equation system for three water types is:

$$\begin{cases} \theta = m_A \theta_A + m_B \theta_B + m_C \theta_C \\ S = m_A S_A + m_B S_B + m_C S_C \\ 1 = m_A + m_B + m_C \end{cases} \quad (7.2)$$

where

$\theta$  = potential temperature of the water parcel

$S$  = salinity of the water parcel

$m_A$  = fraction of the water type A contributing to the mixing

$m_B$  = fraction of the water type B contributing to the mixing

$m_C$  = fraction of the water type C contributing to the mixing

$0 < (m_A, m_B, m_C) < 1$

Therefore, with the known thermohaline values of each water type given by the literature, we can determine how much each of them is present at any point of the ocean (where the potential temperature  $\theta$  and salinity  $S$  are observed) by simply solving the system 7.2 and finding  $m_A$ ,  $m_B$ , and  $m_C$  (assuming that the mixing between them is linear).

## 7.2 Issues and their solutions within the mixing triangle technique

Now, consider the  $\theta - S$  diagrams prepared with TraCE-21K data (Figure 7.3). As we can see, many of the blue circles that represent water parcels do not fall within the triangle. In the classic mixing triangle technique described above, this would mean a negative contribution of some water type, which is physically impossible. This issue is addressed by doing modifications to the system of equations 7.2. The altered form of the system is:

$$\begin{cases} \theta = m_A\theta_A + m_B\theta_B + m_C\theta_C + \varepsilon_\theta \\ S = m_AS_A + m_BS_B + m_CS_C + \varepsilon_S \\ 1 = m_A + m_B + m_C + \varepsilon_{mass} \end{cases} \quad (7.3)$$

where

$\theta$  = potential temperature of the water parcel

$S$  = salinity of the water parcel

$m_A$  = fraction of the water type A contributing to the mixing

$m_B$  = fraction of the water type B contributing to the mixing

$m_C$  = fraction of the water type C contributing to the mixing

$\varepsilon_\theta, \varepsilon_S, \varepsilon_{mass}$  = residuals

$0 < (m_A, m_B, m_C) < 1$

The system is then solved in a nonnegative least-squares sense, i.e., the set of  $m_x$  ( $x=A,B,C$ ) is found by minimizing  $E$ , where

$$E = \varepsilon_{\theta}^2 + \varepsilon_S^2 + \varepsilon_{mass}^2 \quad (7.4)$$

with  $m_x \geq 0$ .

Additionally, in the "real" world a typical  $\theta - S$  diagram has more than three water types. Consider the TraCE-21K  $\theta - S$  diagrams for the Atlantic basin shown in Figure 7.3. The small circles represent the thermohaline properties of each point inside the Atlantic basin at a given time — the light blue ones are parcels located in the South Atlantic and the dark blue ones are parcels located in the North Atlantic. The red squares stand for the approximate thermohaline indexes of five different water types: Central Waters (CW), Antarctic Intermediate Water (AAIW), Glacial North Atlantic Intermediate Water (GNAIW), North Atlantic Deep Water (NADW) and Antarctic Bottom Water (AABW). Notice that only four of those appear at each time. With four water types it is not possible to construct a single mixing triangle. Thus, we solved this issue by constructing two triangles adjacent to each other, as indicated by the dashed green lines in Figure 7.3. If we determine in which triangle each point belongs, the mixing can be calculated normally.

Here, we have to assume that the water types CW and GNAIW (from 21 ka to 14 ka)/AABW (from 12 ka to 0 ka) do not mix because they do not occur in the same triangle. The assumption of no-mixing between CW and AABW is safe because they are separated by layers of intermediate and deep waters. On the other hand, the mixing between CW and GNAIW can happen in the North Atlantic because they are in contact. As we will see below, not considering the CW-GNAIW mix results in a false signal of AAIW and AABW dominance in the northern North Atlantic in the first 1500 m, where GNAIW should have larger contributions. We address this problem by presenting an alternative result for GNAIW distribution. This alternative result was generated using a mixing triangle for the North Atlantic only, which is reasonable since most of GNAIW does not cross the equator in TraCE-21K, as we could see

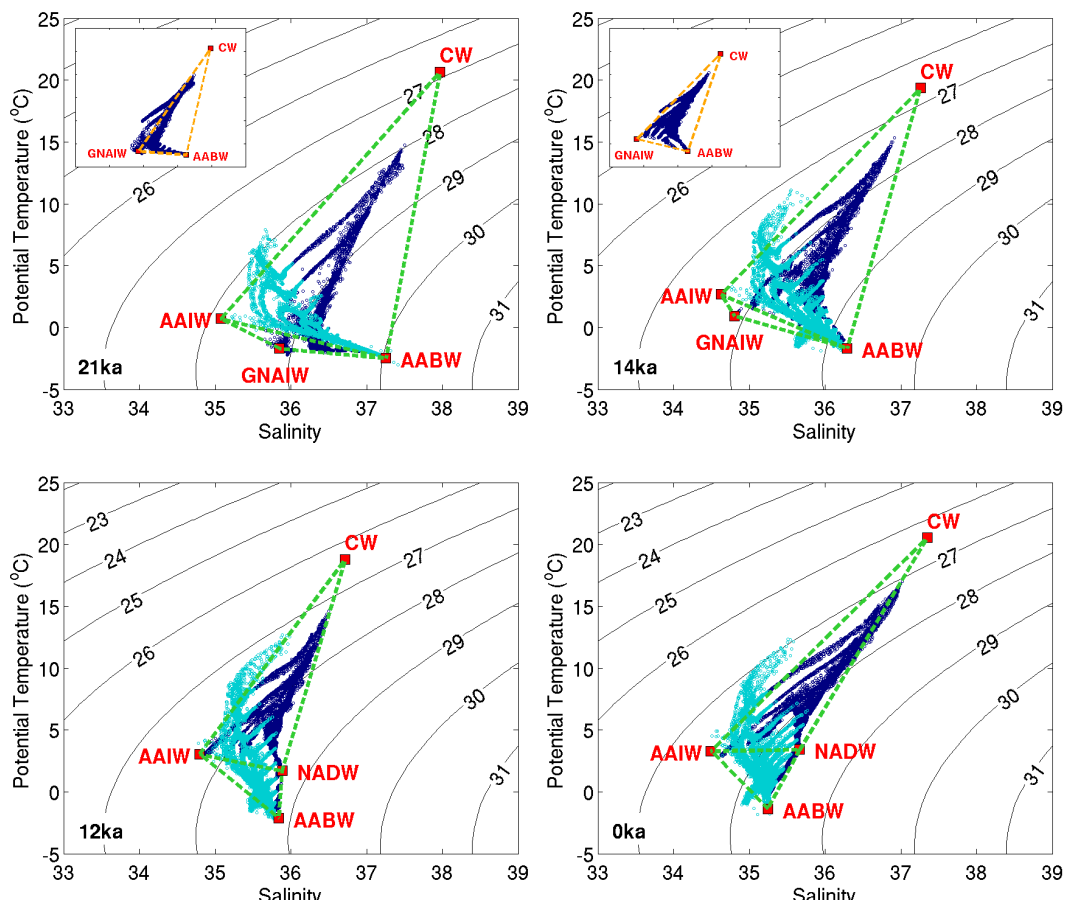


**Figure 7.3:**  $\theta - S$  diagram for points below 500 m depth for the entire Atlantic Ocean at 21 ka (top left), 14 ka (top right), 12 ka (bottom left) and 0 ka (bottom right). The light (dark) blue circles represent points in the South (North) Atlantic. The red squares mark the endmembers of the mixing triangle, i.e., the water types: Central Waters (CW), Antarctic Intermediate Water (AAIW), Antarctic Bottom Water (AABW), Glacial North Atlantic Intermediate Water (GNAIW), and North Atlantic Deep Water (NADW). The dashed green lines define the boundaries of the mixing triangles. The inserts in the upper left corners of the upper panels show the alternative configuration of the triangle to determine GNAIW's distribution.

in a previous analysis of the data (Marson et al., 2014). Thus, the triangle vertices are placed at CW, GNAIW, and AABW water types (see small plots in the upper panels of Figure 7.3). This way, we allow CW and GNAIW mixing but we cut the communication between the hemispheres. As one can see, the method of mixing triangles is simplistic and should be replaced by other methods, such as the Optimum MultiParameter analysis (OMP, Tomczak and Large, 1989) if a more complex analysis is required as well as more data (e.g., inorganic nutrients) is available.

Another issue we faced when working with paleoclimatic data is that the known present-day  $(\theta, S)$  pair of each water type does not apply at 21,000 years ago,

because the ocean was significantly different when compared to its modern state. Besides, one cannot fix the thermohaline properties for the whole deglacial run due to the large changes the ocean goes through during this interval. Therefore, the  $(\theta, S)$  pair of each water type was calculated every 1,000 years (plotted in Figures 7.4 to 7.7 below), taking into account its general features, formation region, and the approximate vertical distribution of the water masses observed in the Figure 6.1. We could thus determine:

- Central Waters (CW), by averaging five points with the **highest temperatures** between 20-40°N (North Atlantic Central Water, NACW) and 20-40°S (South Atlantic Central Water, SACW) between 250 and 500 m;
- Antarctic Intermediate Water (AAIW), by averaging five points with the **lowest salinities** between 40 and 50°S, 250 to 500 m depth;
- Antarctic Bottom Water (AABW), by averaging five points with the **lowest temperatures** between 60 and 70°S, 1500 to 5000 m depth; and
- North Atlantic Deep Water (NADW), by averaging the five points with the **highest salinities and low temperatures** (less than 3.5°C), when those salinities were greater than the AABW salinity. The region considered was between 40 and 80°N, 1500 to 5000 m depth.

Before averaging the five points which determine each water type, we removed points in the  $\theta-S$  diagram that were two standard deviations larger (or smaller) than the mean. Since in the mixing triangle analysis we could consider up to four water masses at the same time, we choose to eliminate SACW and approximate Central Waters in the entire Atlantic by NACW. The choice seems suitable since our interest is on denser water masses.

We saw in the previous chapter that the NADW signal does not appear in the simulation until 12 ka. As mentioned above, the literature indicates that in place of NADW there was Glacial North Atlantic Intermediate Water (GNAIW) at glacial periods. From Figure 7.3 (upper left panel), we observe an additional endmember within

the North Atlantic points. Tracing those points to the geographical region where they belong, we think this endmember indeed represents GNAIW. Therefore, we determined GNAIW thermohaline properties by averaging the 5 points with **lowest salinities which had corresponding lowest temperatures**, between 40 and 80°N, 400 to 1500 m depth. As we can see in the  $\theta - S$  diagrams (Figure 7.3), GNAIW water type is close to AAIW water type, and they become more similar as the deglaciation progresses.

In the next section, we will present the evolution of the water types' ( $\theta, S$ ) and the fractions  $m$  of the water types contribution to each point in the Atlantic. The fractions  $m$  are shown in vertical sections and horizontal maps. We chose four particular periods (21 ka, 14 ka, 12 ka, and 0 ka) to illustrate the range of ocean circulation changes seen in the last 21,000 years. In the maps, the white patches indicate either that there is no data in that region (due to bathymetry or coarse resolution of the coasts) or that the error  $E$  (given by equation 7.4) exceeded the value we considered reasonable. This value was calculated considering a residual of 0.001 for salinity ( $\varepsilon_S=0.001$ ) and mass ( $\varepsilon_m=0.001$ ), and a residual of 0.01 for temperature ( $\varepsilon_\theta=0.01$ ). For the presented results, the main area in which the points exceeded this threshold was the Mediterranean Sea.

## 7.3 Results

### 7.3.1 Evolution of the water types' properties

The evolution of the potential temperature of the North Atlantic and South Atlantic Central Waters (NACW and SACW, respectively) shows an out-of-phase relation from the LGM to 13 ka (Figure 7.4, upper panel). The NACW (dark blue line) cooled from 20 to 17 ka (H1 period), and then warmed until 15 ka, when it reached a peak at the onset of BA. A new cooling followed until 13 ka, after which the temperatures slowly rose to Holocene levels. In the South Atlantic, SACW's temperature began to warm at 20 ka (light blue line) and showed a short cooling from 16 to 15 ka. After that,

SACW restarted to warm. From 22 to 17 ka, SACW's salinity increased (Figure 7.4, lower panel, orange line) while NACW's salinity decreased in response to meltwater input from H1 (red line). SACW's salinity had a negative peak around 14 ka, before reaching Holocene levels at 8 ka. Its northern counterpart has two peaks between the LGM and present day — one in at the onset of the BA and the other is in the early Holocene. A major drop in NACW's salinity separate these two peaks at 13 ka.

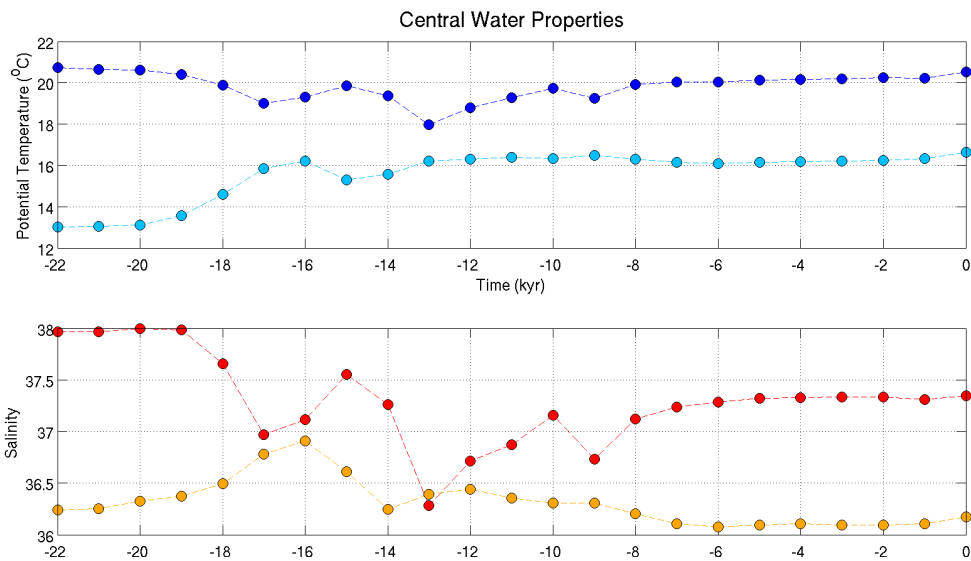


**Figure 7.4:** Potential temperature and salinity evolution of Central Waters. The orange and light blue lines represent SACW while the red and dark blue ones represent NACW.

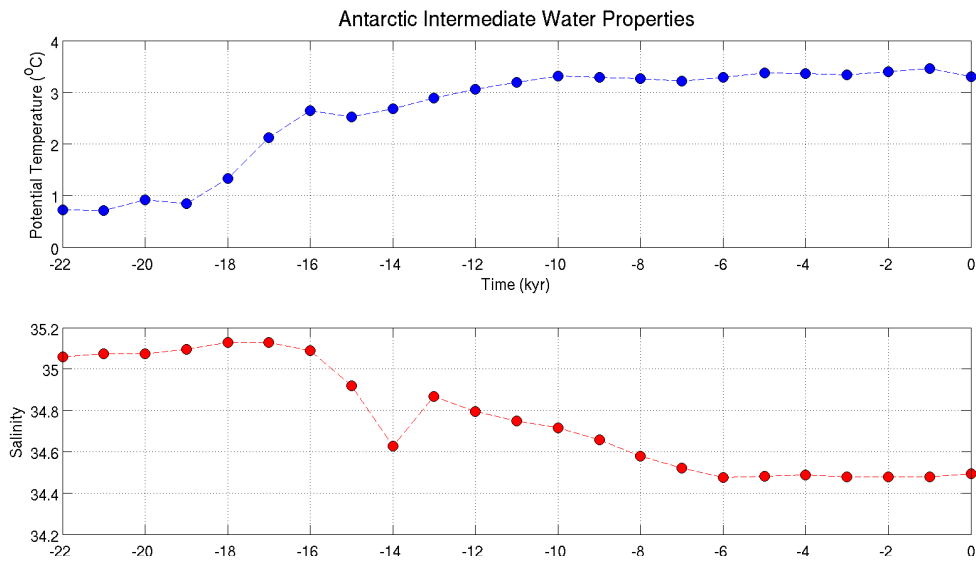


**Figure 7.5:** Potential temperature and salinity evolution of Antarctic Intermediate Water

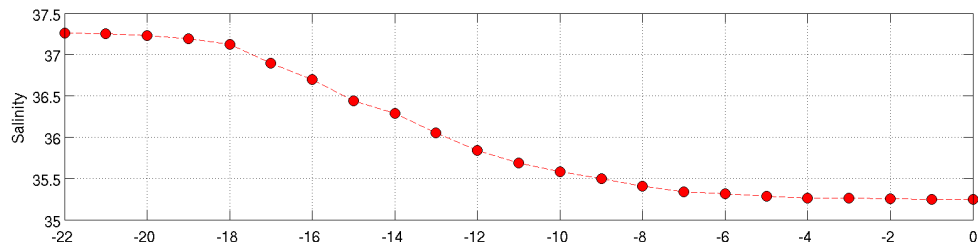
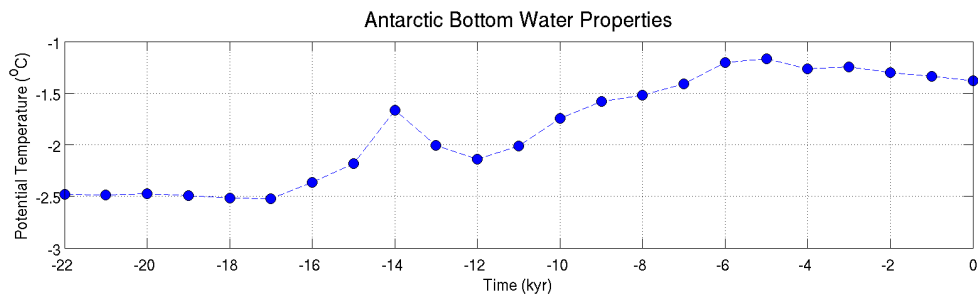
The AAIW's temperature evolved from  $\sim 0.8^{\circ}\text{C}$  at 22 ka to  $\sim 3.2^{\circ}\text{C}$  at present day (Figure 7.5, upper panel). The period with higher increase rates coincide with the

H1. The salinity trend is opposite to the temperature, decreasing from  $\sim 35.1$  to  $\sim 34.5$  throughout the simulation (Figure 7.5, lower panel). Embedded in this monotonic freshening, there is a negative peak at 14 ka, associated with MWP-1A.

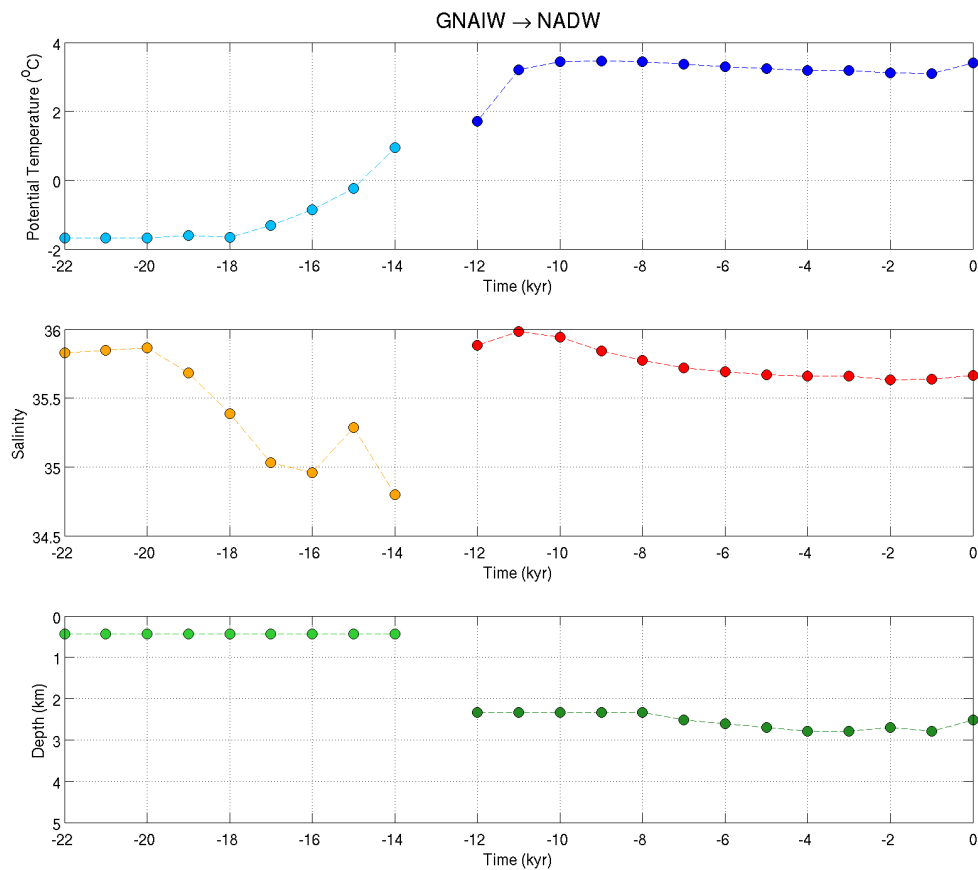
Although the changes in AABW's thermohaline properties are relatively smooth due the stable conditions in the abyssal ocean, the curves in Figure 7.6 show a large difference between the glacial AABW and the modern one. AABW's temperature starts at  $\sim -2.5^\circ\text{C}$  and ends up at  $\sim -1.4^\circ\text{C}$ . The warming is almost monotonic except for a peak coincident with the meltwater pulse 1A (MWP-1A), around 14 ka. The salinity decreases gradually from  $\sim 37.3$  to  $\sim 35.2$  during the simulation run. AABW's core remains near the bottom throughout the run.

Figure 7.7 shows the evolution of the properties of NADW and its precursor GNAIW. GNAIW's temperature at the beginning of the run was nearly as cold as modern AABW. The temperature increases from 19 to 14 ka, when it gives its place to NADW. NADW's temperature increased between 12 and 11 ka and then remains approximately constant (around  $3^\circ\text{C}$ ) until 0 ka. GNAIW's salinity at the LGM ( $\sim 35.9$ ) is similar to NADW's after 8 ka. After 20 ka, the GNAIW freshens about one unit until 14 ka, except for a slight peak at 15 ka. At 12 ka, NADW's salinity is very close to AABW's salinity, and this probably is the reason why it is difficult to tell them apart in a salinity vertical section before 11 ka (as we saw in the previous chapter). The core depths of both water types are quite distinct: around 500 m for GNAIW and 2500 m for NADW. The GNAIW/NADW points at 13 ka are absent in Figure 7.7 because the method could not find either water type. Even if there is some water mass being formed in the North Atlantic at this time, its properties possibly coincide with a linear combination of the other water types and, therefore, cannot be separated.

We can see on the  $\theta - S$  diagrams (Figure 7.3) that the thermohaline indexes (i.e., temperature and salinity) found for each water type represent well the mixing triangles endmembers. NADW's and AABW's salinities at the present time (0 ka), however, are overestimated by the model when compared to observations (Talley et al., 2011).



**Figure 7.6:** Potential temperature and salinity evolution of Antarctic Bottom Water



**Figure 7.7:** Potential temperature, salinity, and core depth evolution of Glacial North Atlantic Intermediate Water and North Atlantic Deep Water. The orange, light blue and light green lines represent GNAIW while the red, dark blue and dark green ones represent NADW.

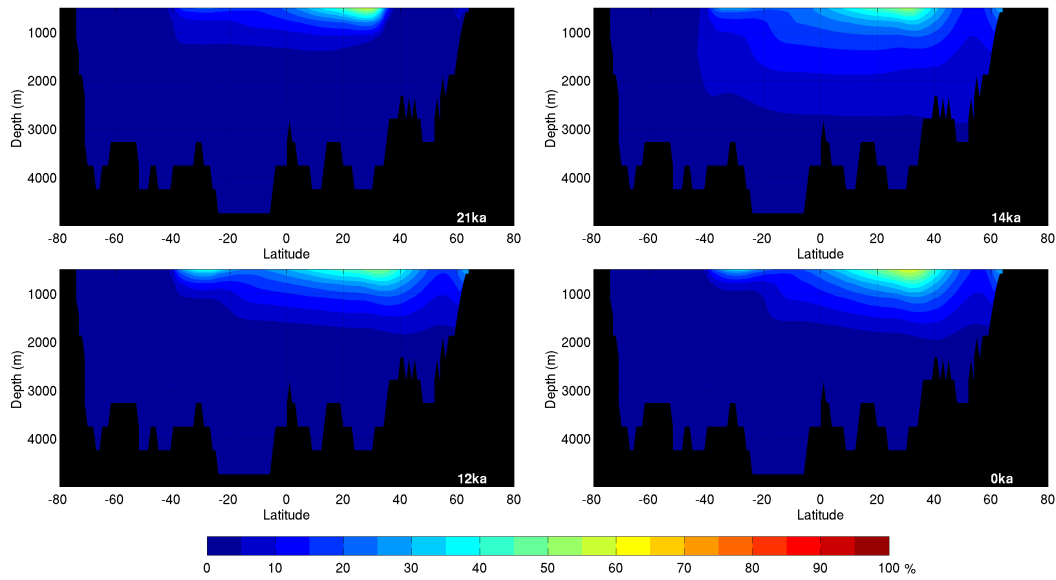
### 7.3.2 Spatial contribution of analyzed water masses in the Atlantic Ocean

Figure 7.8 shows the contribution of CW to the water column along the Atlantic (on 25°W) calculated through the mixing triangle method described above. During all the simulation, contributions of this water mass are restrict to less than 1000 m of depth. If we examine the horizontal structure of the CW distribution (Figure 7.9), we can see that the Central Waters concentrate in the middle of the subtropical gyres, especially the northern one - since we used NACW water type to represent Central Waters in general. The CW contribution is largest (~60%) at around 600 m and diminishes as we go down on the water column. The patterns of spatial distribution do not change much through the simulation.

The transect along 25°W for AAIW is presented in Figure 7.10. The highest contributions are seen around 40°S, although some signal appears around 40 to 60°N at 21 and 14 ka. The spatial patterns of AAIW distribution show a decreasing contribution north of 40°S. The band of higher percentages around ~40°S is weaker at H1 (Figure 7.12) and YD (Figure 7.11). The north latitude signal discussed before is present in the maps around the subpolar gyre and Nordic Seas. This is probably the undesired result of the GNAIW-CW no-mixing assumption mentioned before. AAIW percentages are reduced as we go deeper through the water column.

Antarctic Bottom Water contributions are high through most of the Atlantic Ocean from 21 to 14 ka (Figure 7.13, upper panels). The contributions diminish toward the surface, except for the southern band from 80°S to 60°S. At 21 ka the percentages are smaller from 40°N to 60°N too, forming a "blob" of lower contributions (as indicated by the arrow in Figure 7.13, upper left panel). A big change is seen from 14 to 12 ka, when AABW contributions drop to nearly zero northward of 40°S and above 3000 m. From this point on, the AABW distribution pattern remains generally the same.

In the spatial maps (Figure 7.14, see below), higher percentages of AABW dominate the latitudes south of ~50°S at ~600 m, and the values increase toward the



**Figure 7.8:** Central Waters contribution (%) — calculated using NACW water type — below 500 m, along 25°W, at 21 ka (upper left), 14 ka (upper right), 12 ka (lower left), and 0 ka (lower right).

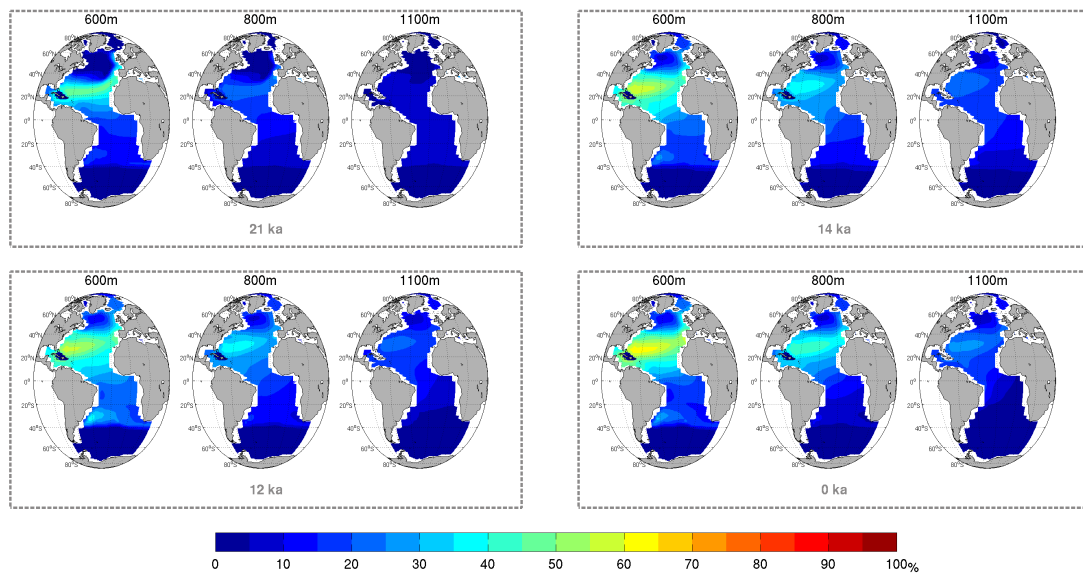


**Figure 7.9:** Central Waters contribution (%) — calculated using NACW water type — at various layers at 21 ka (upper left), 14 ka (upper right), 12 ka (lower left), and 0 ka (lower right).

bottom. From Figure 7.14 (upper panels) there is a rise of percentages around and at the center of the subpolar gyre in the North Atlantic in the upper 1500 m, which is probably caused by the no-mixing assumption between CW and GNAIW that we mentioned in section 7.2. After 13 ka (Figure 7.14, lower panels), higher contributions are present near the bottom throughout the Atlantic and almost nothing is found north

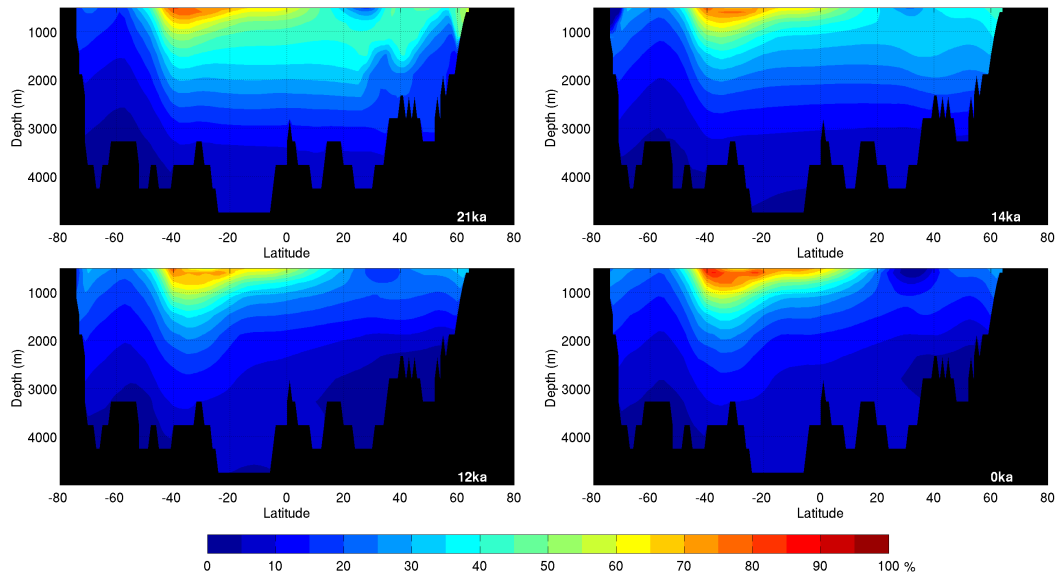


**Figure 7.10:** Antarctic Intermediate Water contribution (%) below 500 m, along 25°W, at 21 ka (upper left), 14 ka (upper right), 12 ka (lower left), and 0 ka (lower right).

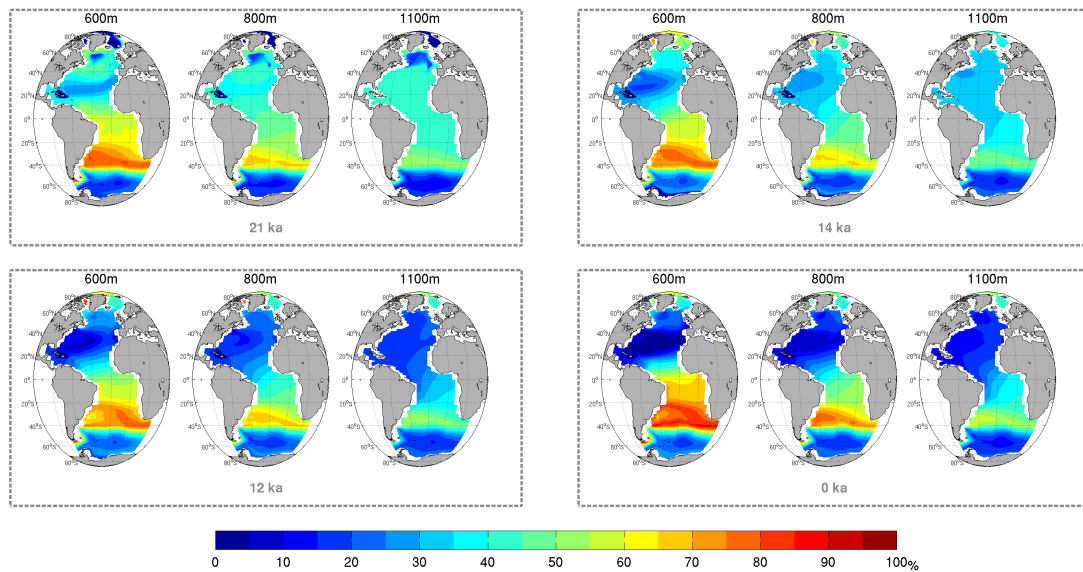


**Figure 7.11:** Antarctic Intermediate Water contribution (%) at various layers at 21 ka (upper left), 14 ka (upper right), 12 ka (lower left), and 0 ka (lower right).

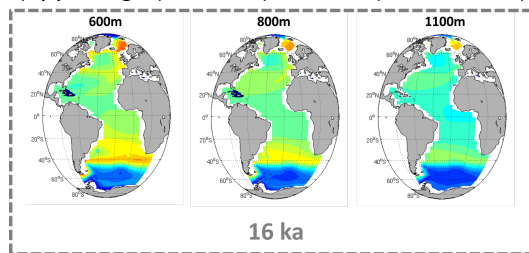


**Figure 7.12:** Antarctic Intermediate Water contribution (%) at various layers at 16 ka.

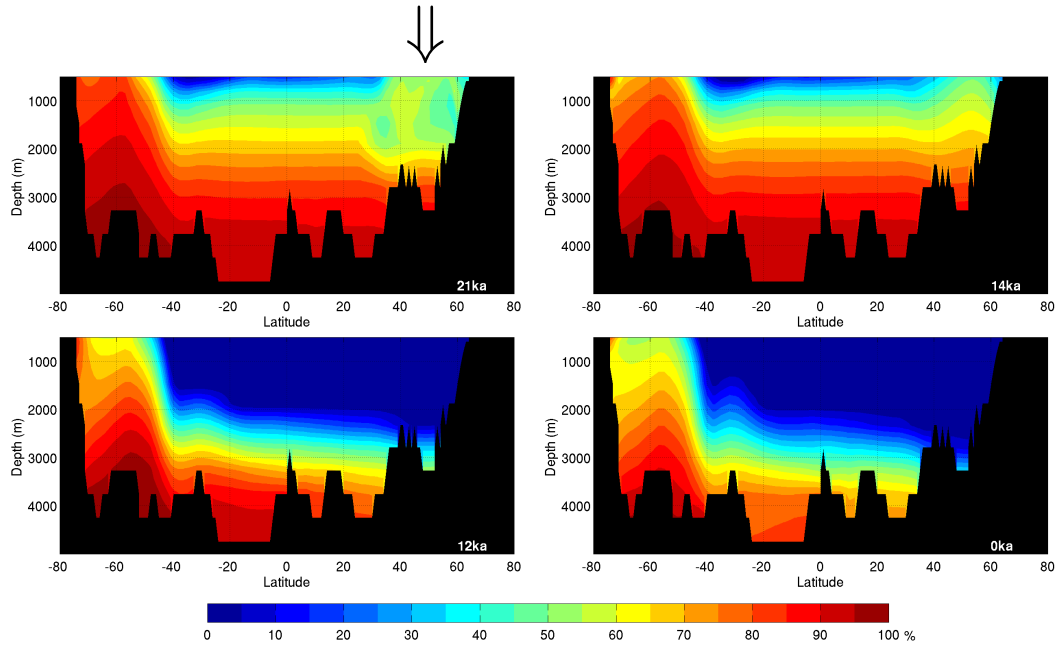


**Figure 7.13:** Antarctic Bottom Water contribution (%) below 500 m, along 25°W, at 21 ka (upper left), 14 ka (upper right), 12 ka (lower left), and 0 ka (lower right). The arrow indicates the "blob" of AABW low contributions cited in the text.

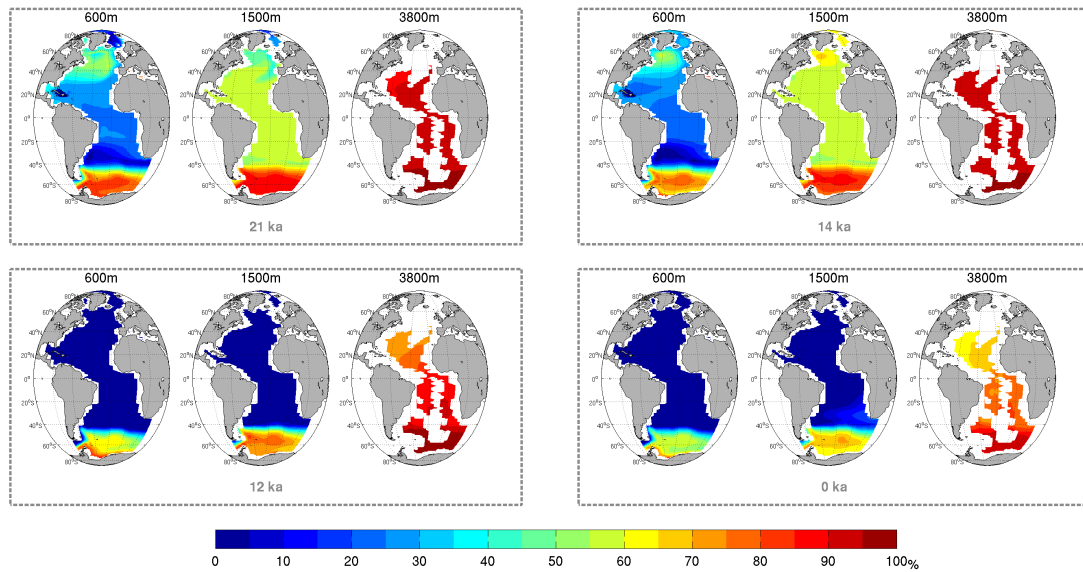


**Figure 7.14:** Antarctic Bottom Water contribution (%) at various layers at 21 ka (upper left), 14 ka (upper right), 12 ka (lower left), and 0 ka (lower right).

of 50°S at deep and intermediate depths.

Within the original triangle configurations, the highest contributions of GNAIW at 21 ka are located in the upper 2000 m of the North Atlantic (~40°N, Figure 7.15, upper left panel). When we consider the mixing between CW and GNAIW in the alternative triangle (small plots in Figure 7.3), the GNAIW distribution is larger (see

below Figure 7.17, left panels) and occupies the intermediate levels as south as 20°N. Because GNAIW's  $(\theta, S)$  are similar to AAIW's  $(\theta, S)$ , the high percentages between the equator and 20°N are possibly related to AAIW's spreading beyond the equator at the LGM. From 12 ka to the present day, the vertical distribution of NADW does not change much and its core dominates depths around 2000 to 3000 m from high northern latitudes to ~40°S (Figure 7.15, lower panels).

The horizontal distribution of GNAIW shows the highest percentages in the Nordic Seas and lower ones in the subpolar gyre (Figure 7.16, upper left panel and Figure 7.17, upper right maps). The GNAIW contributions at 14 ka disappear in Figure 7.16 (upper right panel), and are not significant south of 60°N in Figure 7.17. The NADW shows a very different horizontal distribution, with high concentrations south of Greenland at ~600 m and throughout the deep ocean down to the Southwestern Atlantic (Figure 7.16, lower left panel). A quasi-latitudinal band of higher contributions appears around 40°S at ~600 m. The spatial patterns do not vary significantly from 12 ka to 0ka (Figure 7.16, lower panels), except by a slight decrease in NADW's contribution at the 1500 m layer of the subtropics. This decrease is probably related to the deepening of NADW's core after 8 ka, also observed in Figure 7.7 (bottom).

## 7.4 Discussion

From the time series of the CW temperature (Figure 7.4, upper panel), we observe that these waters seem to capture the surface temperature signal of each hemisphere (Figure 7.18, top). The out-of-phase pattern between north and south has been known in the literature as the "bipolar seesaw" (Broecker, 1998). The North Atlantic cooled during H1 and YD, while the southern counterpart cooled during BA. CW salinities also connect with the surface, reflecting the net balance between precipitation and evaporation (Figure 7.18, middle) and the meltwater fluxes (Figure 7.18, bottom).

A higher contribution of CW for the subtropical gyres' center (maps in Figure

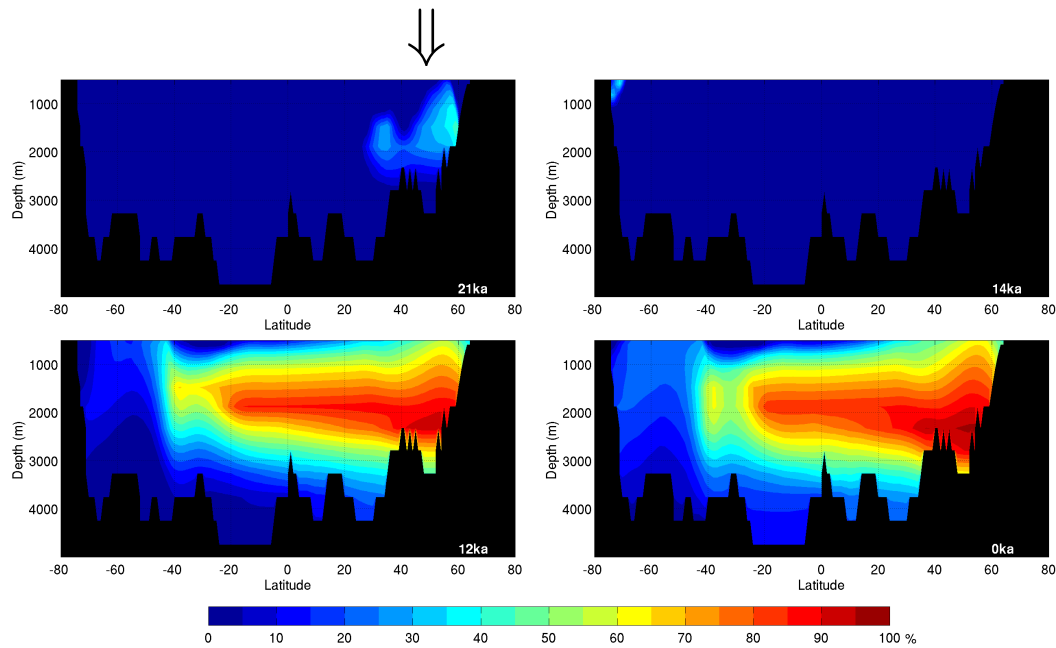


**Figure 7.15:** Glacial North Atlantic Intermediate Water at 21 ka (upper left) and 14 ka (upper right) and North Atlantic Deep Water at 12 ka (lower left) and 0 ka (lower right) contribution (%) below 500 m, along  $25^{\circ}\text{W}$ . The arrow indicates the "blob" of GNAIW high contributions cited in the text.

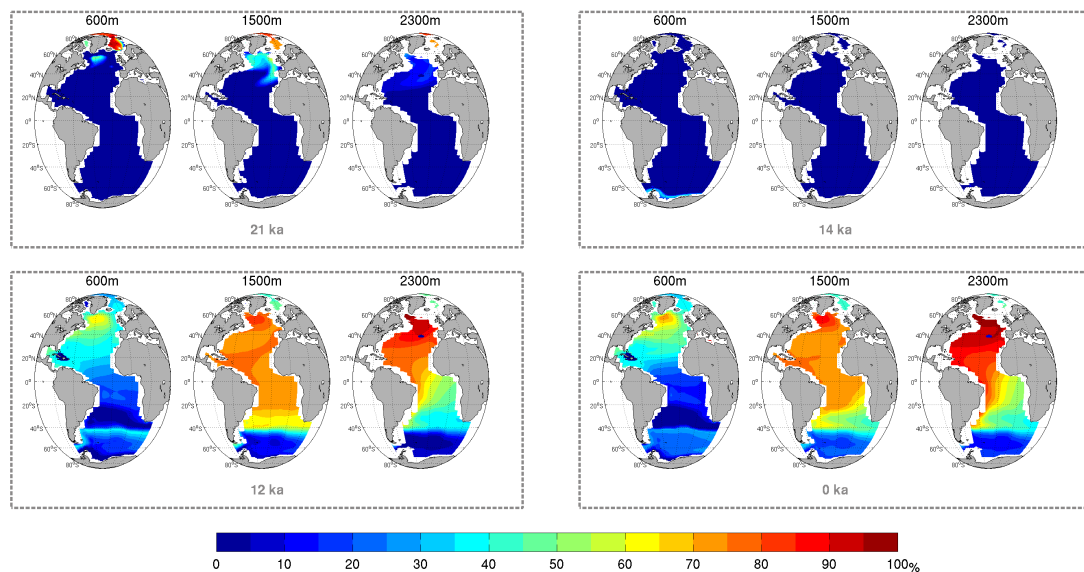


**Figure 7.16:** Glacial North Atlantic Intermediate Water at 21 ka (upper left) and 14 ka (upper right) and North Atlantic Deep Water at 12 ka (lower left) and 0 ka (lower right) contribution (%) at various layers.

7.9) agrees with the fact that the Central Waters are formed in those regions and occupy most of their pycnoclines (Talley et al., 2011).

The AAIW's temperature evolves quite monotonically (Figure 7.5, upper panel).

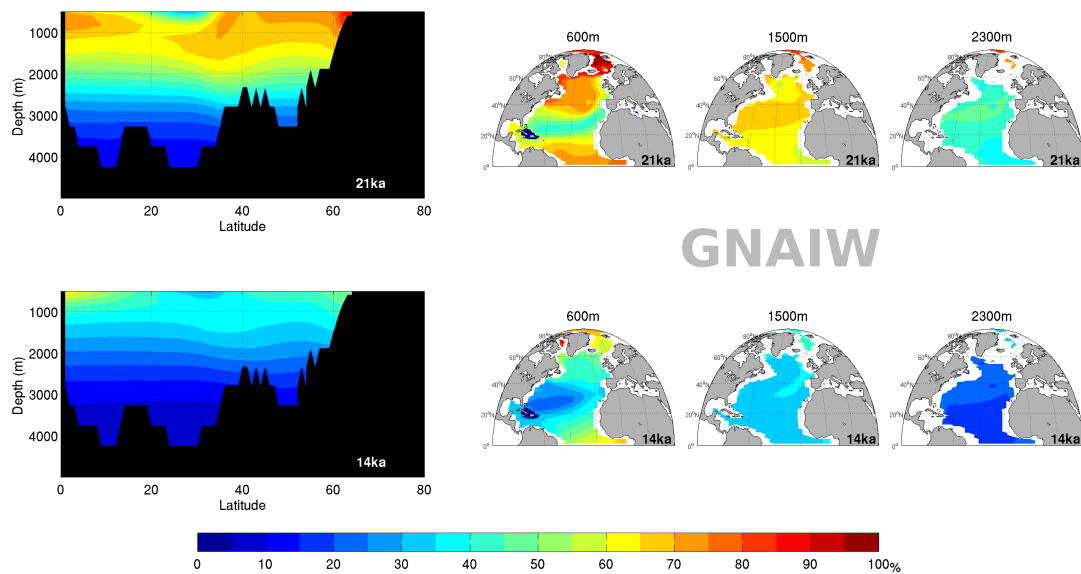


**Figure 7.17:** Glacial North Atlantic Intermediate Water contribution (%) from the alternative triangle. The left panels show the vertical distribution below 500 m, along  $25^{\circ}\text{W}$ , while the right panels show the horizontal distribution in the North Atlantic.

From 22 to 16ka, the temperature increase in AAIW could be aligned with the early warming in the Southern Hemisphere (e.g., Barker et al., 2009). The salinities, in turn, accompany the overall freshening trend in the Atlantic Ocean, with a sudden drop associated with MWP-1A.

The AAIW also seems to be well represented in its spatial distribution (Figure 7.11). The band of high contribution values coincides with the typical position of the Subantarctic Front, which is the region that surface waters are subducted and transported northward in intermediate layers (Deacon, 1937). Although this is the hypothesis of AAIW formation that we consider here, there are other studies that point to either the southeast Pacific (McCartney, 1977) or Brazil-Malvinas confluence in the southwest Atlantic (Piola and Gordon, 1989). In some cases, the low salinity water formed in the circumpolar region is called Subantarctic Mode Water (SAMW). From this band located around  $40^{\circ}\text{S}$ , AAIW spreads northward and gradually mixes with other water masses. The attributed contribution of AAIW to the northern subpolar gyre is related to the similarities between its low salinity and fresh GNAIW. This indicates that the mixing triangle method cannot distinguish perfectly both water masses in the

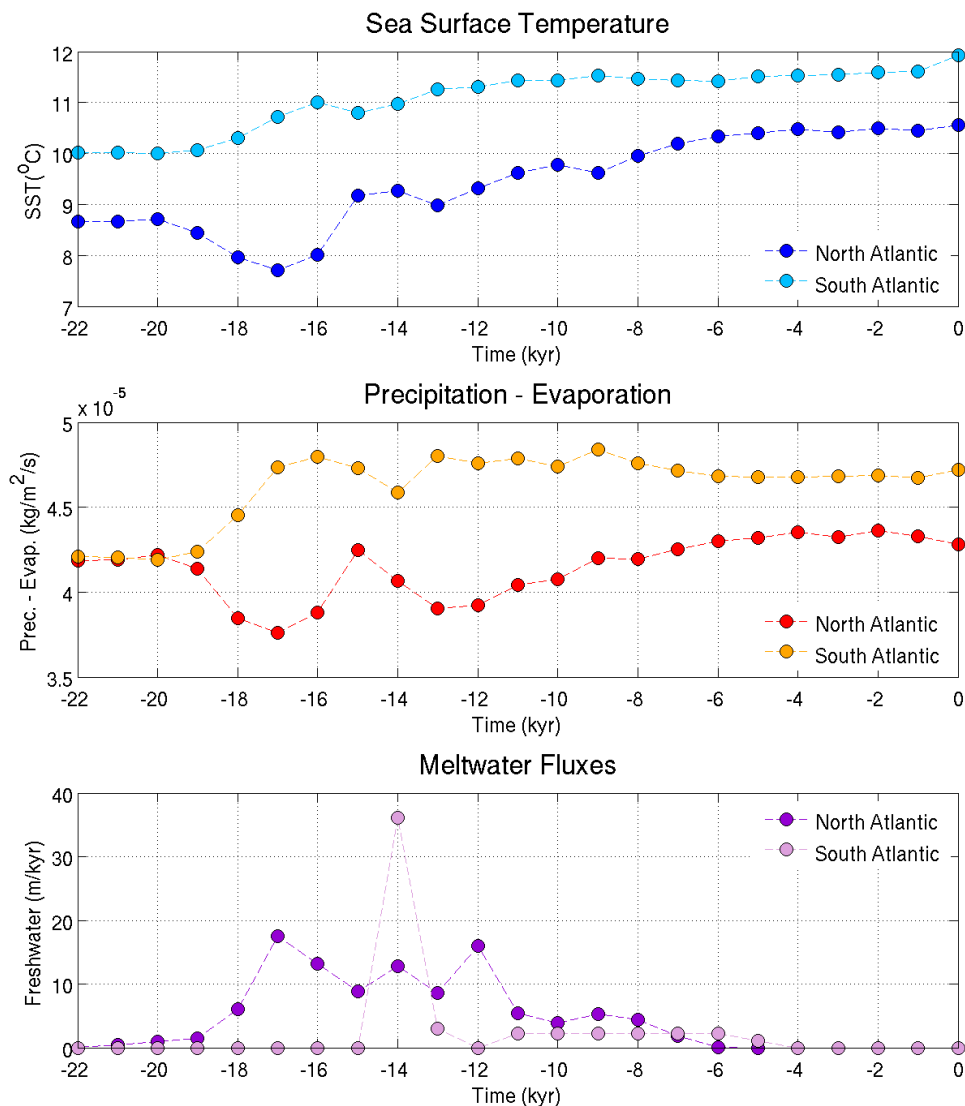


**Figure 7.18:** Mean sea surface temperature (top), precipitation minus evaporation (middle), and meltwater fluxes (bottom) for the North (dark blue, red, purple) and South (light blue, orange, violet) Atlantic Ocean from TraCE-21K simulation.

Northern Hemisphere.

The lower contributions of AAIW during the H1 (Figure 7.12) and YD (Figure 7.11) raises the question about the northward expansion of AAIW during the last deglaciation. The subject is still controversial. There are some studies which suggest there was an increase in the northward penetration of AAIW during the cold events (e.g., Pahnke et al., 2008; Thornalley et al., 2011), resulting in its presence up to  $60^\circ\text{N}$ . However, other investigators believe the opposite: AAIW would have been ac-

tually weaker during those periods (Came et al., 2008; Xie et al., 2012). Our results, therefore, seem to agree with the second hypothesis.

During the last deglaciation, the freshwater resulting from the melting of ice sheets — both from the Northern and Southern Hemispheres — led to a gradual decrease of the Antarctic Bottom Water's salinity (as we saw in chapter 6; Figure 7.6, lower panel). The small increase of AABW's temperature accompanied the general climate warming trend, and is similar to its freshening — fairly gradual —, except for the small peak at 14 ka (Figure 7.6, upper panel). This peak results from the presence of freshwater at the surface during the MWP-1A, which increases the vertical stability of the water column and, consequently, does not allow the heat brought at depth from the north to escape. The same behavior was observed by Richardson et al. (2005) in their model study about responses to a freshwater input in the Southern Ocean.

Using the methodology presented, we could identify GNAIW water type characteristics up to 14 ka (Figure 7.7). We found that GNAIW was a cold and relatively fresh water mass (when compared to glacial AABW), as suggested by Boyle and Keigwin (1987). These characteristics make GNAIW very similar to AAIW in the  $(\theta, S)$  domain, especially as the deglaciation advances in time. Interestingly, after 13 ka, the fresh "tail" that stands for GNAIW in the North Atlantic  $\theta - S$  diagram assumes a position similar to the one that Labrador Sea Water occupies in a modern  $\theta - S$  diagram.

The LGM GNAIW's salinity (Figure 7.7, orange line in the middle panel) is similar to modern NADW (Figure 7.7, red line in the middle panel) and was progressively reduced during the H1. It seems that after 16 ka the GNAIW's salinity trend was heading toward NADW's salinity values, but it was interrupted by a freshening at 14 ka. Because the ocean waters that mix with the meltwater released during MWP-1A share GNAIW's characteristics, it is hard to distinguish them around 14 ka. This would explain the reduction of GNAIW salinity at 14 ka (Figure 7.7, orange line) and also the presence of a small amount of a GNAIW-like water mass in the Southern Ocean (Figure 7.15 and 7.16, upper right panel). The temperatures increase gradually from 18 ka

to 10 ka, separating the cold GNAIW at the beginning of the last deglaciation from the warm and stable NADW during the Holocene (Figure 7.7). The location of GNAIW's and NADW's core in the water column is clearly distinct (Figure 7.7, bottom), which led us to support the use of different names for these water masses.

The vertical sections of AABW's distribution across the Atlantic (Figure 7.13) show the dominance of this water mass at the bottom and deep layers of the entire basin from 21 to 14 ka. Indeed, as discussed above, it is well established that a salty version of AABW expanded meridionally and vertically at the beginning of the deglaciation (e.g., Duplessy et al., 1984; Oppo and Fairbanks, 1987; Curry et al., 1988; Duplessy et al., 1988; Adkins et al., 2002; Cottet-Puinel et al., 2004; Ferrari et al., 2014). From 12 ka on, however, AABW was drastically reduced and confined to abyssal depths, dominating the entire water column only nearer its formation region in the Southern Ocean (Figure 7.13, lower panels).

We believe that the transition between GNAIW and NADW occurred gradually after Heinrich Stadial 1 (after 14.7 ka). Tessin and Lund (2013) analyzed  $\delta^{13}\text{C}$  reconstructions from Brazil margin cores and suggested a reorganization of water masses during the H1, with reduced influence of the northern sourced water mass. The freshwater input between 19 and 15 ka might have weakened the intermediate water formation in the North Atlantic, which is why the AMOC is sluggish during this period (as mentioned in section 5.1). This meltwater was then transported to the Southern Ocean, where it continuously freshened AABW and finally allowed NADW to sink from 12 ka and beyond (chapter 6 and Figure 7.15, lower panels). This is the point when AABW retracts to give space to the newly formed NADW.

The AABW's horizontal distribution (Figure 7.14) shows the formation of this water mass to be south of  $50^\circ\text{S}$ . The spreading of this water mass happens mostly near the bottom. At 21 ka and 14 ka (Figure 7.14, upper panels), the AABW's contribution is considerable also in the deep layers. The higher values at the northern subpolar gyre are due to the configuration of the triangles explained above. At 12 ka (Figure 7.14, lower left panel) we note the sudden reduction of AABW in the At-

lantic Ocean. AABW spreads at the greatest depths and is probably traceable up to the subtropical North Atlantic, which is consistent with the pattern observed today (Purkey and Johnson, 2010; Talley et al., 2011).

When we compare the maps showing the GNAIW and NADW horizontal distributions (Figure 7.16 and 7.17), we notice that the spreading of NADW is much larger. NADW is transported by the DWBC and reaches 40°S, where it upwells (see the horizontal strip of higher values at ~600 m in the lower two panels of Figure 7.16). GNAIW, on the other hand, is mostly constrained to the subpolar gyre. The maps also reveal something else of interest. It appears that GNAIW was formed mainly by the Nordic Seas overflow, and then spreads to the subpolar North Atlantic (Figure 7.16, upper left panel). NADW, in turn, is a result of the mixing between Nordic Seas overflow and Labrador Sea waters (LSW). Proxy data reconstructions indeed suggested that LSW formation was absent until the early Holocene and that the main source of dense waters in the North Atlantic was the Nordic Seas (Hillaire-Marcel et al., 2001; Cottet-Puinel et al., 2004; Crocket et al., 2011). The reason for LSW's early absence is likely because of the almost constant meltwater flux from the Laurentide ice sheet into the Labrador Sea (Cottet-Puinel et al., 2004).

## CHAPTER 8

---

# The Southern Ocean and the Meltwater

## Pulse 1A

---

**T**HE Southern Ocean is the only ocean that covers every longitude, allowing a continuous and strong eastward flow — the Antarctic Circumpolar Current (ACC). Because it connects all the major ocean basins, ACC is the main vehicle that transports water from one ocean to another. Near the Antarctic coast, another current flows opposite to ACC: the Antarctic Coastal Current (ACoC). ACoC is important because it sets the regime where the ocean interacts with ice shelves, which ultimately modify water masses formed on the Antarctic shelf. Due to low temperatures and constant sea ice formation — which releases salt to the water underneath —, the shelf waters get very dense and sink to the bottom, especially at the Weddell and Ross Seas. These very dense waters are later exported to all ocean basins as Antarctic Bottom Water (AABW), which drives the lower limb of the global Overturning Circulation.

## 8.1 Regional evolution of thermohaline properties: Weddell and Ross Seas

The AABW precursors are mainly formed in the Weddell Sea and Ross Sea (Orsi et al., 2002). Because of that, we have placed a meridional section in each sea in order to observe the changes in temperature and salinity during the 22 thousand years of simulation (Figure 8.1).

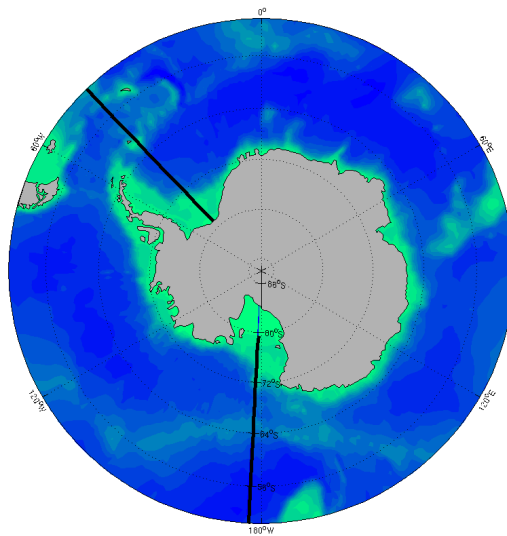


**Figure 8.1:** Chosen transects at the Weddell Sea and Ross Sea (black lines). The position of these transects were determined based on the approximated longitude of the two main point of dense water formation (Orsi et al., 2002).

The temperature sections for both seas (Figures 8.2 and 8.3) show a progressive warming of intermediate and deep waters, especially during the Holocene. The range of depths that shows the largest warming is commonly occupied by the Circumpolar Deep Water (CDW) — or Warm Deep Water (WDW) in the Weddell Sea. As this water mass is essentially formed by deep waters coming from north (North Atlantic Deep Water, Pacific Deep Water, and Indian Deep Water; Talley et al., 2011), the warming of CDW may indicate warming of its predecessors. We know, from the previous chapters, that at least the NADW warmed during the last 21 kyr. In the salinity sections (Figures 8.4 and 8.5), the values diminish in the entire water column as we move from the LGM to 0 ka — which is expected in high latitudes under deglacial con-

ditions. The largest salinity change occurred between 19 ka and 14.7 ka, when the meltwater prescribed for H1 reached the Southern Ocean and ultimately freshened the Antarctic Bottom Water.

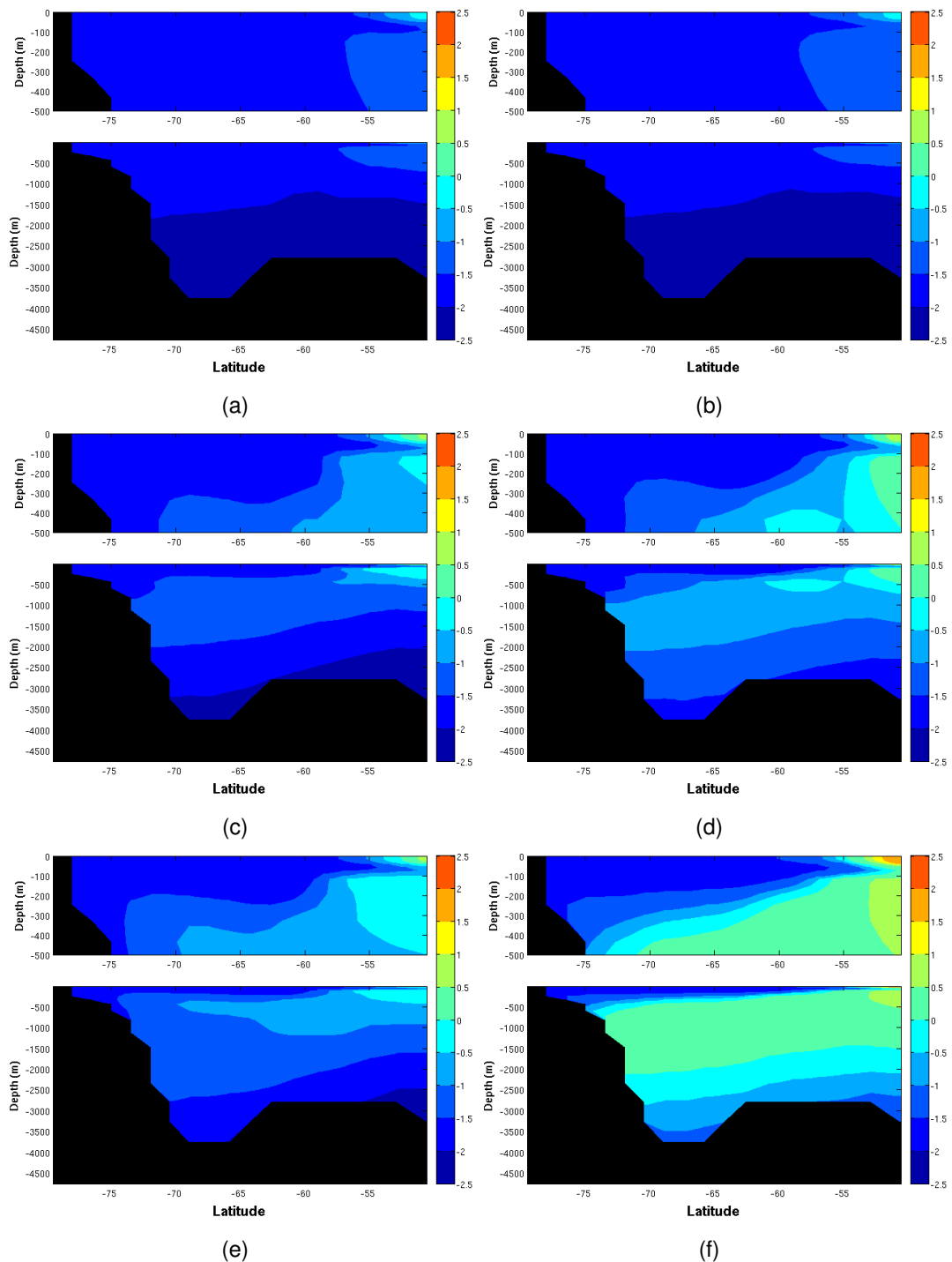


**Figure 8.2:** Temperature at the Weddell Sea transect at (a) 22 ka, (b) 19 ka, (c) 14.7 ka, (d) 12.9 ka, (e) 11.7 ka, and (f) 0 ka.

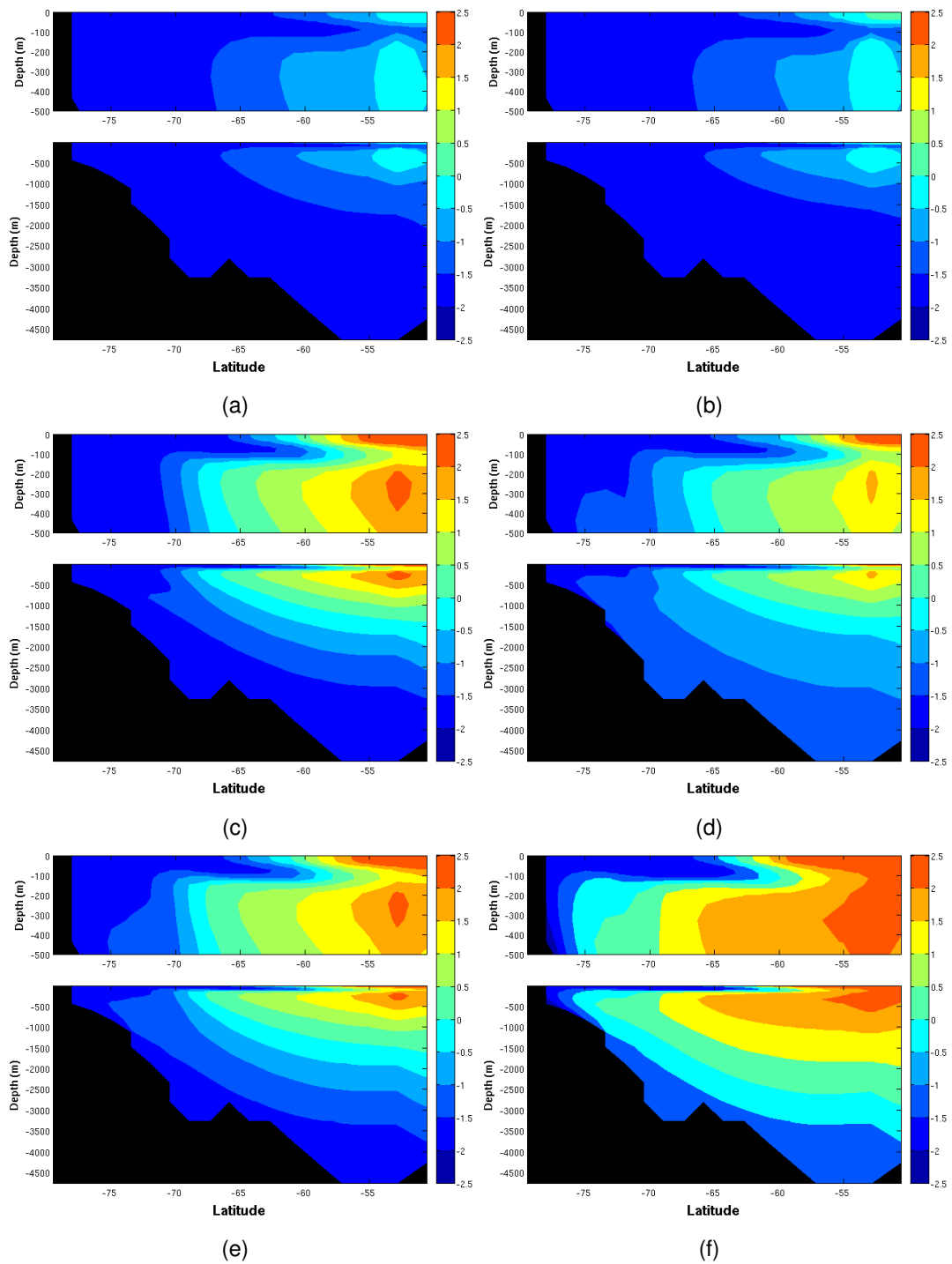


**Figure 8.3:** Temperature at the Ross Sea transect at (a) 22 ka, (b) 19 ka, (c) 14.7 ka, (d) 12.9 ka, (e) 11.7 ka, and (f) 0 ka.

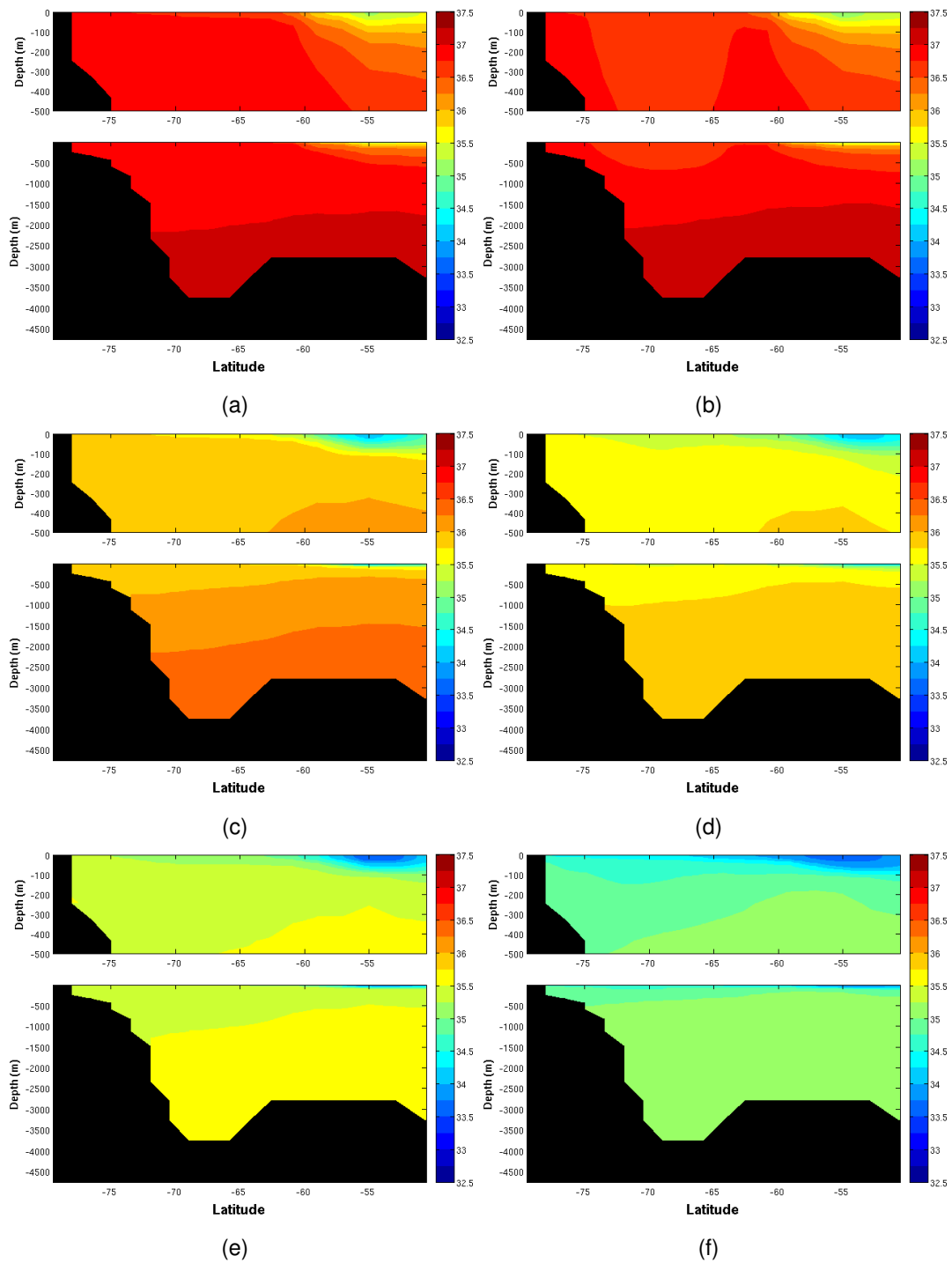


Figure 8.4: Salinity at the Weddell Sea transect at (a) 22 ka, (b) 19 ka, (c) 14.7 ka, (d) 12.9 ka, (e) 11.7 ka, and (f) 0 ka.

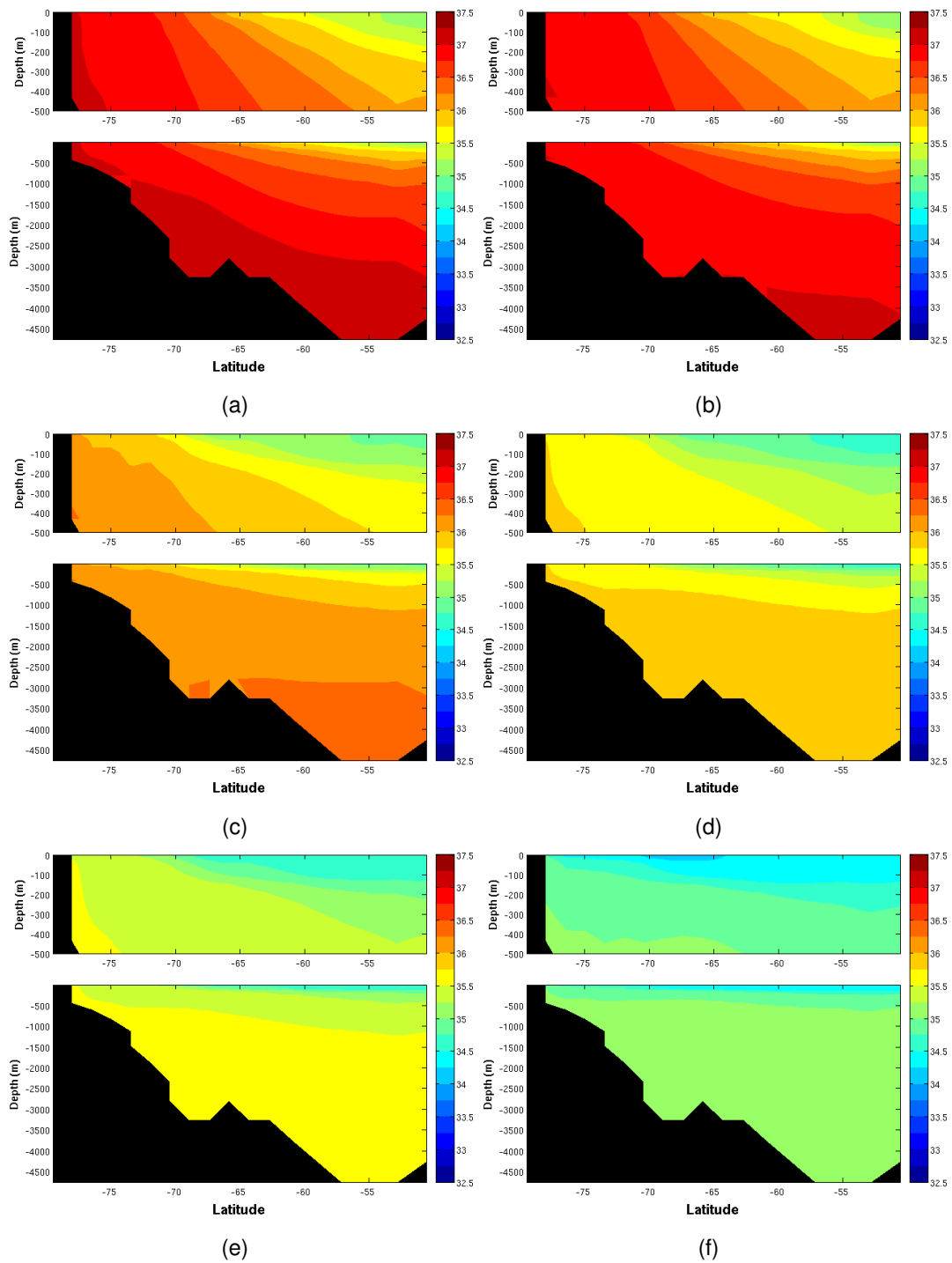


Figure 8.5: Salinity at the Ross Sea transect at (a) 22 ka, (b) 19 ka, (c) 14.7 ka, (d) 12.9 ka, (e) 11.7 ka, and (f) 0 ka.

## 8.2 The impact of the MWP-1A on the Southern Ocean dynamics

Figure 8.6 shows the evolution of surface ocean current speed, surface salinity, and wind stress averaged along 55°S and 65°S during the simulation. The 55°S band is on the Antarctic Circumpolar Current (ACC) pathway, while the 65°S band is on the Antarctic Coastal Current (ACoC) pathway.

A general negative trend can be noted in the three variables at 55°S. Although there is still controversy about the position and strength of westerlies during and after the LGM (Kohfeld et al., 2013), there are studies that point out to stronger winds at the LGM in high southern latitudes (e.g. Wainer et al., 2005), as we see in the top panel of Figure 8.6. The salinity at 55°S decreases according to the prescribed freshwater fluxes, with a major drop possibly associated with the northward transport of the meltwater from the Antarctic ice sheet during the Meltwater Pulse 1A (MWP-1A). The current speed, as the salinity, has a major drop around 14 ka, but the speed negative peak happens before the salinity one.

At 65°S, the wind stress increases from the LGM to around 12 ka, and then maintains a relative stable level on the remaining simulation. This variability is quite different from salinity and current speed time series. The salinity slightly decreases over time while the current speed is almost constant, and both of them have a large peak around 14 ka — positive for current speed and negative for salinity.

Although the general negative trend in the ACC velocity might be essentially a response to the wind stress weakening, it seems that the current speed variability is associated with the changes in surface salinity. The wind stress is thought to be the main driver of the ACC (e.g. Gill, 1968; Allison et al., 2010), but Hogg (2010) points out the importance of surface buoyancy controlling ACC intensity. Here, we think that the melting of the Antarctic ice sheet played an important role in the Southern Ocean dynamics. Normally, in a meridional section across the Southern Ocean, the isopycnals rise polewards since the surface waters near the Antarctic shelf are much

denser compared to surface waters farther north. The sea level, on the other hand, is higher equatorward. This scenario produces a pressure gradient force from mid- to high-latitudes, which forces the water to flow poleward (Figure 8.7(a)). This flow is ultimately deflected to the left due to Earth's rotation, reinforcing the ACC — which flows eastward — and weakening the ACoC — which flows westward (Figure 8.7(a)). When freshwater is released around Antarctica, the isopycnals deepen and the surface level rises near the coast. This weakens or inverts the pressure gradient force, resulting in a flow that is opposite to ACC's direction (Figure 8.7(b)). In this case, the ACoC is intensified. This scenario would explain the well-correlated peaks around the time of the MWP-1A, where an abrupt reduction of salinity is immediately accompanied by an intensified ACC (Figure 8.6, bottom). The lag between the minimum salinity and ACC's speed drop (Figure 8.6, top) might be explained depending on the adjustment time of the northward flow of freshwater relative to the pressure gradient generated by the presence of freshwater over the shelf.

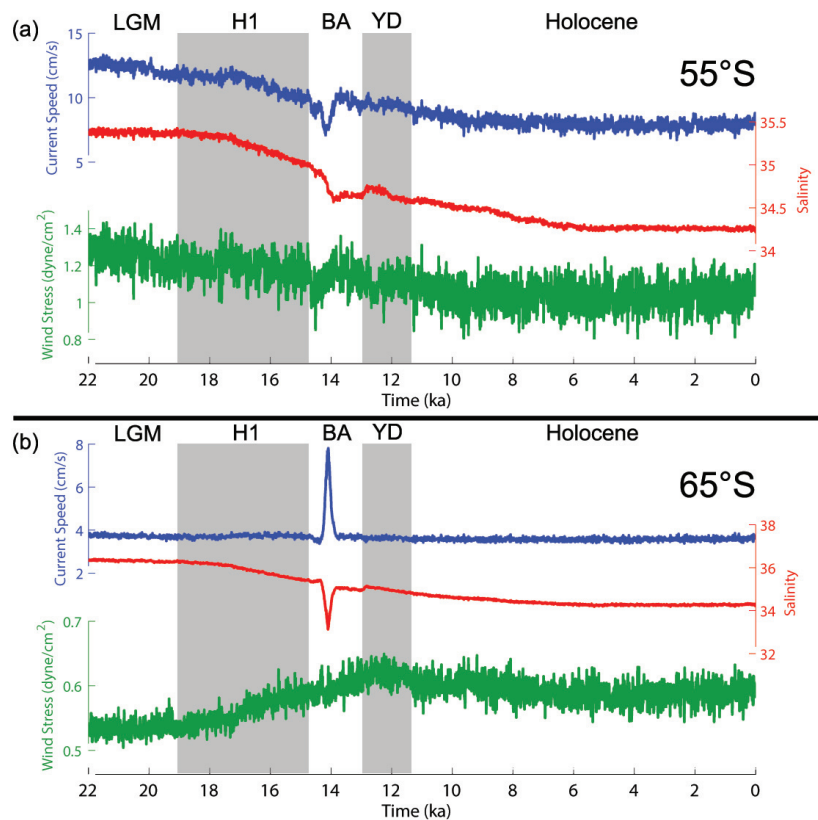


**Figure 8.6:** Current speed at the ocean surface (blue line), salinity (red line) and wind stress (green line) at 55°S (top) and 65°S (bottom).

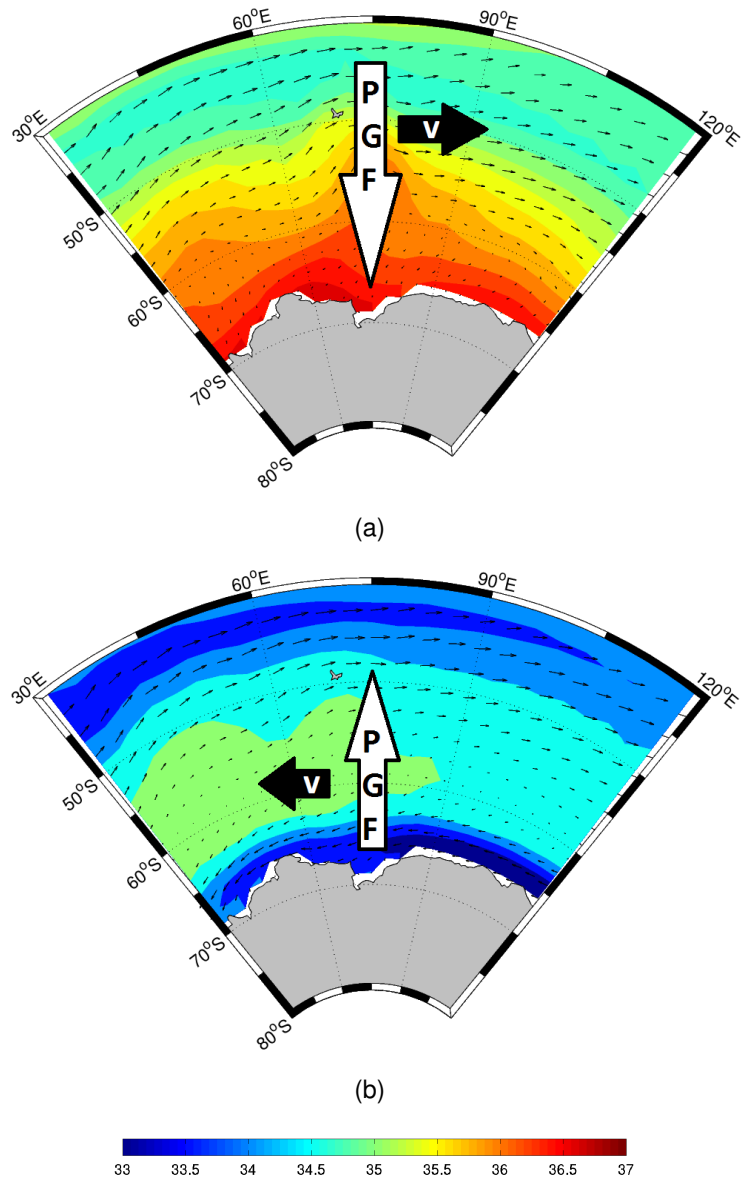


**Figure 8.7:** Salinity gradient (colors), the pressure gradient force (PGF) generated (white arrow), and the resulting flow direction (black arrow) at (a) 21 ka and (b) 14.1 ka (during the MWP-1A).

## CHAPTER 9

---

## The Indian Ocean's response to meltwater fluxes

---

**S**MALLER than the Atlantic and Pacific Oceans, the Indian Ocean is unique because it is limited up to 25°N, where it encounters the Asiatic landmass. This ocean has also a limited connection with the Atlantic Ocean since the African landmass stands between the two of them. The only direct communication between the Atlantic and the Indian Ocean occurs between the tip of Africa and Antarctica. Since there is no direct water exchange between the Indian and the North Atlantic, this ocean is a good laboratory where we can isolate and analyze the effects of a meltwater pulse coming from the Southern Ocean.

## 9.1 The Indian Ocean's characteristics

In the Indian Ocean, the surface circulation can be divided into two systems: a subtropical gyre in the southern hemisphere and a seasonal regime in the tropics and in the Northern Hemisphere, driven by the monsoonal regime. These two systems are limited at around 10-12°S by the nearly zonal Southern Equatorial Current (Talley et al., 2011). In the boreal summer, strong southwestern winds dominate the Arabian Sea area. These winds reverse northeastward during the winter (Figure 9.1). The change in the wind regime affects the ocean currents in this area. During the summer, the West and East Indian Coastal Current (WICC and EICC) flow eastward, as well as the Southwest Monsoon Current, which is present only at this season. During the winter, the WICC, the EICC, and the Northeast Monsoon Current flow westward (Figure 9.2, Talley et al., 2011).

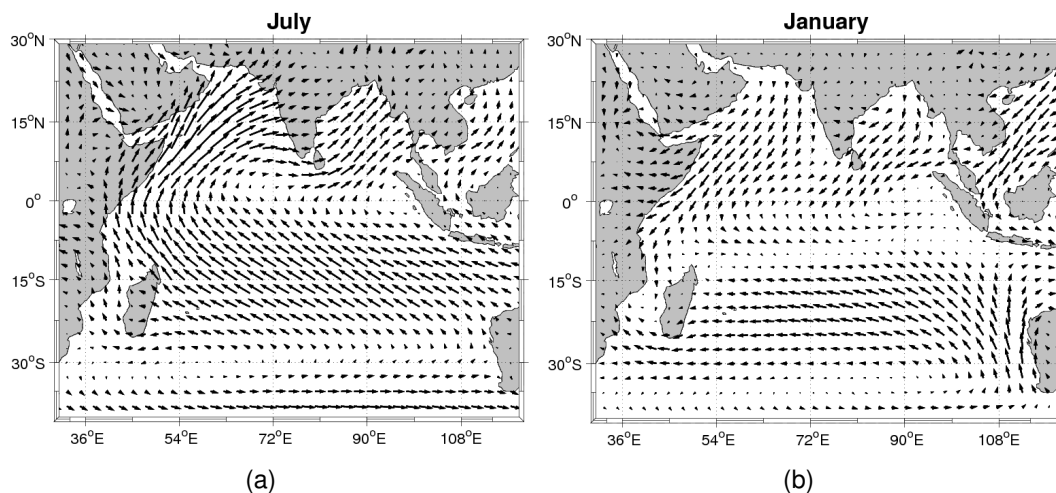


**Figure 9.1:** Present climatological winds over the Indian Ocean for (a) July and (b) January from NCEP reanalysis<sup>1</sup>.

The North Indian Ocean has also a salinity contrast between west and east of India. The Arabian Sea is dominated by the high salinity outflows from the Persian Gulf and Red Sea. The Bay of Bengal, on the other hand, is under the influence of major river discharges, which gives this part of the ocean its low salinity characteristic. At intermediate depths, we also find a salinity contrast in the north-south axis of the western Indian Ocean (Figure 9.3). Coming from south, there is a low salinity tongue

<sup>1</sup>Data obtained at: <http://www.esrl.noaa.gov/psd/data/histdata/>

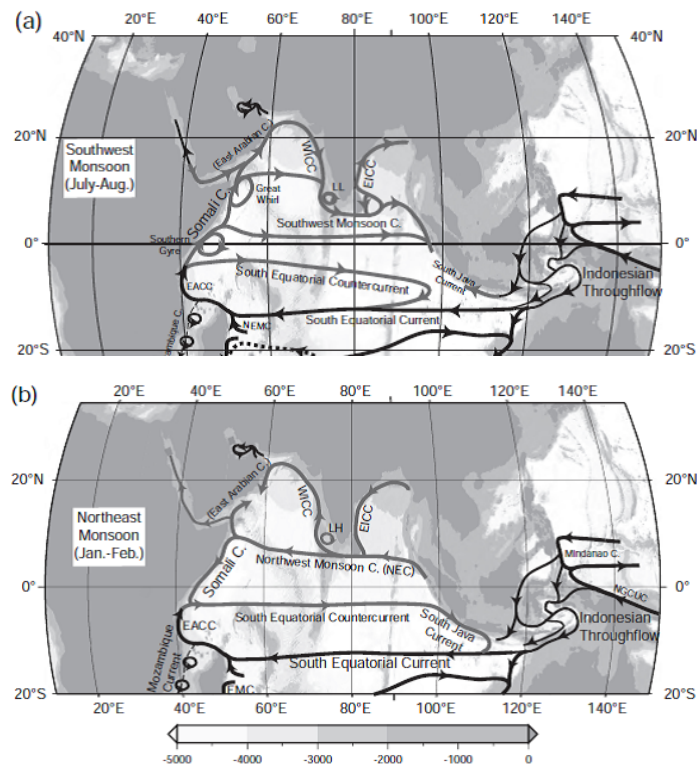


**Figure 9.2:** Indian Ocean surface circulation for (a) summer and (b) winter. Adapted from Talley et al. (2011).

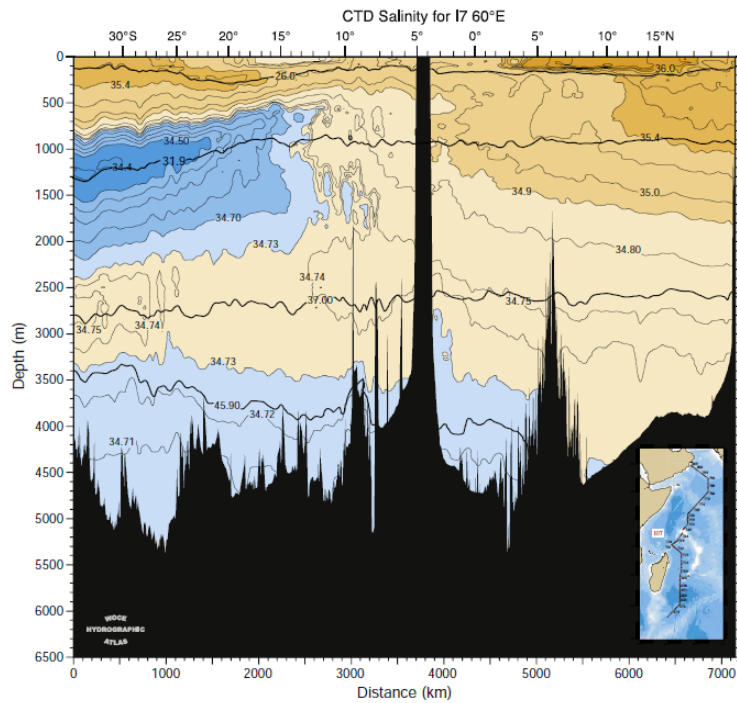


**Figure 9.3:** Modern western Indian Ocean vertical salinity distribution at the transect indicated in the detail plot, obtained during the WOCE program (figure from Talley et al., 2011).

that indicates the presence of Antarctic Intermediate Water. From north, a salty water mass originated in the Red Sea extends southward (the Red Sea Water, RSW, with influences of the Persian Gulf waters). Generally, the limit between these two water masses is around 5°S (You, 1998). At larger depths, AABW dominates.

## 9.2 Impacts of meltwater pulses on the Indian Ocean

In order to compare the state of the Indian Ocean during the last deglaciation with the modern state described above, we chose to observe the western Indian in a meridional transect at 53°E. Figure 9.4 shows the salinity distribution in this transect at different times. At the LGM (Figure 9.4(a)), the vertical stratification is reinforced by the presence of the salty version of the AABW (Adkins et al., 2002). The stratification gradually weakens as the simulation advances in time (as we saw previously in the Atlantic Ocean). At 14 ka (Figure 9.4(c)), the AAIW is much fresher and occupies a larger domain than before, while RSW is retracted. After that, the AAIW tongue weakens but the RSW plume does not return to its glacial extension. The freshening of the AAIW at 14 ka is probably associated to the MWP-1A, since part of this water mass is formed through the subduction of southern surface waters at the Subantarctic Front (e.g. Sloyan and Rintoul, 2001).

Analyzing the region where AAIW and RSW meet (between 10°S and the equator), it is possible to observe when one water mass overcome the other through the mean salinity variation in intermediate depths (Figure 9.5(a)). In general, the salinity between 200 and 1000 m increases about 0.25 during the H1, after which the values drop drastically until 14 ka, during the MWP-1A. At the YD, the salinity increases by 0.25 again and drops slightly toward Holocene levels. The surface mean salinity follow the intermediate layer variability, but has lower salinity values. From 1000 m to the bottom, region of AABW's dominion, the salinity reduction is approximately monotonous during the deglaciation.

The potential temperature for the same layers is presented in Figure 9.5(b).

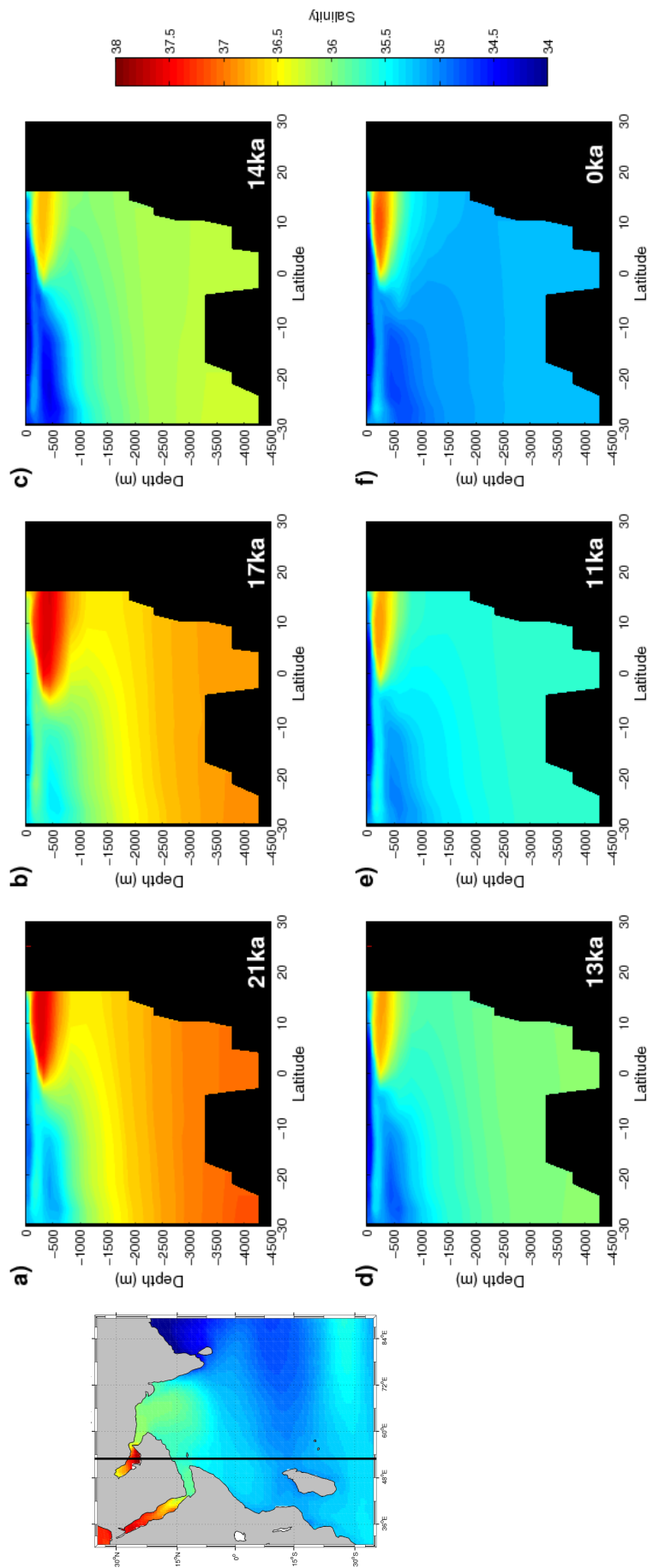


**Figure 9.4:** Indian Ocean vertical salinity distribution at 53°E (transect indicated in the map on the left) from TraCE-21K simulation at different periods: (a) 21 ka; (b) 17 ka; (c) 14 ka; (d) 13 ka; (e) 11 ka; (f) 0 ka.

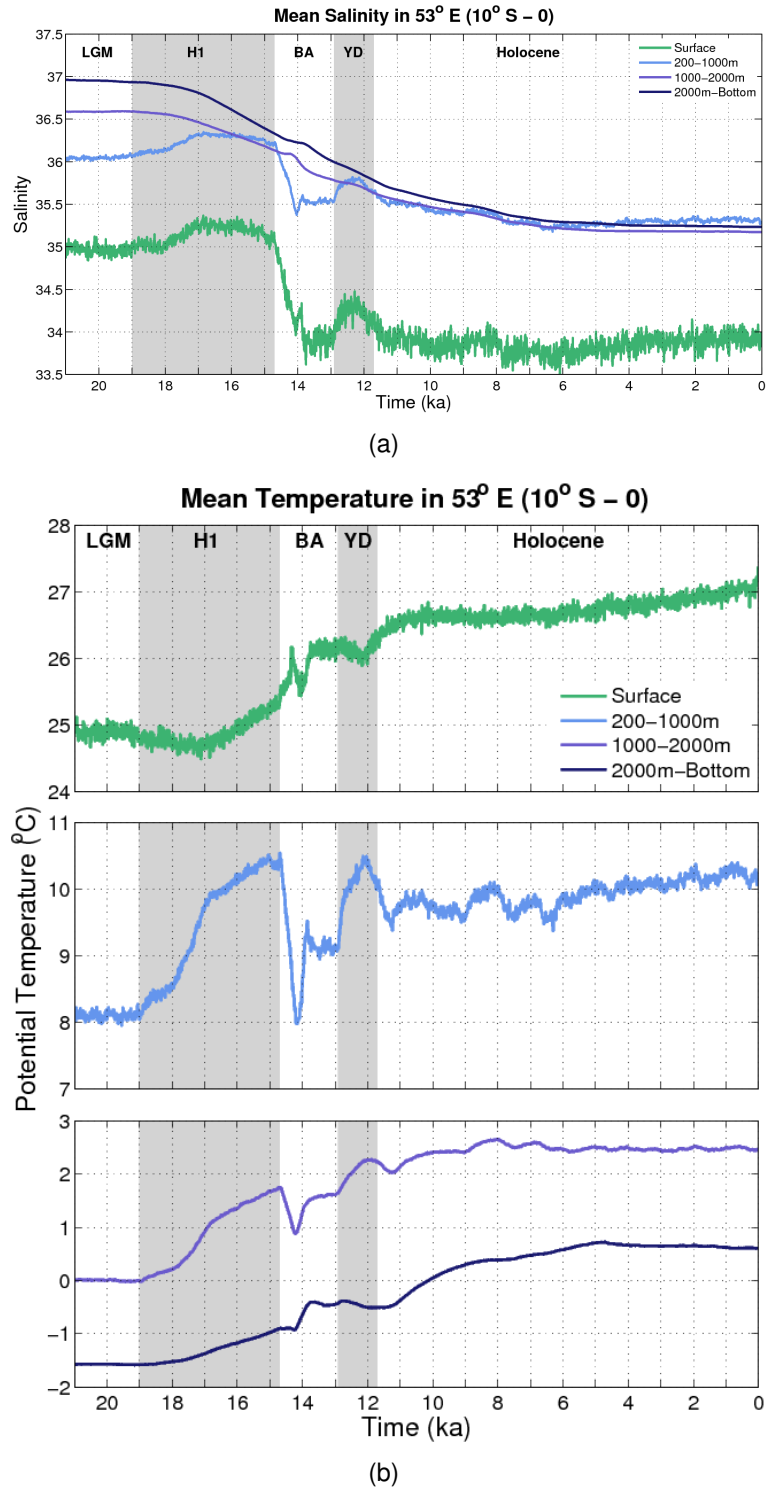


**Figure 9.5:** Southwest Indian Ocean (at 53°E) mean (a) salinity and (b) temperature between 10°S and the equator at different depth ranges, as indicated by the legend.

We observe that the evolution of temperature in the intermediate layer (200-1000 m) is similar to the Antarctic air temperature reconstruction (Figure 2.2, middle, purple line) and its variability is larger compared to the temperature variability at the sur-

face. Kiefer et al. (2006) show that the temperature variations in the western tropical Indian, reconstructed from  $\delta^{18}\text{O}$  and Mg/Ca records, remarkably resemble the temperature recorded in Antarctic ice cores. The authors point the Subantarctic Mode Water (SAMW) — which can be considered part of the AAIW — as the responsible for the link between these two regions. The SAMW is formed between the Subantarctic and Subtropical Fronts, when it is subducted to depths around 200-600 m and moves equatorward, where it upwells at the thermocline base. This way, the signal is clearer at intermediate depths, as observed in Figure 9.5(b). Kiefer et al. (2006) hypothesis was later reinforced by Naidu and Govil (2010) and Romahn et al. (2013).

The surface temperatures seem to mix the patterns observed in Antarctic and Greenland ice cores, which indicates that the western Indian Ocean responds to the climatic variability of both hemispheres.

The  $\theta - S$  diagram for the same region (53°E, between 10°S and the equator) is presented in Figure 9.6. It can be seen that the curve has a salinity maximum at intermediate temperatures. This maximum is associated with the dominance of RSW over AAIW between 10°S and the equator. According to You (1998), the boundary between RSW and AAIW is usually placed around 5°S, as we mentioned before. As indicated in the  $\theta - S$  diagram, the salinity maximum is larger at 15 ka, while at 14.1 ka it reverses to a salinity minimum. The observed change may be associated with the northward expansion of the AAIW during the BA period.

In order to explain this variability in the northern limit of AAIW, we first investigated the atmospheric forcings. The Figure 9.7 shows the variability of the wind stress over the equator during the last 22 thousand years. Comparing this time series with the one associated to the temperature at Greenland (Figure 2.2) we note the similarity between them. The reduction of southwest winds (weakened summer monsoon) is associated with cold periods in the North Atlantic.

In a study with dinoflagellates related to upwelling at the Somalian coast, Zonneveld et al. (1997) found the following sequence of events associated with the monsoon system in the Indian Ocean since the LGM:

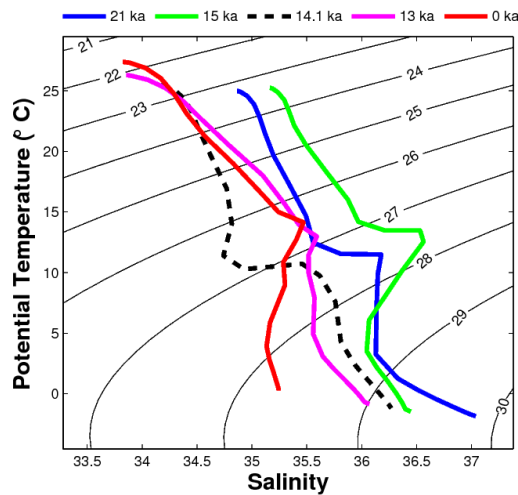


**Figure 9.6:**  $\theta - S$  diagram for the Indian Ocean at  $53^\circ\text{E}$  between  $10^\circ\text{S}$  and the equator at different periods.

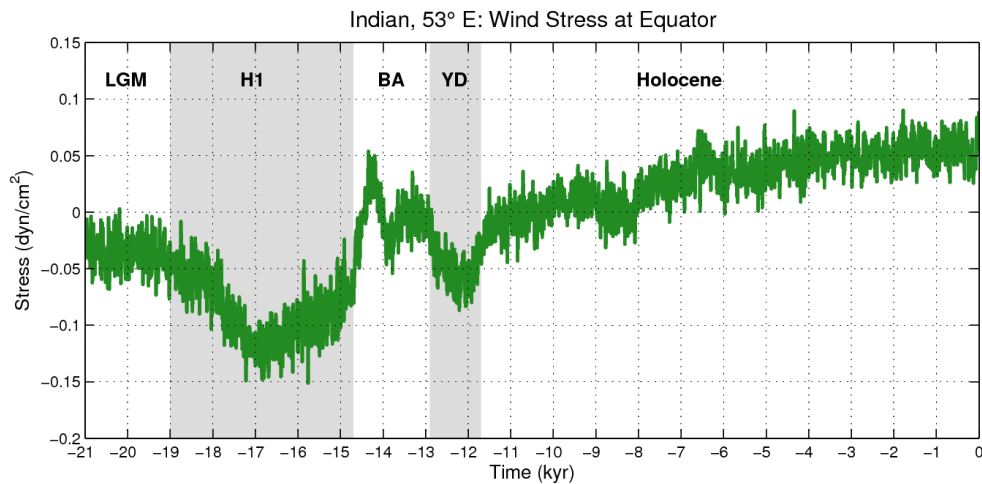


**Figure 9.7:** Wind stress time series at the equator,  $53^\circ\text{E}$ .

- 21.9 to 17.4 ka → Southwest (SW) monsoon not too intense;
- 17.2 to 14.7 ka → SW monsoon extremely weak;
- 14.7 ka → Rapid transition toward stronger SW monsoon;
- 14.7 ka to 11.8 ka → Several short pulses of low intensity SW monsoon (Younger Dryas);
- Holocene → Rising values, reaching a maximum at 7.2 ka, and sharp decrease between 4.5 and 2.5 ka.

The same sequence of events can be observed in the Figure 9.7, with exception of the abrupt decline during the Holocene. We notice that the expansion phase

of AAIW observed at Figures 9.4 and 9.6 is associated to the period of intense SW monsoons at the BA. Strong SW winds implicate in a reduced outflow from the Red Sea equatorward (which is consistent with the surface circulation observed at Figure 9.2), allowing AAIW to reach its northernmost position.

Another important feature of the tropical Indian Ocean responds to climatic variations in the model: the Equatorial Undercurrent (EUC). In the Figure 9.8, we observe the variability in the core speed of this current along the simulation. The increase in the speed core is consistent with the intensification of the SW monsoons. The core depth almost does not change, rising slightly during the H1.

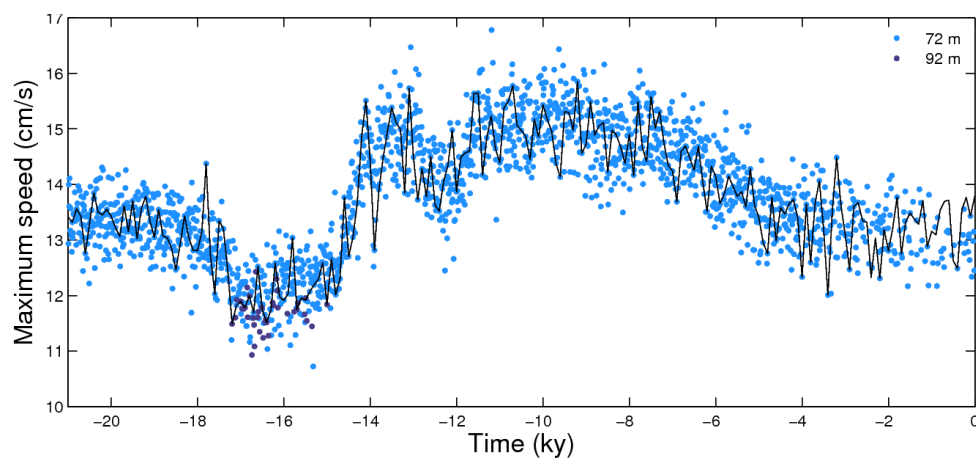


**Figure 9.8:** EUC core speed and depth at 53°E.

## CHAPTER 10

---

# General Conclusions and Final Considerations

---

This study examined, through the analysis of the results of a transient paleoclimate numerical simulation with the NCAR-CCSM3 from the 21,000 years ago to present day, the evolution of the deep Atlantic (and western Indian) Ocean circulation under meltwater forcing. We went through a brief review of the climatic events since the LGM (Chapter 2); analyzed the changes in the Atlantic's circulation, from the variability of the AMOC and its associated heat and salt transports to the changes in the thermohaline structure and water masses distribution (Chapters 4 to 7); assessed the direct impacts of the presence of freshwater on the Antarctic shelf (Chapter 8); and investigated the indirect impact of the meltwater discharges in the dynamics of the western Indian Ocean (Chapter 9). As these last two chapters (8 and 9) were not explored as deeply as the ones concerning the Atlantic Ocean, we suggest that TraCE-21K data for the Southern Ocean and the Indian Ocean are further investigated in the future.

---

The main conclusions we have found are:

1. The glacial ocean (21 ka) was very stable, stratified, and its layers did not mix as much as they do today. The main reason for this vertical configuration was the production of a salty version of AABW, which occupied most of the deep ocean basins. The presence of this very dense water mass below 2000 m of depth did not allow the intrusion of the northern water mass to the modern NADW level. At 12 ka, AABW's distribution was drastically reduced by the appearance of NADW;
2. AABW had a gradual warming and freshening since the LGM, except for the small warming peak during the MWP-1A, associated with reduced upwelling of northern warm waters;
3. As the upper North Atlantic gets flooded by freshwater during the H1 and this freshwater reaches the deep ocean through the Southern Ocean, the ocean's vertical structure starts changing but the salinity stratification still only allows the formation of an intermediate water mass in the North Atlantic, the so-called GNAIW;
4. GNAIW was a cold water mass, fresher than AABW that existed in the beginning of the deglaciation; its characteristics made GNAIW very similar to AAIW; GNAIW was shallower than NADW and could not spread as much southward;
5. GNAIW's formation progressively weakened during the Heinrich Stadial 1 — which caused the MOC to slow down — and was finally replaced by modern NADW after 12 ka;
6. The impact on the ocean structure resulting from the continuous freshening allows the erosion of the salinity barrier that was preventing the spread of the NADW into the South Atlantic. The newly formed NADW is allowed to sink and spreads southward;

7. Since 12 ka, NADW has been formed by contributions from both Nordic Seas overflow and the Labrador Sea Water. Prior to this, GNAIW was mainly formed by Nordic Seas overflow;
8. During the Holocene, the vertical distribution of salinity (related to the distribution of Atlantic water masses) reaches its modern-day pattern. Therefore, the present-day NADW owes its spatial structure to the impact of several freshwater discharges in the Atlantic, which contributed to the erosion of the subsurface salinity barrier formed at LGM.
9. AAIW seems to have weakened during the cold events H1 and YD;
10. The presence of freshwater over the Antarctic shelf shortly induced the intensification of the Antarctic Coastal Current and the slowdown of the Antarctic Circumpolar Current. The connection between the salinity field and the current speeds happens through the change in the meridional pressure gradient and its resulting flow;
11. The western tropical Indian Ocean responds to the climatic variations from both hemispheres: the Northern Hemisphere through the atmosphere and the Southern Hemisphere essentially through the ocean. Wang et al. (2013) point the influence of both hemispheres in the Indian Ocean, highlighting that the signal captured by each proxy may differ according to the phytoplankton preference to the southern winter or summer. According to these authors, the variation of the ITCZ position favors the record of the NH temperatures when the same is displaced southward and the record of SH temperatures when it is displaced northward.

It is worth to notice that we analyzed a single transient run where no control simulation or other companion sensitivity experiments were available to assess uncertainties and robustness of the results with respect to each individual meltwater flux. Furthermore, there are other intrinsic uncertainty sources such as the prescribed meltwater flux in TraCE-21 (that is obtained indirectly from sea level records) plus the

fact that the timing, magnitude and location of MWP-1A, associated with global sea level change, has significant uncertainty as well. Since the meltwater fluxes were prescribed, it does not necessarily mean that the model has the correct sensitivity to the freshwater input. In this respect, interpretation of the results has to be taken with caution considering that the lack of a control run does not allow us to single out cause and effect relationships relative to individual events.

Moreover, the method of analysis employed to determine the water masses distribution is quite simplistic. Using only two physical properties to identify four water masses is somewhat limiting. Nevertheless, the information this analysis produced is of considerable value, especially because it shows the continuous evolution of the deep Atlantic water masses since the LGM. The formation regions indicated by the highest percentages of contribution at thermocline levels are consistent with much of the oceanographic data literature. In addition, the main water mass distribution patterns formed are quite reasonable. We believe that this work gives new insights into the evolution, on the millennial time scale, of the deep Atlantic circulation in the last 21,000 years.

---

## Academic production

---

### **Papers presented in scientific events**

1. Antarctic coastal circulation changes and their possible causes. World Climate Research Programme (WCRP) Open Science Conference, 2011, Denver, USA [POSTER]
2. Simulated freshwater pulses since Last Glacial Maximum: impacts in the Atlantic and Southern Oceans. APECS Meeting, 2012, Rio Grande, Brazil [PLENARY SESSION]
3. Impacts of a meltwater pulse originated on the Southern Ocean at 14ky BP from a NCAR-CCSM3 simulation.
  - (a) LaACER Meeting, 2012, Bogota, Colombia [ORAL]
  - (b) International Polar Year, 2012, Montreal, Canada [POSTER]
4. Impacts of the Meltwater Pulse 1A (MWP-1A) on the Atlantic Ocean's circulation. Second meeting of INCT-Criosfera, 2013, Bento Gonçalves, Brazil [ORAL]
5. The role of meltwater fluxes in the evolution of Atlantic Ocean's deep circulation

since the Last Glacial Maximum. 48th Canadian Meteorological and Oceanographic Society Congress, 2014, Rimouski, Canada [POSTER]

### **Publications**

1. Marson, J. M., Wainer, I., Mata, M. M., and Liu, Z.: The impacts of deglacial meltwater forcing on the South Atlantic Ocean deep circulation since the Last Glacial Maximum, *Clim. Past*, 10, 1723-1734, doi:10.5194/cp-10-1723-2014, 2014.
2. Marson, J. M., Mysak, L. A., Mata, M. M., and Wainer, I. Evolution of the deep Atlantic water masses since the Last Glacial Maximum based on a transient run of NCAR-CCSM3. Under review in *Climate Dynamics*.

---

## Bibliography

---

- Adkins, J. F. (2013). The role of deep ocean circulation in setting glacial climates. *Paleoceanography*, 28(3):539–561.
- Adkins, J. F., McIntyre, K., and Schrag, D. P. (2002). The salinity, temperature, and  $\delta^{18}\text{O}$  of the glacial deep ocean. *Science (New York, N.Y.)*, 298(5599):1769–73.
- Alley, R. B. (2000a). Ice-core evidence of abrupt climate changes. *Proceedings of the National Academy of Sciences of the United States of America*, 97(4):1331–4.
- Alley, R. B. (2000b). The Younger Dryas cold interval as viewed from central Greenland. *Quaternary Science Reviews*, 19(1-5):213–226.
- Alley, R. B. and Clark, P. U. (1999). The deglaciation of the Northern Hemisphere: A Global Perspective. *Annual Review of Earth and Planetary Sciences*, 27(1):149–182.
- Alley, R. B., Mayewski, P. A., Sowers, T., Stuiver, M., Taylor, K. C., and Clark, P. U. (1997). Holocene climatic instability: A prominent, widespread event 8200 yr ago. *Geol*, 25(6):483.

- Allison, L. C., Johnson, H. L., Marshall, D. P., and Munday, D. R. (2010). Where do winds drive the antarctic circumpolar current? *Geophys. Res. Lett.*, 37(12):L12605.
- Andrews, J., Jennings, A., Kerwin, M., Kirby, M., Manley, W., Miller, G., Bond, G. C., and MacLean, B. (1995). A Heinrich-like event, H-0 (DC-0): Source (s) for detrital carbonate in the North Atlantic during the Younger Dryas Chronozone. *Paleoceanography*, 10(5):943–952.
- Annan, J. D. and Hargreaves, J. C. (2013). A new global reconstruction of temperature changes at the Last Glacial Maximum. *Climate of the Past*, 9(1):367–376.
- Barker, S., Diz, P., Vautravers, M. J., Pike, J., Knorr, G., Hall, I. R., and Broecker, W. S. (2009). Interhemispheric Atlantic seesaw response during the last deglaciation. *Nature*, 457(7233):1097–1102.
- Bassett, S. E., Milne, G. A., Mitrovica, J. X., and Clark, P. U. (2005). Ice sheet and solid Earth influences on far-field sea-level histories. *Science (New York, N.Y.)*, 309(5736):925–8.
- Berger, A. (1978). Long-Term Variations of Daily Insolation and Quaternary Climatic Changes. *Journal of the Atmospheric Sciences*, 35(12):2362–2367.
- Blaschek, M., Bakker, P., and Renssen, H. (2014). The influence of Greenland ice sheet melting on the atlantic meridional overturning circulation during past and future warm periods: a model study. *Climate Dynamics*, pages 1–21.
- Blunier, T. and Brook, E. J. (2001). Timing of millennial-scale climate change in Antarctica and Greenland during the last glacial period. *Science (New York, N.Y.)*, 291(5501):109–12.
- Bohm, E., Lippold, J., Gutjahr, M., Frank, M., Blaser, P., Antz, B., Fohlmeister, J., Frank, N., Andersen, M. B., and Deininger, M. (2014). Strong and deep atlantic meridional overturning circulation during the last glacial cycle. *Nature*, 517(7532):73–76.

- Bond, G. C., Broecker, W. S., Johnsen, S. J., McManus, J. F., Labeyrie, L., Jouzel, J., and Bonani, G. (1993). Correlations between climate records from North Atlantic sediments and Greenland ice. *Nature*, 365(6442):143–147.
- Bond, G. C., Kromer, B., Beer, J., Muscheler, R., Evans, M. N., Showers, W., Hoffmann, S., Lotti-Bond, R., Hajdas, I., and Bonani, G. (2001). Persistent solar influence on North Atlantic climate during the Holocene. *Science (New York, N.Y.)*, 294(5549):2130–6.
- Bond, G. C. and Lotti, R. (1995). Iceberg Discharges into the North Atlantic on Millennial Time Scales During the Last Glaciation. *Science*, 267(5200):1005–1010.
- Bond, G. C., Showers, W., Cheseby, M., Lotti, R., Almasi, P., DeMenocal, P., Priore, P., Cullen, H., Hajdas, I., and Bonani, G. (1997). A Pervasive Millennial-Scale Cycle in North Atlantic Holocene and Glacial Climates. *Science*, 278(5341):1257–1266.
- Boville, B. a. and Gent, P. R. (1998). The NCAR Climate System Model, Version One. *Journal of Climate*, 11(6):1115–1130.
- Boyle, E. A. and Keigwin, L. D. (1987). North Atlantic thermohaline circulation during the past 20,000 years linked to high-latitude surface temperature. *Nature*, 330(6143):35–40.
- Brady, E. C. and Otto-Bliesner, B. L. (2010). The role of meltwater-induced subsurface ocean warming in regulating the Atlantic meridional overturning in glacial climate simulations. *Climate Dynamics*, 37(7-8):1517–1532.
- Briegleb, B. P., Bitz, C. M., Hunke, E. C., Limpscomb, W., Holland, M. M., Schramm, J. L., and Moritz, R. (2004). Scientific description of the sea ice component in the Community Climate System Model, version three. Technical report, NCAR Technical Note NCAR/TN-463STR.
- Broecker, W. S. (1994). Massive iceberg discharges as triggers for global climate change. *Nature*, 372(6505):421–424.

- Broecker, W. S. (1998). Paleocean circulation during the Last Deglaciation: A bipolar seesaw? *Paleoceanography*, 13(2):119–121.
- Broecker, W. S., Peacock, S. L., Walker, S., Weiss, R., Fahrback, E., Schroeder, M., Mikolajewicz, U., Heinze, C., Key, R., Peng, T.-H., and Rubin, S. (1998). How much deep water is formed in the Southern Ocean? *Journal of Geophysical Research*, 103(C8):15833–15843.
- Came, R. E., Oppo, D. W., Curry, W. B., and Lynch-Stieglitz, J. (2008). Deglacial variability in the surface return flow of the Atlantic meridional overturning circulation. *Paleoceanography*, 23(1):PA1217.
- Carlson, A. E. (2009). Geochemical constraints on the Laurentide Ice Sheet contribution to Meltwater Pulse 1A. *Quaternary Science Reviews*, 28(17-18):1625–1630.
- Carlson, A. E., LeGrande, A. N., Oppo, D. W., Came, R. E., Schmidt, G. a., Anslow, F. S., Licciardi, J. M., and Obbink, E. a. (2008). Rapid early Holocene deglaciation of the Laurentide ice sheet. *Nature Geoscience*, 1(9):620–624.
- Cheng, W., Bitz, C. M., and Chiang, J. C. H. (2007). Adjustment of the global climate to an abrupt slowdown of the Atlantic meridional overturning circulation. In *Ocean Circulation: Mechanisms and Impacts*, pages 295–313. Geophysical Monograph Series 173.
- Clark, P. U., Dyke, A. S., Shakun, J. D., Carlson, A. E., Clark, J., Wohlfarth, B., Mitrovica, J. X., Hostetler, S. W., and McCabe, A. M. (2009). The Last Glacial Maximum. *Science (New York, N.Y.)*, 325(5941):710–4.
- Clark, P. U., Marshall, S. J., Clarke, G. K., Hostetler, S. W., Licciardi, J. M., and Teller, J. T. (2001). Freshwater forcing of abrupt climate change during the last glaciation. *Science (New York, N.Y.)*, 293(5528):283–7.
- Clark, P. U., McCabe, a. M., Mix, A. C., and Weaver, A. J. (2004). Rapid rise of sea level 19,000 years ago and its global implications. *Science (New York, N.Y.)*, 304(5674):1141–4.

- Clark, P. U., Mitrovica, J. X., Milne, G., and Tamisiea, M. (2002a). Sea-level fingerprinting as a direct test for the source of global meltwater pulse IA. *Science*, 2438(2002):10–14.
- Clark, P. U. and Mix, A. C. (2002). Ice sheets and sea level of the Last Glacial Maximum. *Quaternary Science Reviews*, 21(1-3):1–7.
- Clark, P. U., Pisias, N. G., Stocker, T. F., and Weaver, A. J. (2002b). The role of the thermohaline circulation in abrupt climate change. *Nature*, 415(February):863–869.
- Clauzet, G., Wainer, I., Lazar, A., Brady, E. C., and Otto-Bliesner, B. L. (2007). A numerical study of the South Atlantic circulation at the Last Glacial Maximum. *Palaeogeography, Palaeoclimatology, Palaeoecology*, 253(3-4):509–528.
- Collins, W. D., Rasch, P. J., Boville, B. A., Hack, J. J., McCaa, J. R., Williamson, D. L., Briegleb, B. P., Bitz, C. M., Lin, S.-J., and Zhang, M. (2006). The Formulation and Atmospheric Simulation of the Community Atmosphere Model Version 3 (CAM3). *Journal of Climate*, 19(11):2144–2161.
- Cottet-Puinel, M., Weaver, A. J., Hillaire-Marcel, C., de Vernal, A., Clark, P. U., and Eby, M. (2004). Variation of Labrador Sea Water formation over the Last Glacial cycle in a climate model of intermediate complexity. *Quaternary Science Reviews*, 23(3-4):449–465.
- Crocket, K. C., Vance, D., Gutjahr, M., Foster, G. L., and Richards, D. a. (2011). Persistent Nordic deep-water overflow to the glacial North Atlantic. *Geology*, 39(6):515–518.
- Cuffey, K. M. and Clow, G. D. (1997). Temperature, accumulation, and ice sheet elevation in central Greenland through the last deglacial transition. *Journal of Geophysical Research*, 102(C12):26383.
- Curry, W. B., Duplessy, J. C., Labeyrie, L. D., and Shackleton, N. J. (1988). Changes in the distribution of  $\delta^{13}\text{C}$  of deep water  $\Sigma\text{CO}_2$  between the Last Glaciation and the Holocene. *Paleoceanography*, 3(3):317–341.

- Curry, W. B. and Oppo, D. W. (2005). Glacial water mass geometry and the distribution of  $\delta^{13}\text{C}$  of  $\Sigma\text{CO}_2$  in the western Atlantic Ocean. *Paleoceanography*, 20(1):PA1017.
- Dällenbach, A., Blunier, T., Flückiger, J., Stauffer, B., Chappellaz, J., and Raynaud, D. (2000). Changes in the atmospheric  $\text{CH}_4$  gradient between Greenland and Antarctica during the Last Glacial and the transition to the Holocene. *Geophysical Research Letters*, 27(7):1005–1008.
- Deacon, G. (1937). *The hydrology of the Southern Ocean*. Discovery Rep., 15.
- Driesschaert, E., Fichefet, T., Goosse, H., Huybrechts, P., Janssens, I., Mouchet, A., Munhoven, G., Brovkin, V., and Weber, S. L. (2007). Modeling the influence of Greenland ice sheet melting on the atlantic meridional overturning circulation during the next millennia. *Geophys. Res. Lett.*, 34(10):L10707.
- Duplessy, J.-C., Shackleton, N. J., Fairbanks, R. G., Labeyrie, L., Oppo, D. W., and Kallel, N. (1988). Deepwater source variations during the last climatic cycle and their impact on the global deepwater circulation. *Paleoceanography*, 3(3):343–360.
- Duplessy, J.-c., Shackleton, N. J., Matthews, R. K., Prell, W., Ruddiman, W. F., Caralp, M., and Hendy, C. H. (1984).  $^{13}\text{C}$  Record of benthic foraminifera in the last interglacial ocean: Implications for the carbon cycle and the global deep water circulation. *Quaternary Research*, 21(2):225–243.
- Ellis, J. S., Haar, T. H. V., Levitus, S., and Oort, A. H. (1978). The annual variation in the global heat balance of the earth. *Journal of Geophysical Research*, 83(C4):1958.
- Fairbanks, R. G. (1989). A 17,000-year glacio-eustatic sea level record: influence of glacial melting rates on the Younger Dryas event and deep-ocean circulation. *Nature*, 342(6250):637–642.
- Ferrari, R., Jansen, M. F., Adkins, J. F., Burke, A., Stewart, A. L., and Thompson, A. F. (2014). Antarctic sea ice control on ocean circulation in present and glacial

- climates. *Proceedings of the National Academy of Sciences of the United States of America*, 111(24):8753–8.
- Flückiger, J., Dallenbach, A., Blunier, T., Stauffer, B., Stocker, T. F., Raynaud, D., and Barnola, J.-M. (1999). Variations in Atmospheric N<sub>2</sub>O Concentration During Abrupt Climatic Changes. *Science*, 285(5425):227–230.
- Gent, P. R., Bryan, F. O., Danabasoglu, G., Lindsay, K., Tsumune, D., Hecht, M. W., and Doney, S. C. (2006). Ocean chlorofluorocarbon and heat uptake during the twentieth century in the CCSM3. *Journal of Climate*, 19(11):2366–2381.
- Gherardi, J., Labeyrie, L., Nave, S., Francois, R., McManus, J. F., and Cortijo, E. (2009). Glacial-interglacial circulation changes inferred from 231 Pa/ 230 Th sedimentary record in the North Atlantic region. *Paleoceanography*, 24(2):1–14.
- Gill, A. E. (1968). A linear model of the antarctic circumpolar current. *J. Fluid Mech.*, 32(03):465.
- Gruber, N., Keeling, C. D., and Bates, N. R. (2002). Interannual variability in the north atlantic ocean carbon sink. *Science*, 298(5602):2374–2378.
- Hall, M. M. and Bryden, H. L. (1982). Direct estimates and mechanisms of ocean heat transport. *Deep Sea Research Part A. Oceanographic Research Papers*, 29(3):339–359.
- Hartmann, D. L. (1994). *Global physical climatology*, volume 56. Academic Press.
- Hawkins, E., Smith, R. S., Allison, L. C., Gregory, J. M., Woollings, T. J., Pohlmann, H., and de Cuevas, B. (2011). Bistability of the atlantic overturning circulation in a global climate model and links to ocean freshwater transport. *Geophys. Res. Lett.*, 38(10):L10605.
- Hays, J. D., Imbrie, J., and Shackleton, N. J. (1976). Variations in the Earth's Orbit: Pacemaker of the Ice Ages. *Science*, 194(4270):1121–32.

- He, F. (2011). *Simulating transient climate evolution of the last deglaciation with CCSM3*. PhD thesis, University of Wisconsin-Madison.
- Heinrich, H. (1988). Origin and consequences of cyclic ice rafting in the northeast Atlantic Ocean during the past 130,000 years. *Quaternary research*, 29(2):142–152.
- Hillaire-Marcel, C., de Vernal, A., Bilodeau, G., and Weaver, A. J. (2001). Absence of deep-water formation in the Labrador Sea during the last interglacial period. *Nature*, 410(6832):1073–7.
- Hofmann, M. and Rahmstorf, S. (2009). On the stability of the atlantic meridional overturning circulation. *Proceedings of the National Academy of Sciences*, 106(49):20584–20589.
- Hogg, A. M. (2010). An antarctic circumpolar current driven by surface buoyancy forcing. *Geophys. Res. Lett.*, 37(23):L23601.
- Hogg, N. G. and Owens, W. B. (1999). Direct measurement of the deep circulation within the Brazil Basin. *Deep Sea Research Part II: Topical Studies in Oceanography*, 46(1-2):335–353.
- Hu, A., Meehl, G. A., Han, W., and Yin, J. (2011). Effect of the potential melting of the Greenland ice sheet on the meridional overturning circulation and global climate in the future. *Deep Sea Research Part II: Topical Studies in Oceanography*, 58(17-18):1914–1926.
- Hughen, K. A., Overpeck, J. T., Lehman, S. J., Kashgarian, M., Southon, J. R., Peterson, L. C., Alley, R. B., and Sigman, D. M. (1998). Deglacial changes in ocean circulation from an extended radiocarbon calibration. *Nature*, 391(January):65–68.
- Indermühle, A., Monnin, E., Stauffer, B., Stocker, T. F., and Wahlen, M. (2000). Atmospheric CO<sub>2</sub> concentration from 60 to 20 kyr BP from the Taylor Dome Ice Core, Antarctica. *Geophysical Research Letters*, 27(5):735–738.

- IPCC (2013). *Climate Change 2013: The Physical Science Basis. Contribution of Working Group I to the Fifth Assessment Report of the Intergovernmental Panel on Climate Change*. Cambridge University Press.
- Johnson, G. C. (2008). Quantifying Antarctic Bottom Water and North Atlantic Deep Water volumes. *Journal of Geophysical Research*, 113(C5):1–13.
- Joos, F. and Spahni, R. (2008). Rates of change in natural and anthropogenic radiative forcing over the past 20,000 years. *PNAS*, 105(5):1425–1430.
- Jouzel, J., Masson-Delmotte, V., Cattani, O., Dreyfus, G., Falourd, S., Hoffmann, G., Minster, B., Nouet, J., Barnola, J.-M., Chappellaz, J., Fischer, H., Gallet, J. C., Johnsen, S. J., Leuenberger, M., Loulergue, L., Luethi, D., Oerter, H., Parrenin, F., Raisbeck, G. M., Raynaud, D., Schilt, A., Schwander, J., Selmo, E., Souchez, R., Spahni, R., Stauffer, B., Steffensen, J. P., Stenni, B., Stocker, T. F., Tison, J. L., Werner, M., and Wolff, E. W. (2007). Orbital and millennial Antarctic climate variability over the past 800,000 years. *Science (New York, N.Y.)*, 317(5839):793–6.
- Karl, T. R. and Trenberth, K. E. (2003). Modern global climate change. *Science*, 302(5651):1719–23.
- Keigwin, L. D. and Lehman, S. J. (1994). Deep circulation change linked to HEINRICH Event 1 and Younger Dryas in a middepth North Atlantic Core. *Paleoceanography*, 9(2):185–194.
- Kiefer, T., McCave, I. N., and Elderfield, H. (2006). Antarctic control on tropical Indian Ocean sea surface temperature and hydrography. *Geophysical Research Letters*, 33(24):L24612.
- Kohfeld, K., Graham, R., de Boer, A., Sime, L., Wolff, E., Le Quéré, C., and Bopp, L. (2013). Southern hemisphere westerly wind changes during the last glacial maximum: paleo-data synthesis. *Quaternary Science Reviews*, 68:76–95.
- Kukla, G. J., Bender, M. L., de Beaulieu, J.-L., Bond, G. C., Broecker, W. S., Cleveringa, P., Gavin, J. E., Herbert, T. D., Imbrie, J., Jouzel, J., Keigwin, L. D., Knudsen,

- K.-L., McManus, J. F., Merkt, J., Muhs, D. R., Müller, H., Poore, R. Z., Porter, S. C., Seret, G., Shackleton, N. J., Turner, C., Tzedakis, P. C., and Winograd, I. J. (2002). Last Interglacial Climates. *Quaternary Research*, 58(1):2–13.
- Levis, S., Bonan, G. B., Vertenstein, M., and Oleson, K. W. (2004). The community land model's dynamic global vegetation model (clm-dgvm): Technical description and user's guide. Technical report, NCAR Tech. Note TN-459+ IA, 50.
- Licciardi, J. M., Teller, J. T., and Clark, P. U. (1999). Freshwater routing by the Laurentide Ice Sheet during the last deglaciation. In *Mechanisms of global climate change at millennial time scales*, pages 177–201.
- Lippold, J., Luo, Y., Francois, R., Allen, S. E., Gherardi, J., Pichat, S., Hickey, B., and Schulz, H. (2012). Strength and geometry of the glacial Atlantic Meridional Overturning Circulation. *Nature Geoscience*, 5(11):813–816.
- Liu, Z. (2005). Atmospheric CO<sub>2</sub> forcing on glacial thermohaline circulation and climate. *Geophysical Research Letters*, 32(2):L02706.
- Liu, Z., Otto-Bliesner, B. L., He, F., Brady, E. C., Tomas, R., Clark, P. U., Carlson, A. E., Lynch-Stieglitz, J., Curry, W. B., Brook, E. J., Erickson, D., Jacob, R., Kutzbach, J. E., and Cheng, J. (2009). Transient simulation of last deglaciation with a new mechanism for Bolling-Allerod warming. *Science (New York, N.Y.)*, 325(5938):310–4.
- Loulergue, L., Schilt, A., Spahni, R., Masson-Delmotte, V., Blunier, T., Lemieux, B., Barnola, J.-M., Raynaud, D., Stocker, T. F., and Chappellaz, J. (2008). Orbital and millennial-scale features of atmospheric CH<sub>4</sub> over the past 800,000 years. *Nature*, 453(7193):383–6.
- Lüthi, D., Le Floch, M., Bereiter, B., Blunier, T., Barnola, J.-m., Siegenthaler, U., Raynaud, D., Jouzel, J., Fischer, H., Kawamura, K., Stocker, T. F., and Floch, M. L. (2008). High-resolution carbon dioxide concentration record 650,000-800,000 years before present. *Nature*, 453(7193):379–82.

- Lynch-Stieglitz, J., Adkins, J. F., Curry, W. B., Dokken, T. M., Hall, I. R., Herguera, J. C., Hirschi, J. J.-M., Ivanova, E. V., Kissel, C., Marchal, O., Marchitto, T. M., McCave, I. N., McManus, J. F., Mulitza, S., Ninnemann, U. S., Peeters, F., Yu, E.-F., and Zahn, R. (2007). Atlantic meridional overturning circulation during the Last Glacial Maximum. *Science (New York, N.Y.)*, 316(5821):66–9.
- MacAyeal, D. R. (1993). Binge/purge oscillations of the Laurentide ice sheet as a cause of the North Atlantic's Heinrich events. *Paleoceanography*, 8(6):775–784.
- Makou, M. C., Oppo, D. W., and Curry, W. B. (2010). South Atlantic intermediate water mass geometry for the last glacial maximum from foraminiferal Cd/Ca. *Paleoceanography*, 25(4):PA4101.
- Mamayev, O. I. (1975). *Temperature-Salinity Analysis of World Ocean Waters*. Elsevier Scientific Publishing Co, New York.
- Marchitto, T. M., Curry, W. B., and Oppo, D. W. (1998). Millennial-scale changes in North Atlantic circulation since the last glaciation. *Nature*, 393(6685):557–561.
- Marcott, S. A., Clark, P. U., Padman, L., Klinkhammer, G. P., Springer, S. R., Liu, Z., Otto-bliesner, B. L., Carlson, A. E., Ungerer, A., Padman, J., He, F., Cheng, J., and Schmittner, A. (2011). Ice-shelf collapse from subsurface warming as a trigger for Heinrich events. *Proceedings of the National Academy of Sciences of the United States of America*, 108(33):13415–13419.
- Marson, J. M., Wainer, I., Mata, M. M., and Liu, Z. (2014). The impacts of deglacial meltwater forcing on the South Atlantic Ocean deep circulation since the Last Glacial Maximum. *Climate of the Past*, 10(5):1723–1734.
- Mayewski, P. A., Rohling, E. E., Curt Stager, J., Karlén, W., Maasch, K. A., David Meeke, L., Meyerson, E. A., Gasse, F., van Kreveld, S., Holmgren, K., and et al. (2004). Holocene climate variability. *Quaternary Research*, 62(3):243–255.
- McCartney, M. S. (1977). Subantarctic Mode Water. *A voyage of discovery*, 24:103–119.

- McManus, J. F., Francois, R., Gherardi, J., Keigwin, L. D., and Brown-Leger, S. (2004). Collapse and rapid resumption of Atlantic meridional circulation linked to deglacial climate changes. *Nature*, 428(6985):834–7.
- Menviel, L., England, M. H., Meissner, K. J., Mouchet, a., and Yu, J. (2014). Atlantic-Pacific seesaw and its role in outgassing CO<sub>2</sub> during Heinrich events. *Paleoceanography*, 29(1):58–70.
- Milankovitch, M. (1941). Kanon der erdbestrahlung und sei eiszeitenproblem. *Acad. R. Serbe (Belegade)*, ed. *Spec. 133 Sect. Sci. Math. Naturales*, 633. (translated by the Israel Program for Scientific Translations. Jerusalem, 1970).
- Mix, A., Bard, E., and Schneider, R. (2001). Environmental processes of the ice age: land, oceans, glaciers (epilog). *Quaternary Science Reviews*, 20(4):627–657.
- Monnin, E., Indermühle, A., Dällenbach, A., Flückiger, J., Stauffer, B., Stocker, T. F., Raynaud, D., and Barnola, J.-M. (2001). Atmospheric CO<sub>2</sub> concentrations over the last glacial termination. *Science (New York, N.Y.)*, 291(5501):112–4.
- Naidu, P. D. and Govil, P. (2010). New evidence on the sequence of deglacial warming in the tropical Indian Ocean. *Journal of Quaternary Science*, 25(7):1138–1143.
- Negre, C., Zahn, R., Thomas, A. L., Masqué, P., Henderson, G. M., Martínez-Méndez, G., Hall, I. R., and Mas, J. L. (2010). Reversed flow of Atlantic deep water during the Last Glacial Maximum. *Nature*, 468(7320):84–8.
- Oppo, D. W. and Fairbanks, R. G. (1987). Variability in the deep and intermediate water circulation of the Atlantic Ocean during the past 25,000 years: Northern Hemisphere modulation of the Southern Ocean. *Earth and Planetary Science Letters*, 86(1):1–15.
- Oppo, D. W. and Lehman, S. J. (1993). Mid-depth circulation of the subpolar north Atlantic during the last glacial maximum. *Science (New York, N.Y.)*, 259(5098):1148–52.

- Orsi, A. H., Smethie, W. M., and Bullister, J. L. (2002). On the total input of Antarctic waters to the deep ocean: A preliminary estimate from chlorofluorocarbon measurements. *Journal of Geophysical Research*, 107(C8):3122.
- Otto-Bliesner, B. L., Brady, E. C., Clauzet, G., Tomas, R., Levis, S., and Kothavala, Z. (2006). Last Glacial Maximum and Holocene Climate in CCSM3. *Journal of Climate*, 19(11):2526–2544.
- Otto-Bliesner, B. L., Hewitt, C. D., Marchitto, T. M., Brady, E. C., Abe-Ouchi, A., Crucifix, M., Murakami, S., and Weber, S. L. (2007). Last Glacial Maximum ocean thermohaline circulation: PMIP2 model intercomparisons and data constraints. *Geophysical Research Letters*, 34(12):L12706.
- Pahnke, K., Goldstein, S. L., and Hemming, S. R. (2008). Abrupt changes in Antarctic Intermediate Water circulation over the past 25,000 years. *Nature Geoscience*, 1(12):870–874.
- Paul, A. and Schafer-Neth, C. (2003). Modeling the water masses of the Atlantic Ocean at the Last Glacial Maximum. *Paleoceanography*, 18(3):1058.
- Peltier, W. (2004). Global glacial isostasy and the surface of the ice-age Earth: The ICE-5G (VM2) Model and GRACE. *Annual Review of Earth and Planetary Sciences*, 32(1):111–149.
- Peltier, W. R. (1994). Ice age paleotopography. *Science (New York, N.Y.)*, 265(5169):195–201.
- Piola, A. R. and Gordon, A. L. (1989). Intermediate waters in the southwest South Atlantic. *Deep Sea Research Part A. Oceanographic Research Papers*, 36(1):1–16.
- Praetorius, S. K., McManus, J. F., Oppo, D. W., and Curry, W. B. (2008). Episodic reductions in bottom-water currents since the last ice age. *Nature Geoscience*, 1(7):449–452.

- Prentice, I. C. and Jolly, D. (2000). Mid-holocene and glacial-maximum vegetation geography of the northern continents and Africa. *Journal of Biogeography*, 27(3):507–519.
- Purkey, S. G. and Johnson, G. C. (2010). Warming of Global Abyssal and Deep Southern Ocean Waters between the 1990s and 2000s: Contributions to Global Heat and Sea Level Rise Budgets\*. *Journal of Climate*, 23(23):6336–6351.
- Richardson, G., Wadley, M. R., Heywood, K. J., Stevens, D. P., and Banks, H. T. (2005). Short-term climate response to a freshwater pulse in the Southern Ocean. *Geophysical Research Letters*, 32(3):L03702.
- Rickaby, R. E. M. and Elderfield, H. (2005). Evidence from the high-latitude north atlantic for variations in antarctic intermediate water flow during the last deglaciation. *Geochem. Geophys. Geosyst.*, 6(5):Q05001.
- Ritz, S. P., Stocker, T. F., Grimalt, J. O., Menviel, L., and Timmermann, A. (2013). Estimated strength of the Atlantic overturning circulation during the last deglaciation. *Nature Geoscience*, 6(3):208–212.
- Roberts, N. L., Piotrowski, A. M., McManus, J. F., and Keigwin, L. D. (2010). Synchronous deglacial overturning and water mass source changes. *Science (New York, N.Y.)*, 327(5961):75–8.
- Romahn, S., Mackensen, A., Groeneveld, J., and Pätzold, J. (2013). Deglacial intermediate water reorganization: new evidence from the Indian Ocean. *Climate of the Past*, 9(4):293–303.
- Ruddiman, W. F. (2008). *Earth's Climate: Past and Future*. W. H. Freeman and Company, second edition edition.
- Sabine, C. L., Feely, R. A., Gruber, N., Key, R. M., Lee, K., Bullister, J. L., Wanninkhof, R., Wong, C. S., Wallace, D. W. R., Tilbrook, B., Millero, F. J., Peng, T.-H., Kozyr, A., Ono, T., and Rios, A. F. (2004). The oceanic sink for anthropogenic CO<sub>2</sub>. *Science*, 305(5682):367–371.

- Sarnthein, M., Stategger, K., Dreger, D., Erlenkeuser, H., Grootes, P., Haupt, B. J., Jung, S., Kiefer, T., Kuhnt, W., Pflaumann, U., Schafer-Neth, C., Schulz, H., Schulz, M., Seidov, D., Simstich, J., van Kreveld, S., Vogelsang, E., Volkerl, A., and Weinelt, M. (2001). Fundamental modes and abrupt changes in North Atlantic circulation and climate over the last 60 ky—Concepts, reconstruction and numerical modeling. In Shafer, P., Ritzrau, W., Schluter, M., and Thiede, J., editors, *The Northern North Atlantic: A Changing Environment*, pages 365–410. Springer, Berlin.
- Seidov, D. and Maslin, M. (2001). Atlantic ocean heat piracy and the bipolar climate see-saw during Heinrich and Dansgaard-Oeschger events. *Journal of Quaternary Science*, 16(4):321–328.
- Shepherd, A., Ivins, E. R., A, G., Barletta, V. R., Bentley, M. J. M. J., Bettadpur, S., Briggs, K. H., Bromwich, D. H., Forsberg, R., Galin, N., Horwath, M., Jacobs, S. S., Joughin, I., King, M. a., Lenaerts, J. T. M., Li, J., Ligtenberg, S. R. M., Luckman, A., Luthcke, S. B., McMillan, M., Meister, R., Milne, G. G., Mouginot, J., Muir, A., Nicolas, J. P., Paden, J., Payne, A. J., Pritchard, H. D., Rignot, E., Rott, H., Sorensen, L. S., Scambos, T. a. T. a., Scheuchl, B., Schrama, E. J. O., Smith, B. E., Sundal, A. V., van Angelen, J. H., van de Berg, W. J., van den Broeke, M. R., Vaughan, D. G., Velicogna, I., Wahr, J., Whitehouse, P. L., Wingham, D. J., Yi, D., Young, D., Zwally, H. J., and Sørensen, L. S. (2012). A reconciled estimate of ice-sheet mass balance. *Science*, 338(6111):1183–1189.
- Shin, S.-I. (2003). Southern Ocean sea-ice control of the glacial North Atlantic thermohaline circulation. *Geophysical Research Letters*, 30(2):1096.
- Shin, S.-I., Liu, Z., Otto-Bliesner, B. L., and Brady, E. C. (2003). A simulation of the Last Glacial Maximum climate using the NCAR-CCSM. *Climate Dynamics*, 20:127–151.
- Sloyan, B. M. and Rintoul, S. R. (2001). Circulation, Renewal, and Modification of Antarctic Mode and Intermediate Water. *Journal of Physical Oceanography*, 31(4):1005–1030.

- Stanford, J. D., Rohling, E. J., Bacon, S., Roberts, A. P., Grousset, F., and Bolshaw, M. (2011). A new concept for the paleoceanographic evolution of Heinrich event 1 in the North Atlantic. *Quaternary Science Reviews*, 30(9-10):1047–1066.
- Stanford, J. D., Rohling, E. J., Hunter, S. E., Roberts, A. P., Rasmussen, S. O., Bard, E., McManus, J., and Fairbanks, R. G. (2006). Timing of meltwater pulse 1a and climate responses to meltwater injections. *Paleoceanography*, 21(4):PA4103.
- Stommel, H. (1958). The abyssal circulation. *Deep Sea Research*, 5(1):80–82.
- Stouffer, R. J., Yin, J., Gregory, J. M., Dixon, K. W., Spelman, M. J., Hurlin, W., Weaver, A. J., Eby, M., Flato, G. M., Hasumi, H., Hu, A., Jungclaus, J. H., Kamenkovich, I. V., Levermann, A., Montoya, M., Murakami, S., Nawrath, S., Oka, A., Peltier, W. R., Robitaille, D. Y., Sokolov, A., Vettoretti, G., and Weber, S. L. (2006). Investigating the Causes of the Response of the Thermohaline Circulation to Past and Future Climate Changes. *Journal of Climate*, 19(8):1365–1387.
- Swingedouw, D., Braconnot, P., and Marti, O. (2006). Sensitivity of the atlantic meridional overturning circulation to the melting from northern glaciers in climate change experiments. *Geophys. Res. Lett.*, 33(7):L07711.
- Talley, L. D., Pickard, G., Emery, W. J., and Swift, J. H. (2011). *Descriptive physical oceanography: an introduction*. Elsevier, Oxford, UK, 6th edition.
- Tessin, A. C. and Lund, D. C. (2013). Isotopically depleted carbon in the mid-depth South Atlantic during the last deglaciation. *Paleoceanography*, 28(2):296–306.
- Thornalley, D. J. R., Barker, S., Broecker, W. S., Elderfield, H., and McCave, I. N. (2011). The deglacial evolution of North Atlantic deep convection. *Science (New York, N.Y.)*, 331(6014):202–5.
- Tomczak, M. and Large, D. G. B. (1989). Optimum multiparameter analysis of mixing in the thermocline of the eastern Indian Ocean. *Journal of Geophysical Research*, 94(C11):16141–16149.

- Wainer, I., Clauzet, G., Ledru, M.-P., Brady, E., and Otto-Bliesner, B. (2005). Last glacial maximum in South America: Paleoclimate proxies and model results. *Geophys. Res. Lett.*, 32(8):L08702.
- Wainer, I., Goes, M., Murphy, L. N., and Brady, E. C. (2012). Changes in the intermediate water mass formation rates in the global ocean for the Last Glacial Maximum, mid-Holocene and pre-industrial climates. *Paleoceanography*, 27(3):PA3101.
- Wang, Y. V., Leduc, G., Regenberg, M., Andersen, N., Larsen, T., Blanz, T., and Schneider, R. R. (2013). Northern and southern hemisphere controls on seasonal sea surface temperatures in the Indian Ocean during the last deglaciation. *Paleoceanography*, 28(4):619–632.
- Weaver, A. J., Saenko, O. A., Clark, P. U., and Mitrovica, J. X. (2003). Meltwater pulse 1A from Antarctica as a trigger of the Bølling-Allerød warm interval. *Science (New York, N.Y.)*, 299(5613):1709–13.
- Xie, R. C., Marcantonio, F., and Schmidt, M. W. (2012). Deglacial variability of Antarctic Intermediate Water penetration into the North Atlantic from authigenic neodymium isotope ratios. *Paleoceanography*, 27(3):PA3221.
- Yokoyama, Y., Lambeck, K., De Deckker P, Johnston, P., and Fifield, L. K. (2000). Timing of the Last Glacial Maximum from observed sea-level minima. *Nature*, 406(6797):713–6.
- You, Y. (1998). Intermediate water circulation and ventilation of the Indian Ocean derived from water-mass contributions. *Journal of Marine Research*, 56(5):1029–1067.
- Yu, E.-F., Francois, R., and Bacon, M. P. (1996). Similar rates of modern and last-glacial ocean thermohaline circulation inferred from radiochemical data. *Nature*, 379(6567):689–694.
- Zhang, X., Lohmann, G., Knorr, G., and Purcell, C. (2014). Abrupt glacial climate shifts controlled by ice sheet changes. *Nature*, 512(7514):290–294.

- Zonneveld, K. A., Ganssen, G., Troelstra, S., Versteegh, G. J., and Visscher, H. (1997). Mechanisms forcing abrupt fluctuations of the indian ocean summer monsoon during the last deglaciation. *Quaternary Science Reviews*, 16(2):187–201.